

POLITECNICO DI TORINO

Faculty of Aerospace Engineering

Master Thesis

**Conceptual design and
prototyping of a fast-acting valve
for blowdown wind tunnels.**



**Politecnico
di Torino**

Supervisor:

Prof. Andrea Ferrero

Co-supervisor:

Prof. Daniele Botto

Candidate:

Davide De Martino

Von Karman Institute Tutors:

Prof. Sergio Lavagnoli, Eng. Fernando Linares Dorado

March-April 2025

Acknowledgements

I would like to say thank you to Eng. Fernando Linares Dorado and Prof. Sergio Lavagnoli for giving me a very relevant first touch with a professional, friendly and inspiring workplace, and for the guidance they provided along the development of my thesis. I would also like to express my gratitude to my supervisors Prof. Daniele Botto and Prof. Andrea Ferrero, for the skillful insights they provided during the project.

I would like to thank my parents for allowing me to pursue my passions and for supporting me in difficult moments. And thank you to my siblings, for the happy memories and valuable lessons I learned growing up together.

To all my friends from high school, it has almost been 10 years, and I look forward to the next 10. I thank you for helping me grow up the way I did, I am proud of it, and I hope it has been as good for you knowing me as it has been for me knowing you.

To all my friends from Polito, the support we have given one another is one of the main reasons I have been able to retain my hairline through the hard 5 years that are now behind us. I sincerely hope we will keep in touch and that our beautiful friendships survive through the physical distance that is probably going to separate us.

Abstract

This project aims at developing and prototyping an upgraded version of an existing shutter valve for two different compression tube turbomachinery wind tunnels in use at the Von Karman Institute. The current solution has been analyzed in detail, a list of requirements has been produced for the new solution and a literature review has been conducted to define a state of the art for fast-acting valve solutions in multidisciplinary applications. Concepts for the solution have been analyzed and the performance of the most promising one has been modeled through a MATLAB script. The model takes into account thermodynamic effects of the pneumatic actuator powering the system, inertia, kinematics and dynamics of components. As a result, contact forces and reaction forces for different components have been evaluated and used to size some parts of the system and of a scaled down prototype version.

Contents

List of Figures	VII
List of Tables	XI
1 Introduction	1
1.1 CT3 and CT2 wind tunnels	2
1.1.1 Basic working principles	2
1.1.2 CT3 wind tunnel	3
1.2 Current architecture of the valve	5
1.2.1 Basic working principles	5
1.2.2 Detailed description of components and construction	6
1.2.3 Performance and effect on wind tunnel	9
2 Requirements and constraints for the new solution	13
3 Possible solutions	16
3.1 Literature review of fast-acting valves	16
3.1.1 Case studies	19
3.2 Chosen solution for CT2 and CT3	22
4 Updated requirements and constraints	23
5 Pneumatics Modeling	25
5.1 Hypothesis and equations	25
5.2 Implementation and parameter calibration of the model	27
6 Investigated solutions	32
6.1 Angled locking pin	32
6.1.1 General description	32
6.1.2 Simplified modeling	33

6.1.3	Negative outcome	36
6.2	Brake	36
6.2.1	General description	36
6.2.2	Simplified modeling	36
6.2.3	Detailed modeling	38
6.2.4	Negative outcome	48
6.3	Rocker Block	48
6.3.1	General description	48
6.3.2	Simplified modeling	49
6.3.3	Detailed modeling	52
6.3.4	Implementation	55
6.3.5	Dimensions of the valve's rod end	57
6.3.6	Results for CT3 scale model	59
6.3.7	Scaling for Prototype	69
7	Conclusions and future work	79
	References	81

List of Figures

1.1	Simplified diagram of the Isentropic Light Piston tube facilities [1].	2
1.2	Section drawing of CT3 [2]	3
1.3	Temporal evolution of the pressure, temperature and rotational speed during a typical test [1].	4
1.4	Simplified drawing of the shutter valve in use on CT3.	5
1.5	Section of the shutter assembly [3].	7
1.6	Top view of the shutter assembly, upper plate removed [3].	7
1.7	Section of the piston and lock assembly [3].	8
1.8	Section of the lock assembly [3].	10
1.9	Shutter valve opening, characteristic [4].	11
1.10	Effect of opening time on pressures [1].	11
3.1	Simplified diagram of type I valves [5].	18
3.2	Simplified diagram of type II valves [5].	19
3.3	Simplified diagram of type III valves [5].	19
3.4	Simplified diagram of type IV valves [5].	20
3.5	Simplified diagram of type V valves [5].	20
3.6	Section view of the fast-acting plug valve of the Oxford HDT in the closed state [6].	21
5.1	Volumes of the chambers.	29
5.2	Pressures in the chambers.	29
5.3	Temperatures in the chambers.	30
5.4	Mass of air in the chambers.	30
5.5	Comparison between experimental data (from figure 1.9) and simulation	31
5.6	Comparison between experimental data (from figure 1.9) and simulation, $\beta = 0$	31

6.1	Simplified diagram of the angled locking pin (valve is closed). The sketch is not representative of proportions or any other quantitative factor, it should only be used for the general understanding of the concept.	33
6.2	Force diagram for the static equilibrium of the valve's rod end at incipient movement (where friction forces are at their maximum values). In red the forces exerted by the pin, in green the ones exerted by the guide, and in black the one exerted by the valve's actuator. . .	34
6.3	Force diagram for the static equilibrium of the pin at incipient movement (where friction forces are at their maximum values). In red the forces exerted by the pin's actuator, in green the ones exerted by the pin's guide, and in red the one exerted by the pin's actuator.	34
6.4	Piston diameters for starting the pin's motion (d_{min}) and to accelerate it to avoid slip (d_{ns}).	35
6.5	Simplified diagram of the brake (valve is closed). The sketch is not representative of proportions or any other quantitative factor, it should only be used for the general understanding of the concept.	37
6.6	Free body diagram of the valve's rod end and of the brake at incipient movement, when the drag forces are at their maximum.	38
6.7	Required actuator diameter.	39
6.8	Free body diagram of the valve's rod end and of the brake during movement.	40
6.9	Actuator's chamber volumes in time.	41
6.10	Mass of air in the actuator's chambers in time.	42
6.11	Temperature of air in the actuator's chambers in time.	42
6.12	Pressure of air in the actuator's chambers in time.	43
6.13	Brake's actuator displacement in time.	43
6.14	Coefficient of friction in time. It grows as the pushing force decreases, and once it reaches the maximum static level it lowers and settles at μ_{din}	44
6.15	C_{\perp} in time.	45
6.16	Valve's downward acceleration a_v	45
6.17	Comparison of the performance of the system in terms of valve's displacement, with the current setup.	46
6.18	Residuals res_i in time.	47

6.19	Simplified diagram of the rocker block, in closed configuration (on the left) and during opening (on the right). The sketch is not representative of proportions or any other quantitative factor, it should only be used for the general understanding of the concept.	49
6.20	Free body diagram of the rocker and the valve's rod end in the static condition.	50
6.21	Required actuator diameter.	51
6.22	Free body diagram of the rocker and the valve's rod end in dynamic conditions.	52
6.23	Sketch for evaluating the position of P in the reference frame of the valve's rod end.	54
6.24	Sketch for evaluating the position of P in the reference frame of the rocker.	55
6.25	Haigh diagram for 42CrMo4 steel.	58
6.26	Wöhler curve for 42CrMo4 steel.	58
6.27	Actuator's chamber volumes in time.	60
6.28	Actuator's chamber pressures in time.	61
6.29	Actuator's chamber temperatures in time.	62
6.30	Mass of air in the actuator's chambers.	62
6.31	Acceleration, velocity and position of the rocker's actuator.	63
6.32	Angles' evolution in time.	64
6.33	Angular velocities.	64
6.34	Angular accelerations.	65
6.35	Contact forces.	65
6.36	Residuals for γ , the position of P and for the vertical equilibrium of the valve.	66
6.37	Valve acceleration.	67
6.38	Valve displacement comparison.	67
6.39	Lateral and frontal views of the rocker and rod end assembled in the closed configuration.	68
6.40	Actuator's chamber volumes in time.	70
6.41	Actuator's chamber pressures in time.	71
6.42	Actuator's chamber temperatures in time.	71
6.43	Mass of air in actuator's chambers.	72
6.44	Acceleration, velocity and displacement of the rocker's actuator.	73
6.45	Angles' evolution in time.	74
6.46	Angular velocities.	74

6.47	Angular accelerations.	75
6.48	C_{\perp} and R_x	75
6.49	Residuals for γ , the position of P and for the vertical equilibrium of the valve's placeholder.	76
6.50	Valve acceleration.	77
6.51	Valve displacement.	77
6.52	$\frac{C_{\perp}}{F}$ evolution as the rocker rotates by $\tilde{\varphi}$	78

List of Tables

3.1	Comparison of different systems used for valve actuation [5].	17
6.1	Table with unaddressed parameters for the CT3 scale rocker.	59
6.2	Table with parameters for the scaled prototype rocker.	70

Chapter 1

Introduction

With the purpose of measuring the performance and heat transfer of turbomachinery components, at the von Karman Institute there are two different facilities, CT2 for linear cascades and CT3 for full annular stage testing. These wind tunnels operate using the Isentropic Light Piston Compression Tube principle, where the test gas is initially compressed by a piston, and therefore heated up, and subsequently released by a valve or diaphragm into the test section. The tests start at the valve opening and end once all the test gas is exhausted or when the dump tank reaches a high enough pressure. This translates in short test times (usually lower than 1 s), but long enough to provide meaningful measurements.

The components are tested on and off-design, by matching the adimensional parameters of the flow to accurately reproduce the relevant phenomena that the test aims at capturing. In the case of turbines, the wind tunnels achieve this by allowing interdependent variation of Mach number and Reynolds number. In this way, flow compressibility, viscous and inertial forces can be accurately reproduced.

Both CT3 and CT2 were designed and constructed about 40 years ago, and feature a shutter valve, separating the compressed test gas from the test section, that uses consumables and a small explosive that need to be replaced after every test. This has a toll on the time necessary to prepare the wind tunnels for testing, and exposes the operators to dangerous materials. The objective of this project is to design and prototype a fast acting valve that may replace these outdated systems, in order to reduce preparation times and lower the chances of injury for the staff.

The thesis starts with an overview of the CT3 facility and of the shutter valve currently in use. From this, a list of requirements and constraints for the new system was derived, to maintain the current operational capabilities of the wind tunnel. There will follow an overview of solutions used in similar applications and an analysis

of those, in relation to the requirements set. Subsequently, the analysis of different applicable configurations will be investigated, and all but one of them will be discarded for different reasons, at different levels of detail of the analysis. The end result of this work is the dimensioning of some of the components for a prototype of the solution that shows to be the most promising.

1.1 CT3 and CT2 wind tunnels

1.1.1 Basic working principles

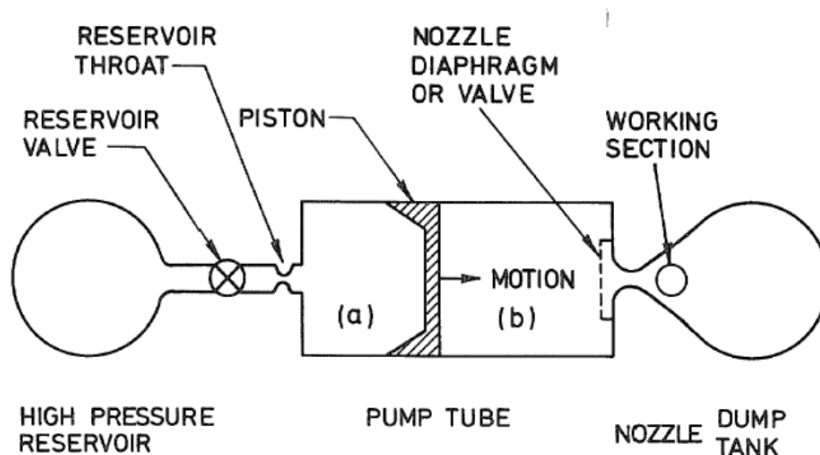


Figure 1.1: Simplified diagram of the Isentropic Light Piston tube facilities [1].

Figure 1.1 shows a simplified diagram of the wind tunnels. They can be divided in four basic components: a high pressure reservoir, the compression tube, a shutter valve and a dump tank, downstream of the test section. At the start of the test cycle sequence, the shutter valve is closed, isolating chamber (b) of the compression tube from the dump tank. The piston is placed at the left end of the tube, and the gas inside is set $P_{initial}$ value and atmospheric temperature. The test section and dump tank are instead evacuated to a maximum of 25 mbar (absolute pressure). High pressure air flows from the reservoir into chamber (a) through an adjustable choked throat area, and this pushes the piston to the right, quasi-isentropically compressing and heating the test gas in chamber (b). When the correct pressure value P_{final} is reached in chamber (b), the shutter receives the opening signal. This moment is conventionally assumed to be the start of the test. As the gas discharges into the test section, the pressure in chamber (b) is kept constant by the piston: the volumetric airflow into chamber (a) is matched to the one into the dump tank,

through a choked throat area downstream of the test section. This ensures constant total pressure and temperature at the inlet of the test section. As pressure rises in the dump tank, the pressure ratio at the throat area lowers and the throat unchokes, allowing perturbations to travel upstream of the dump tank and thus causing the end of the test. Figure 1.3 illustrates the progression of the parameters of interest during the test: the pressure in compression tube rises linearly until the valve opens. Upon opening, both the total inlet pressure and temperature in the test section quickly rise and stabilize after a brief transient period. The test concludes when the perturbations from the dump tank reach the test section.

1.1.2 CT3 wind tunnel

This chapter will discuss in higher detail CT3, as it was used as a reference case for this project.

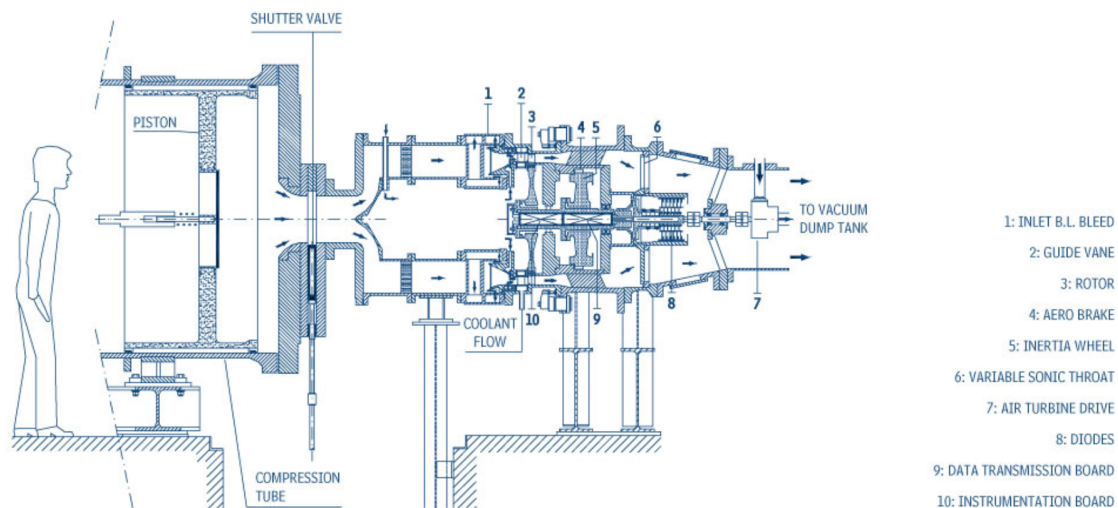


Figure 1.2: Section drawing of CT3 [2]

The facility can deliver stage mass flows between 5 and 30 kg/s, with inlet total temperature typically close to 450 K and inlet total pressure rarely above 3.5 bar. Tests usually last approximately 0.4 s (after the opening signal of the shutter valve). The correct aerodynamic conditions to take measurements are only present for the last 0.2 s of the test, as the flow conditions are changing and stabilizing before. Both time averaged and time resolved data is usually analyzed on a time window of

about 0.03 s, so that rotational speed, relative inlet flow angle relative to the rotor and pressure variation are sufficiently small to consider the tests as performed in steady state conditions. The rotor can achieve speeds up to 8,000 rpm, generating instantaneous powers of 1–2 MW, with acceleration regulated by an inertia wheel.

CT3 enables accurate measurements of convective heat transfer on turbine components, replicating realistic gas-to-wall and gas-to-coolant temperature ratios. The test section accommodates a rotating turbine stage and allows for the installation of additional downstream components, such as a second stator. An independent coolant supply system delivers air or foreign gas to critical areas, including stator and rotor airfoils, platforms, and disc cavities.

The facility advances the understanding of aerodynamics, heat transfer, and efficiency in cooled high-pressure turbines. Studies focus on rim-seal and cavity flows, leakage flows, and unsteady blade row interactions. Rainbow rotor and stator rows facilitate the simultaneous evaluation of aerothermal performance for different turbine designs. Recent upgrades support investigations of high-speed, low-pressure turbines representative of next-generation geared turbofan engines.

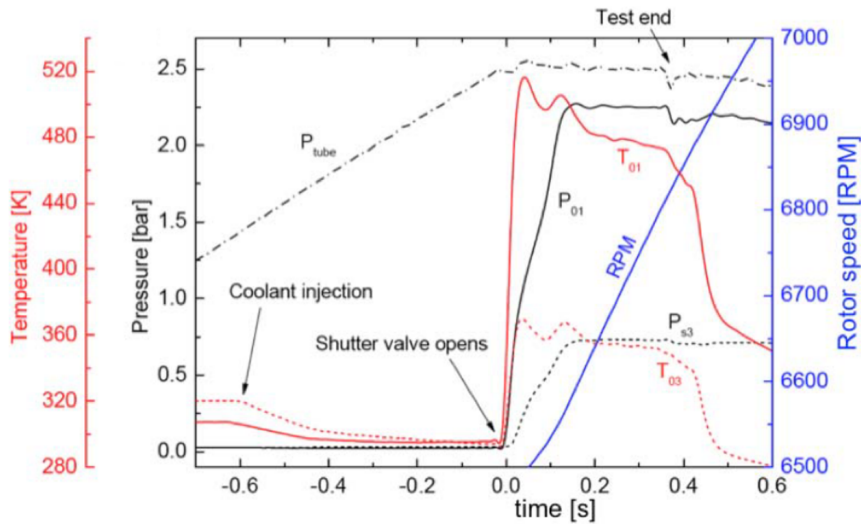


Figure 1.3: Temporal evolution of the pressure, temperature and rotational speed during a typical test [1].

1.2 Current architecture of the valve

1.2.1 Basic working principles

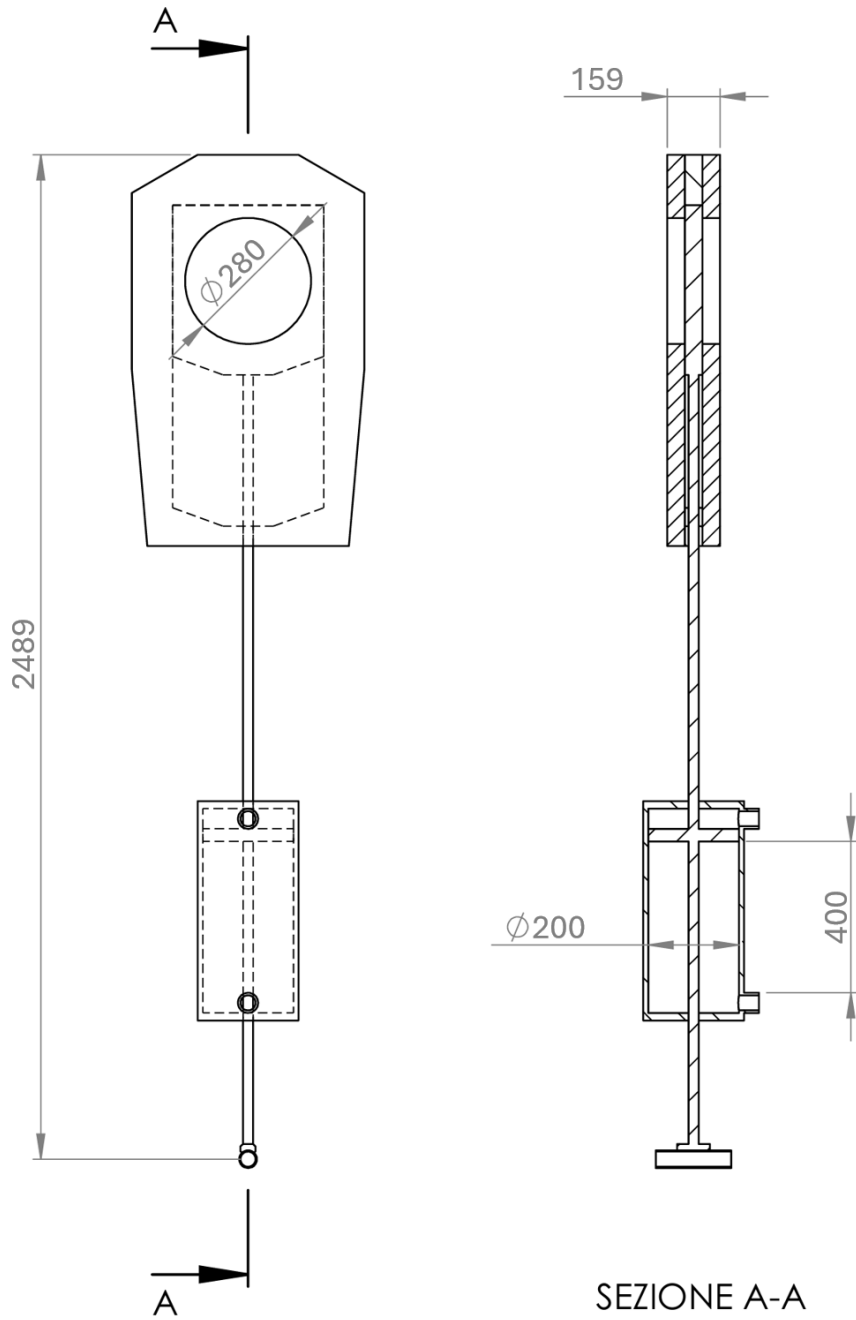


Figure 1.4: Simplified drawing of the shutter valve in use on CT3.

In figure 1.2 it is possible to see that the valve is positioned between the compression tube (on the left) and the test section assembly (on the right). Now, with reference to figure 1.4 we will discuss its basic working principles.

The main components of the valve are the shutter, the lock, and the pneumatic actuator. As seen from SECTION A-A in figure 1.4 the shutter is sandwiched by two plates that bolt to the end of the compression tube on the left and to the start of the test section assembly to the right. Both plates have an opening to allow the airflow to reach the test section from the compression tube. The shutter slides up and down, respectively blocking or uncovering the area of the passages in the sandwiching plates to either isolate or connect the test section to the compression tube.

The pneumatic actuator is responsible for opening and closing the valve, with the case of the actuator being secured to the main structure through mounting hardware bolted to the plate on the test section side. The piston is connected at one end to the shutter and at the other end to the lock through rods. The top chamber of the piston is pre-pressurized before every test, enabling fast opening time and low delay with respect to the opening signal.

The lock is a consumable PMMA cylinder whose purpose is to withstand the force that the actuator exerts on it before each test, when the top chamber of the cylinder is pressurized but the valve needs to remain closed. It is destroyed at every test run by a small detonator placed inside it, which is triggered at opening time.

To summarize, the procedure to prepare the valve for each test is to close the valve, insert the lock in its seating, along with the detonator inside it, and then pressurize the top chamber of the actuator, thus loading the lock with the piston force. At opening time, the opening signal triggers the detonator through electrical current, which destroys the lock, allowing the pressurized air in the top chamber of the actuator to push the shutter down, and thus uncovering the passage for the air to flow into the test section.

1.2.2 Detailed description of components and construction

Figure 1.5 shows the shutter assembly in the closed configuration. With reference to this picture, we will analyze the components that make up the shutter and how it is connected to the other parts.

Part 10 in the assembly is the main piece, and connects all the other parts to the piston, through the end of a threaded rod and its nut. It has a circular opening to allow the installation of part 9, which is the part that seals against the plate on the compression tube side (the bottom one in figure 1.5). The sealing surface between

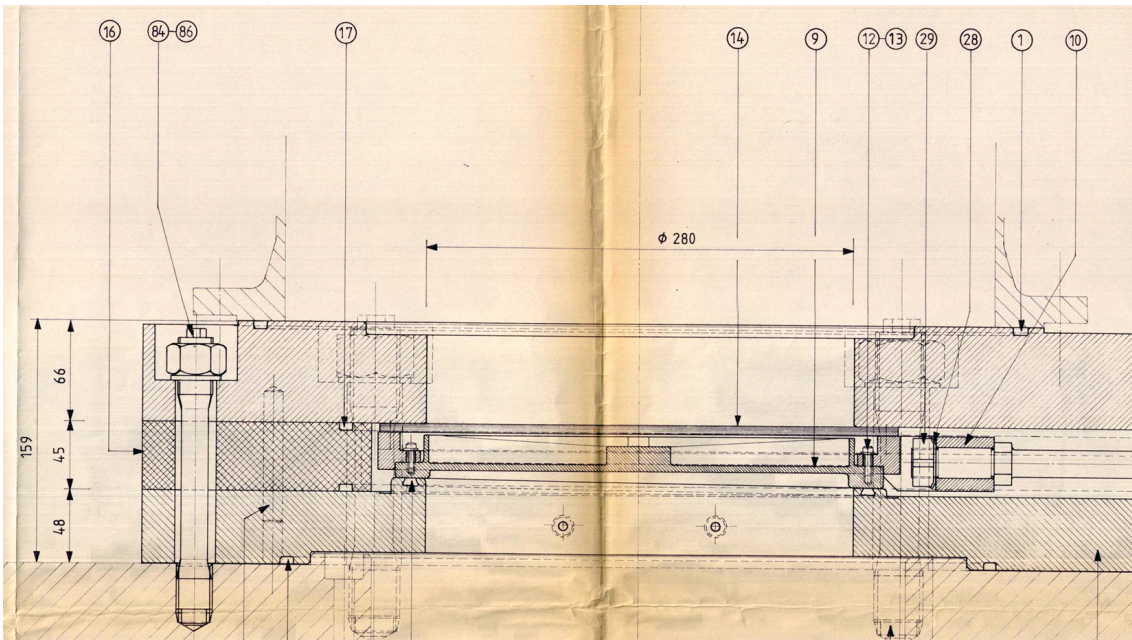


Figure 1.5: Section of the shutter assembly [3].

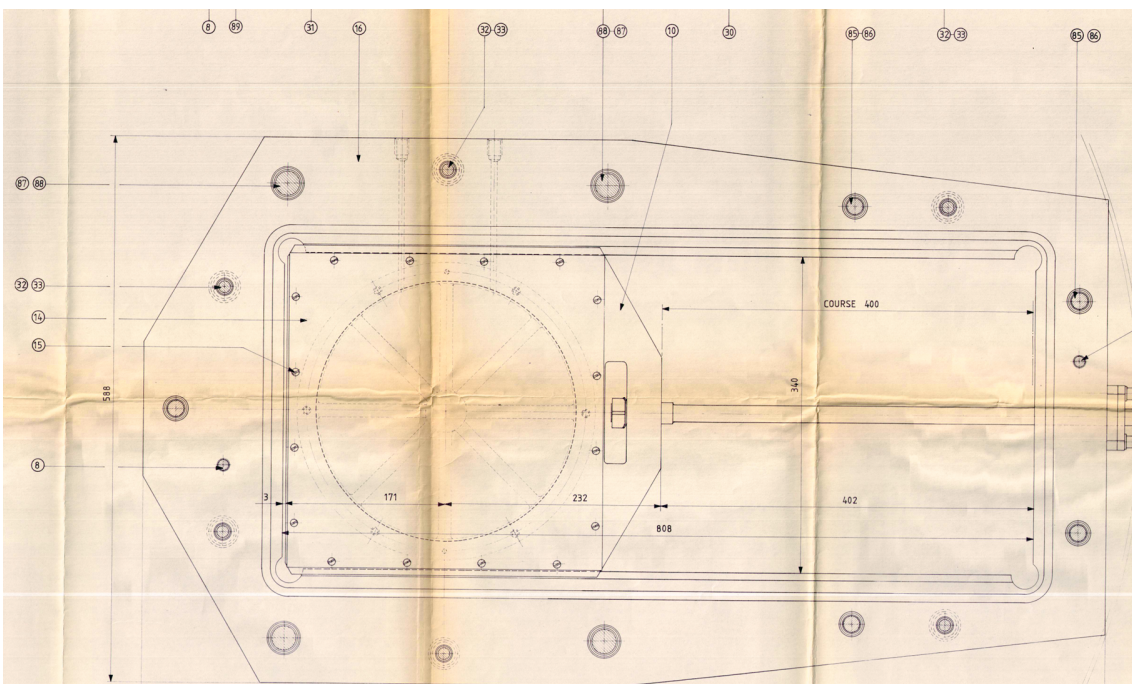


Figure 1.6: Top view of the shutter assembly, upper plate removed [3].

this part and the bottom plate is slanted by 1° , and this wedge-like shape causes seal compression as the shutter travels upward (to the left with reference to figure 1.5). Part 14 is a PTFE frame that surrounds the circular opening in part 9, and its role is to reduce the friction that stems from the compression of the parts due to

the wedge-like shape of the sealing surface. Figure 1.6 shows the shape of part 10 and how it is guided in its motion by part 16, which acts as a rail, ensuring precise movement of the shutter. Part 16 has an opening at the bottom through which the rod slides to move the shutter. Just right of the opening (not shown in the images), there is an adjustment mechanism, where two rod ends with opposite threading are joined by the same long nut. When the nut is rotated in one direction, the ends of the rods are drawn closer together, while rotating it in the opposite direction causes the ends to move farther apart. This allows precise adjustment for the position of the piston and other moving components relative to the shutter.

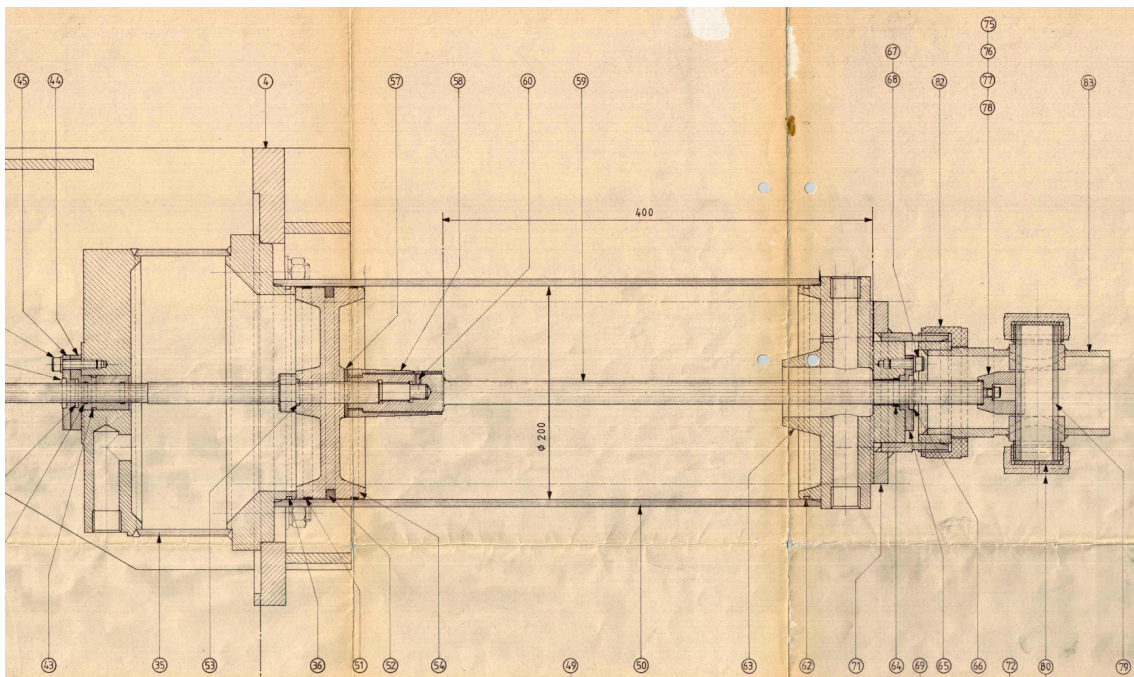


Figure 1.7: Section of the piston and lock assembly [3].

We will now reference figure 1.7. The rod is eventually connected to the piston and the lock assembly. The actuator is made with a tie-rod construction, where four rods (not visible in figure 1.7) compress the main cylinder sleeve between the head and bottom of the actuator.

The head of the actuator (part 35) is made of three components. Starting from the left, there is the top component, connected to the 7 bar feed line by a 3/4 in threaded inlet and welded to a sleeve of larger bore compared to the piston bore. The other end of the sleeve is welded to the last component that makes up the head assembly. The tie-rods connect to it and it is bolted to the support structure (part 4). The other end of this component is inserted in the main actuator sleeve, inside of which the piston sits. The bore of 200 mm enables a force of about 19 kN to pull

the valve open. The rod extends through the center of the piston, and another rod is screwed to its end, squeezing the piston between the shoulder of the first rod and the left end of the second rod. In this position is also located a dampener, which is a body of varying diameter which inserts inside the main exhaust port of the bottom of the actuator as the piston reaches the end of its travel. In this way, the exhaust port is partially blocked for the final phase of the opening, building pressure in the bottom chamber and slowing down the moving assembly.

We will now reference figure 1.8. The bottom of the actuator has a main exhaust port, traversed by the rod, which then splits in two $3/4$ in threaded exhaust ports. The rod continues through the entire bottom piece of the actuator and part 75 is bolted to its end. Part 71 is bolted to the bottom of the actuator and is made of a flange that is welded to an adapter that has a threaded end. A large nut (part 82) is screwed at the end of the adapter, and supports part 83. Transversely to the axis of the rod, we see the PMMA lock (part 79) enclosed in its seat by caps on each side. The lock is loaded by part 75 with the force exerted by the pre-pressurized actuator. As you may notice, the cap on the bottom side of the lock has a small hole, used to run the wires that trigger the detonator.

Most of the parts that make up the valve are made of steel. However there are some exceptions: part 10 and 71, which are aluminum alloy, part 14 which is made of PTFE, part 79, made of PMMA as previously mentioned, and part 9, made of titanium. A gross estimation of the mass of the moving parts, based on density of the materials and approximated volumes of each part, yields a mass of the moving components of the shutter of 13.5 kg. As visible in figure 1.7, the piston travel is 400 mm and the piston bore is 200 mm.

The whole valve assembly sits vertically, as seen from figure 1.2 and is partially placed under the floor level, in a space underground accessible through a hatch to change the consumables.

1.2.3 Performance and effect on wind tunnel

Figure 1.9 shows the normalized displacement over time of the valve. The movement starts just before the 100 ms mark, and the valve rapidly accelerates to ~ 10 m/s. The speed is maintained until about 120 ms, when the combined effect of the cushion of air in the bottom chamber and the insufficient inflow into the top chamber brings the shutter to a stop. Motion restarts once the pressures rise in the top and drop further in the bottom chamber, bringing the assembly to a final stop at the very end of the travel about 180 ms after the motion started.

The most important parameters for the valve are the delay, which occurs between

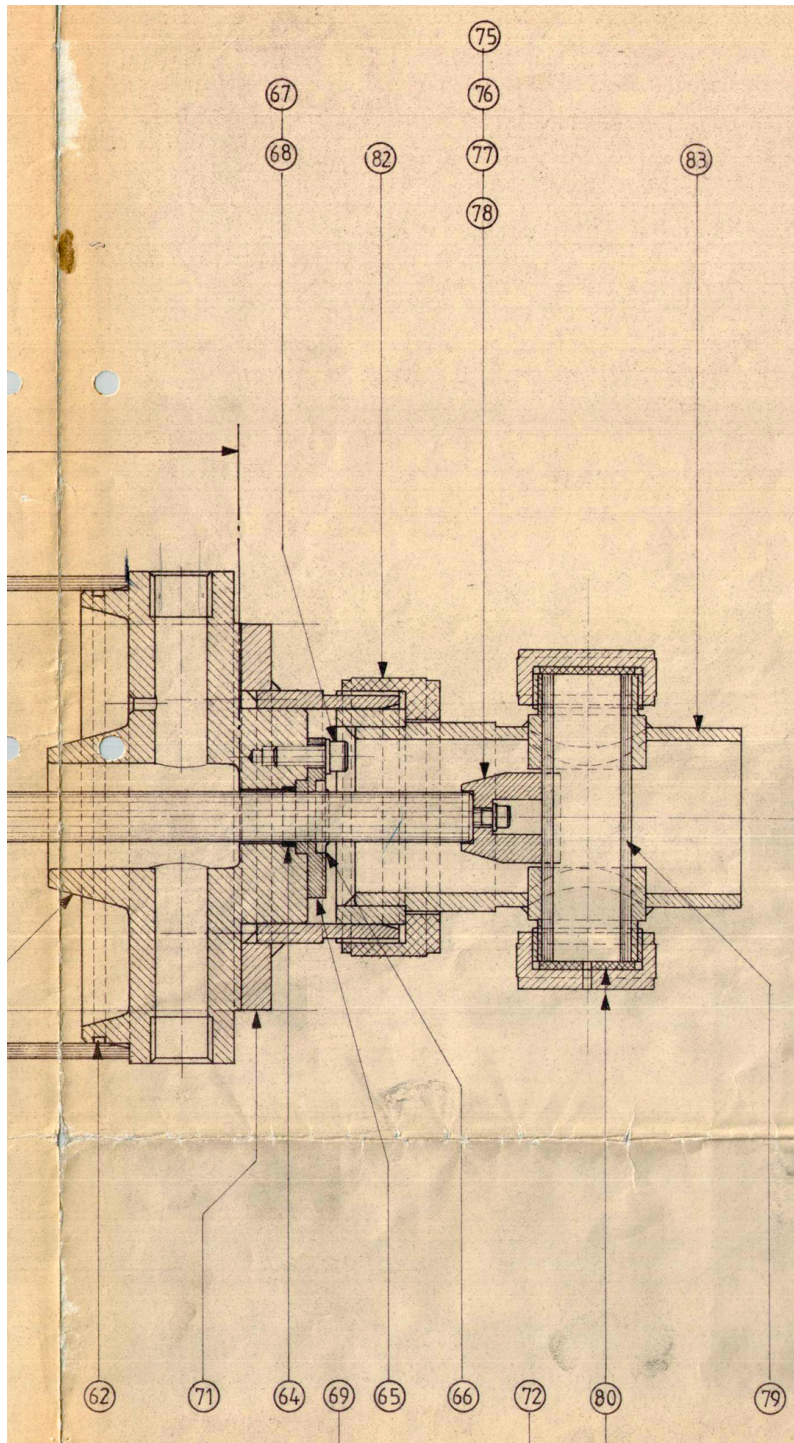


Figure 1.8: Section of the lock assembly [3].

the opening signal and actual downward movement of the valve, and the opening time. It has been shown by previous work that the opening time of the valve has a strong impact on inlet temperatures and pressures.

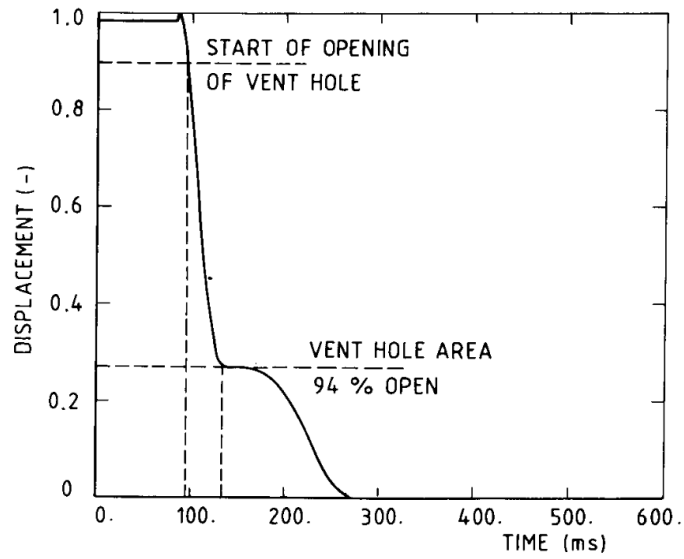


Figure 1.9: Shutter valve opening, characteristic [4].

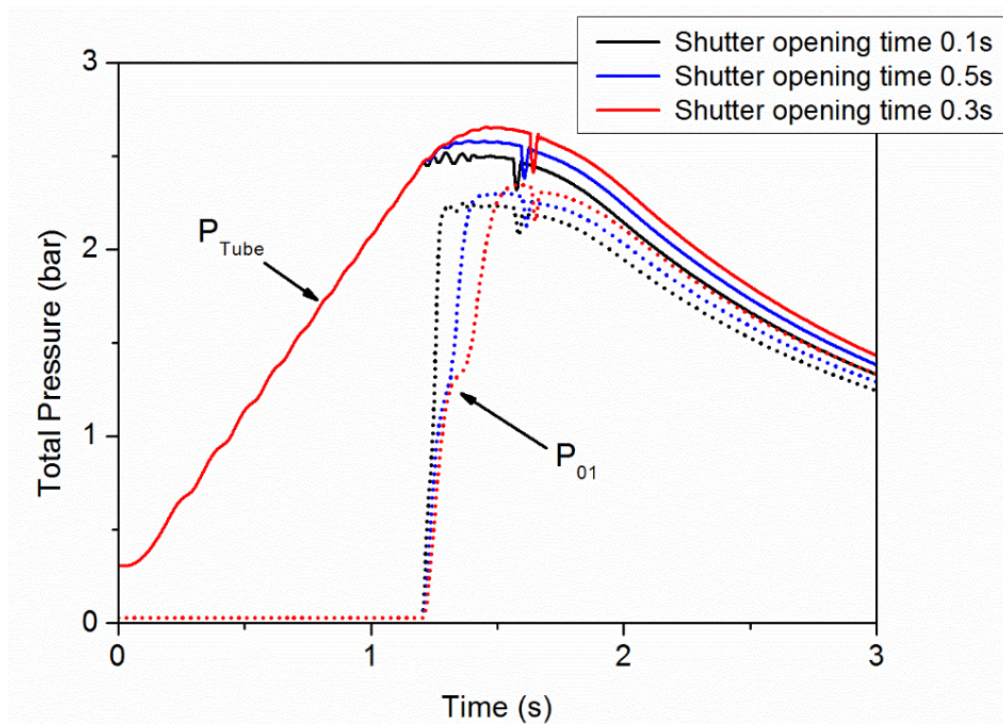


Figure 1.10: Effect of opening time on pressures [1].

In figure 1.10 we can see that higher opening times cause higher total pressure during the test phase, a higher delay in the rise of the total pressure at the turbine inlet, thus decreasing test times. The higher pressure values also means that the total temperature at turbine inlet is higher when the valve opens slower. Delays

in the opening also imply a rise in turbine inlet total pressure, due to the higher pressure value reached in the compression tube between the opening signal and the delayed opening. This means that low opening times and low delays are paramount for the design of the new solution. Consistency is also extremely important, as test to test variance in opening time and delay can reduce the repeatability of tests done in the wind tunnel overall.

Chapter 2

Requirements and constraints for the new solution

From the previous section, we are now capable to conceptualize a list of requirements and constraints that are needed for the new valve system in order not to hinder the performance of the wind tunnel and to enhance its operation procedures. They are listed below, starting from the most important ones.

1. **The new solution should not on rely explosives, consumables or hazardous materials.** This requirement is key to the objective of this project, as the current valve architecture requires that the operators of the wind tunnel handle explosive and replace consumables, which is both dangerous and a waste of time and resources.
2. **The valve should be safe during all anomalous circumstances** such as power outages.
3. **The valve should never need inspecting while the systems are pressurized or ready to go off for tests.** This means that the valve should be made so that the risks of it being stuck closed are minimized.
4. **The valve should be easy to operate**, enabling low training time and lowering chances of injury and malfunction. This means that ideally the valve should be **automatized** and remotely operated.

5. **The valve should reliably open with low run to run variance.** This is crucial to have the facilities working at their best and producing repeatable and accurate results. A high variance in opening times or delay would significantly impact key parameters, such as total inlet temperature and pressure.
6. **The valve should open in 0.1 s**, as is the case with the current valve architecture, and **with low delays between signal and actual execution.** If delays are unavoidable but consistent with every test, it may be an option to account for them and have the opening signal at a pressure value inside the compression tube lower than $P_{initial}$, so that during the delay the pressure level rises to $P_{initial}$.
7. **The valve should generate low pressure losses** (~10% total pressure loss at the test section). The wake and turbulence should be dissipated in the settling chamber and at the test section should be comparable with or better than the current setup.
8. **Operating conditions:** the valve should be capable of sealing across high pressure (~6 bar as a safety value) and vacuum (0.25 mbar) volumes and to operate at medium temperature (450 °K).
9. **Contaminants:** the valve should not interfere with the test section by emitting particles, gases or fluids in the test airflow.
10. **Down-time:** the valve should work reliably for 10 years, without major servicing. During the 10 years period, conservatively overestimating 10 tests/day every day, 36500 total runs can be expected. The routine servicing should not exceed about 6-12 h/year, in line with the current setup. To achieve this, the parts that need routine servicing should be easily accessible.
11. **Power source:** the adopted solution should be powered by sources already available at the facility. The building is equipped with 230 V AC and 400 V AC three-phase, and different pneumatic lines at 7, 16, 40 and 300 bar. The 7 bar line would be the easiest to access, as the current valve solution is powered by it.
12. **The system should fit where the current system sits**, allowing minimal changes to the facility.
13. **Budget:** although a specific amount is not specified, the budget required for the development and installation of the new solution should be proportional with the benefits that it would bring compared to the current solution.

14. **Compatibility:** the updated architecture for the valve should be compatible with both CT2 and CT3 wind tunnels.

In summary the project calls for a design that performs as well as the current system does. What will be different in the new configuration, will be the need for human intervention and consumables for the operation of the valve, which are to be avoided.

Chapter 3

Possible solutions

3.1 Literature review of fast-acting valves

The purpose of this literature review is to scout for fast acting valve solutions that have been adopted in similar applications, in order to inform the design by understanding previous work. The review will cover the solutions adopted in shock tubes, Ludwieg tubes and some case studies of turbomachinery wind tunnels similar to CT2 and CT3.

The work done by Janardhanraj et al. [5] displays and summarizes fast-acting valves used in shock tubes and Ludwieg tunnels in different categories. Each valve has three main attributes: the closure element, the actuation mechanism and the orientation of the driver (high pressure) and driven (low pressure) sections. The closure element initially isolates the driver and driven sections, sealing the passage that connects them. When the actuator is engaged, the closure element is retracted, uncovering the passage and connecting the two sections. The closure element is either a piston, plate, sleeve, cap or membrane. The actuation mechanism is responsible for the rapid movement of the closure element. The exerted force should be enough to overcome friction, seating, and pressure forces, and to guarantee high acceleration of the closure element. The main types of actuator are listed in table 3.1, along with advantages and disadvantages for actuation systems.

Janardhanraj et al. [5] then proceed with reviewing the different geometries that have been reported in literature. In figure 3.1 various type I configurations are shown. None of these geometries are suitable for our applications, as all of them require the flow to take a 180° turn to enter the test section, which would also generate high pressure losses.

Table 3.1: Comparison of different systems used for valve actuation [5].

Actuation System	Advantages	Disadvantages
Hydraulic	Powerful, safe, self-contained.	Fast over short strokes, high maintenance, risk of leaks.
Pneumatic	Fast over long strokes, economical, simple design.	Limited power, short cycle life, gas requirement.
Electric	Quick and fast response, precise control, clean operation, no leaks.	Low power, complicated design, expensive.
Electromagnetic	Reliable and robust, miniature and remote operation, cost-effective.	Electromagnetic interference, sensitive to voltage, limited force.

Type II configurations are illustrated in figure 3.2. Type II(b) configuration is reported in the review to be the most common one used in Ludwig tubes. All of them could be implemented to obtain clean flows and low losses by accurately shaping the closure elements and the side passages of type II(c). Unfortunately, though, none of these configurations are applicable, as they would require major modifications to the facilities. Configurations II(a) and II(d) and II(c) would require installing actuation the system and moving closure inside of the compression tube, potentially obstructing the flow or reducing the available travel of the compression tube itself, further shortening the test times. Configuration II(b) would also require major modifications to the wind tunnels, as the center of the annular settling chamber of CT3 is currently where part of the cooling circuit sits. Although the configurations II(a) and II(b) have been reported in use cases of turbomachinery blow-down wind tunnel, as we will further discuss in the case study [6] and as reported in [7], they don't seem to fit with the requirements of this project.

The same considerations hold true for type III valves, displayed in figure 3.3, which would require installation of components inside the compression tube.

Type IV configurations, reported in figure 3.4 are not compatible with the "in line" driver-driven configurations of CT2 and CT3 wind tunnels, so they are not suitable for this project.

Type V(a) configuration, displayed in figure 3.5 is the current configuration of the valve, and type V(b) is reported to have been successfully implemented in [8]. In spite the halving of the required closure element travel (which translates in lower opening times) that type V(b) offers compared to type V(a), it comes at the cost of potential synchronization issues of the two closure elements and with the added

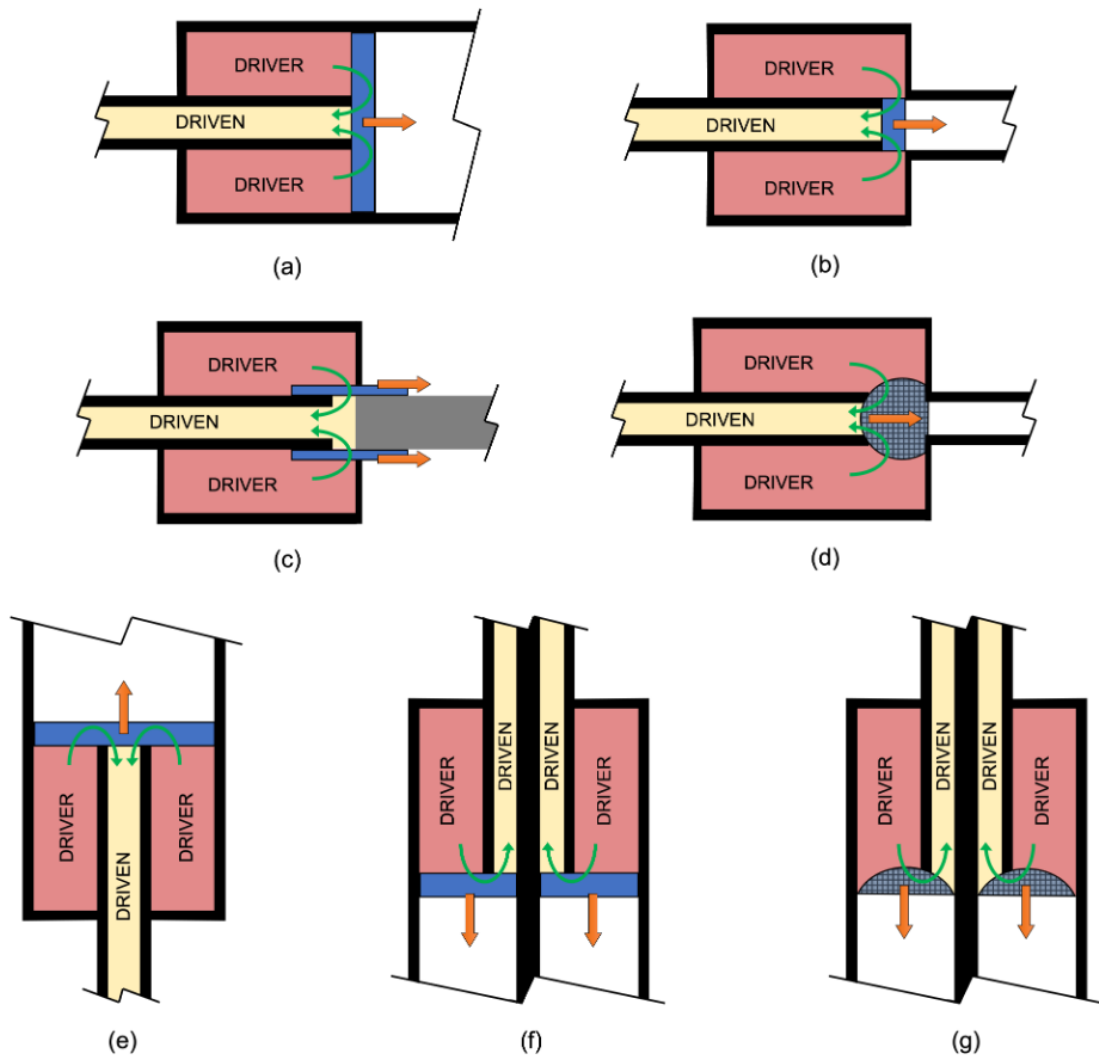


Figure 3.1: Simplified diagram of type I valves [5].

potential leaking interface between the two. Since a reduction of opening time is not paramount for this project, because of the added complexity of the system, and because this solution does not seem to be conclusive with respect to the issues that plague the current solution, configuration V(b) is also discarded.

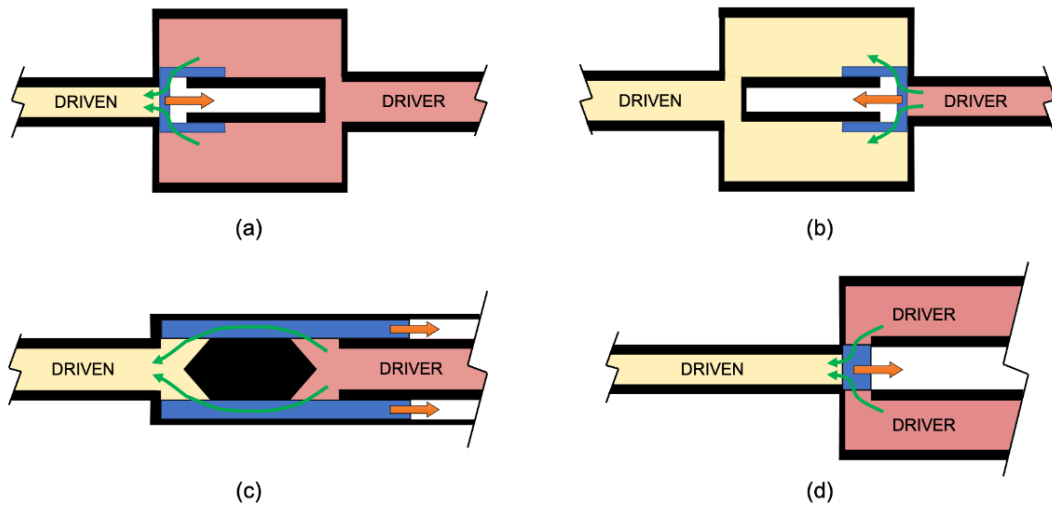


Figure 3.2: Simplified diagram of type II valves [5].

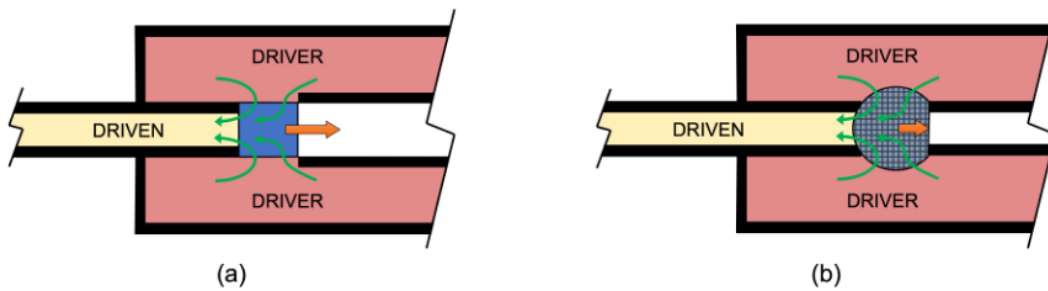


Figure 3.3: Simplified diagram of type III valves [5].

3.1.1 Case studies

In this section we will focus on the analysis of some case studies of the applications of fast acting valves.

High Density Tunnel at The University of Oxford

The High Density Tunnel at The University of Oxford [9] [6] is a Light Isentropic Compression Heating (LICH) tunnel that can be operated in either Ludwieg Tube or LICH tube, with the possibility of using electrical heaters to heat up the test gas. A 17.4 m long and 152.4 mm in diameter tube is used as the reservoir in Ludwieg Tube mode and as the compression tube in LICH mode. The tube is attached to a nozzle via a fast-acting valve, and the nozzle is connected to the test section and to a vacuum dump tank. The facility is used for supersonic and hypersonic testing,

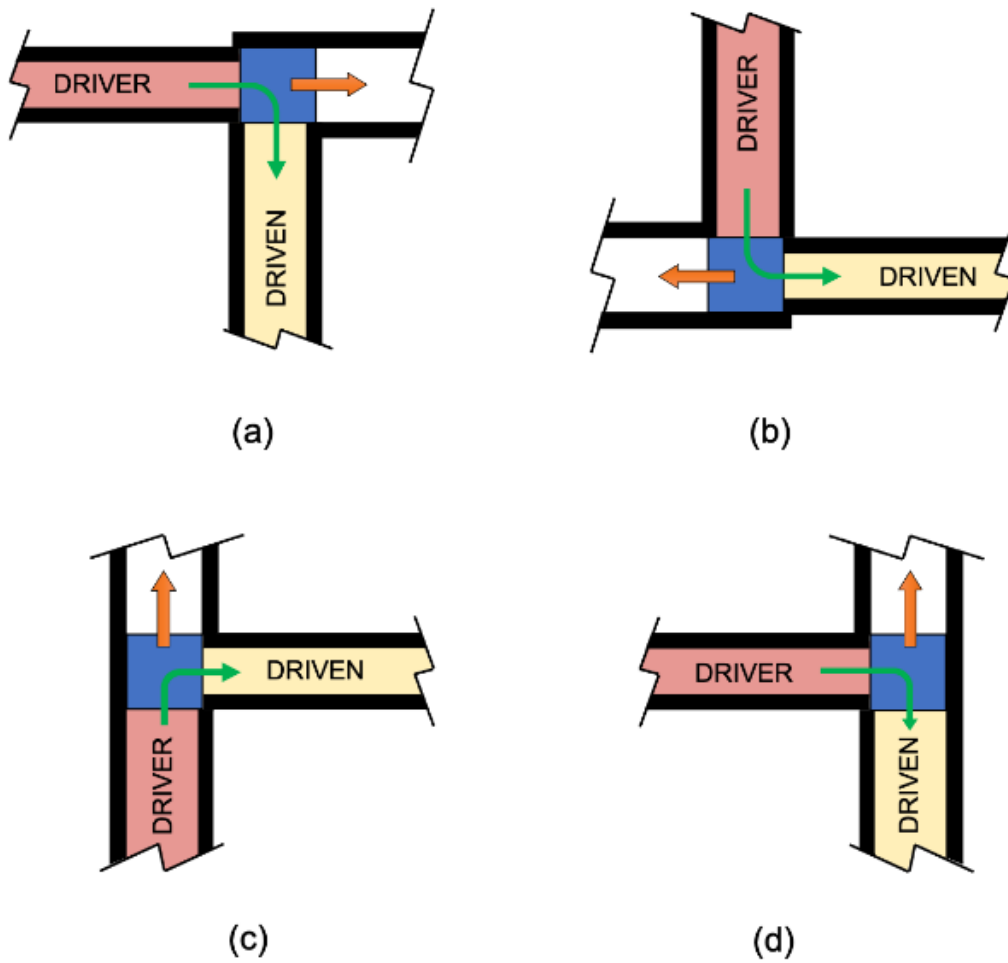


Figure 3.4: Simplified diagram of type IV valves [5].

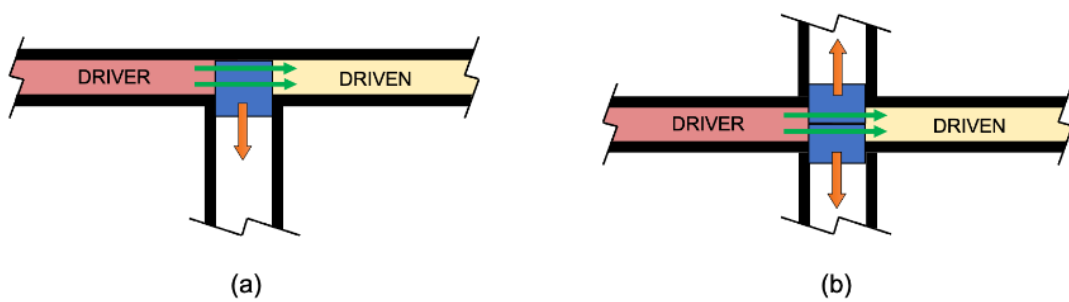


Figure 3.5: Simplified diagram of type V valves [5].

and in LICH mode with heating can safely reproduce Mach 7 flows with stagnation conditions of 750 K and 90 bar.

The fast-acting valve is a plug valve, shown in figure 3.6, in configuration type II(b) (figure 3.2).

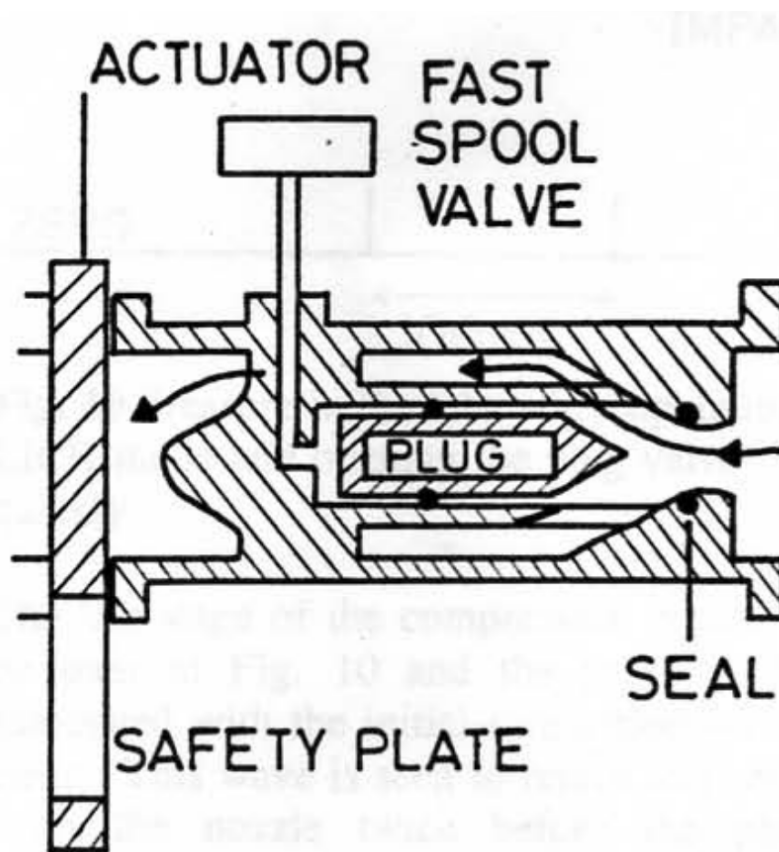


Figure 3.6: Section view of the fast-acting plug valve of the Oxford HDT in the closed state [6].

The plug is held closed by the pressurized air in the chamber that sits behind it, and the opening is prompted by a fast acting spool valve, which vents the pressurized air in the chamber. The plug is moved by the difference in pressure between the pressurized test gas upwind and the venting gas behind it. The time constant of the plug valve is ~ 10 ms, despite it being relatively massive, due to the high operating pressures. The venting process of the chamber that holds the plug closed can be adjusted in order to control the plug opening. In LICH mode, the pressure inside the compression tube is measured during the compression phase and a Programmable Logic Controller continuously predicts the pressure, so that the opening signal is emitted accounting for the operating time of the valve and of the spool valve which controls it. The valve is quickly shut close to preserve most of the pressurized gas in the reservoir when operated in LICH mode.

The Purdue Experimental Turbine Aerothermal Laboratory

The Purdue Experimental Turbine Aerothermal Laboratory [10] is another facility used for both continuous and transient, linear and annular cascade turbine testing. It is equipped with three different heated test gas lines to control the main flow, cooling flow and a third gas stream. It can operate at wide ranges of Reynolds, with inlet pressures ranging from 0.5 to 6 bar and temperature between 270 and 700 K. The test section and the air supply is connected to the test section and dump tank by a fast-acting butterfly valve, actuated by a Kinetrol actuator. The test times are much longer than the ones provided by VKI's CT2, CT3 and Oxford's HDT, at about 30 s. This is enabled by the large volume of the dump tank, of 283 m^3 . As listed on Kinetrol's website [11], the opening time of the valve is of about 2 s.

At first glance the butterfly valve is an interesting solution that could be implemented in CT2 and CT3 facilities without requiring other major changes. The solution is compatible with the linear layout of the facilities and can fit within the tight space where the current solution resides. The issues with this solutions start with the opening times, which, even for commercial applications, are not compatible with the time scale of VKI's facilities. Another problem would be the partial obstruction of the test gas passage by the body of the valve, and by its seals, which need to protrude from the walls of the duct. Considering isentropic flow laws and perfect gas laws for air applied to the CT3 facility, with a 280 mm diameter flow passage, total test gas conditions at 2.5 bar and 350 K, a test mass flow of 25 kg/s and a 5 cm wide cross-section of the body of the valve, the Mach number around the valve body can reach 0.82 (without the obstruction it would be 0.5). This could lead to shock formation around the body of the valve, spoiling the flow and generating high pressure losses that are unsuitable for the requirements of this project.

3.2 Chosen solution for CT2 and CT3

For this project, the solution that was ultimately chosen is to retain the current architecture and workings of the valve but modifying the locking mechanism. This choice was made because the valve in its current state already satisfies all the requirements, except for the usage of consumables and dangerous materials and for the automatization. A system that could replace the current outdated locking mechanism, that could be automated, with low latency and high consistence and repeatability is in essence the new objective of the project. The main challenge is posed by the extremely high loads that have to be released in a fraction of a second.

Chapter 4

Updated requirements and constraints

After reviewing the requirements and constraints in light of the new objective, and excluding those that are already met by the preserved elements of the current system, we can now outline the essential criteria that the locking system must adhere to.

1. **The new solution should not rely explosives, consumables or hazardous materials.** This requirement is key to the objective of this project, as the current valve architecture requires that the operators of the wind tunnel handle explosive and replace consumables, which is both dangerous and a waste of time and resources.
2. **The valve should be safe during all anomalous circumstances** such as power outages.
3. **The valve should never need inspecting while the systems are pressurized or ready to go off for tests.** This means that the valve should be made so that the risks of it being stuck closed are minimized.
4. **The valve should be easy to operate**, enabling low training time and lowering chances of injury and malfunction. This means that ideally the valve should be **automatized** and remotely operated.
5. **The valve should reliably open with low run to run variance.** This is crucial to have the facilities working at their best and producing repeatable and accurate results. A high variance in opening times or delay would significantly impact key parameters, such as total inlet temperature and pressure.

6. **The valve should open in 0.1 s**, as is the case with the current valve architecture, and **with low delays between signal and actual execution**. If delays are unavoidable but consistent with every test, it may be an option to account for them and have the opening signal at a pressure value inside the compression tube lower than $P_{initial}$, so that during the delay the pressure level rises to $P_{initial}$.
7. **Down-time**: the valve should work reliably for 10 years, without major servicing. During the 10 years period, conservatively expecting 10 tests/day every day, 36500 total runs can be expected. The routine servicing should not exceed about 6-12 h/year, in line with the current setup. To achieve this, the parts that need routine servicing should be easily accessible.
8. **Power source**: the adopted solution should be powered by sources already available at the facility. The building is equipped with 230 V AC and 400 V AC three-phase, and different pneumatic lines at 7, 16, 40 and 150 bar. The 7 bar line would be the easiest to access, as the current valve solution is powered by it.
9. **The system should fit where the current system sits**, allowing minimal changes to the facility.
10. **Budget**: although a specific amount is not specified, the budget required for the development and installation of the new solution should be proportional with the benefits that it would bring compared to the current solution.
11. **Compatibility**: the updated architecture for the valve should be compatible with both CT2 and CT3 wind tunnels.

Chapter 5

Pneumatics Modeling

In accordance with the requirements, the power source for all the mechanisms is going to be the 7 bar pneumatic line that already powers the valve's main actuator, thanks to a reservoir installed in the underground hatch below the valve (for CT3). We will now discuss the modeling of pneumatic actuators, which will be later used to compute reaction times of the systems and to fully simulate their behavior. For this analysis, the work from Richer et al. [12] was used as a starting point.

5.1 Hypothesis and equations

Here follows a list of the hypothesis made to develop the model for a pneumatic actuator:

1. **Perfect gas:** the air in the pneumatic system is going to be treated as a perfect gas, where $pV = mRT$, where p is the pressure, V is the volume, m is the mass and T is the temperature of the gas, while $R = 287.09J/kg/K$ is the perfect gas constant for dry air.
2. **Energy equation:** Richer et al. [12] uses the energy equation written as follows:

$$q_{in} - q_{out} + \gamma C_v (\dot{m}_{in} T_{in} - \dot{m}_{out} T_{out}) - \dot{W} = \dot{U} \quad (5.1)$$

where q_{in} and q_{out} are heat exchange terms, γ is the specific heat ratio, C_v is the specific heat at constant volume, $\dot{m}_{in} T_{in}$ is the mass-flow into the actuator chamber multiplied by its temperature, $\dot{m}_{out} T_{out}$ is the mass-flow out of the actuator chamber multiplied by its temperature, \dot{W} is the mechanical power, and \dot{U} is the change of internal energy. Richer et al. [12] further develop this

expression for an adiabatic and an isothermal case, and by comparing them they obtain:

$$\dot{p} = \frac{RT}{V}(\alpha_{in}\dot{m}_{in} - \alpha_{out}\dot{m}_{out}) - \alpha\frac{p}{V}\dot{V} \quad (5.2)$$

where \dot{p} is the time variation of pressure inside the chamber of the actuator and \dot{V} is the rate of change of the volume of the chamber. α_{in} , α_{out} and α are coefficients that depend on the actual heat transfers during the processes, which vary between 1 and γ . The authors suggest to use values of α_{in} close to γ , α_{out} close to 1 and α close to 1.2. For the sake of our analysis, the values used are $\alpha_{in} = \gamma$, $\alpha_{out} = 1.1$ and $\alpha = 1.2$.

3. **Isentropic flow:** this hypothesis was used to calculate the mass flow rates \dot{m}_{in} and \dot{m}_{out} based on the pressure ratio between the chamber and the environment which it is exposed to (either the 7 bar feed line or atmospheric conditions). The following equations apply to a scenario where the chamber (pressure p) is connected to the feed line (pressure p_{in}) and has a lower pressure than that of the feed line. From the pressures we can evaluate the mach number M as the gas flows from the feed reservoir to the chamber, which is considered to be sonic at the most:

$$M = \sqrt{\frac{2}{\gamma - 1} \left[\left(\frac{p_{in}}{p} \right)^{\frac{\gamma-1}{\gamma}} - 1 \right]} \leq 1 \quad (5.3)$$

Now the mass flow can be evaluated:

$$\dot{m}_{in} = C_d \cdot \frac{p_{in} A_t}{\sqrt{RT}} \cdot \frac{\sqrt{\gamma} M}{\left[1 + \frac{\gamma-1}{2} M^2 \right]^{\frac{\gamma+1}{2(\gamma-1)}}} \quad (5.4)$$

where C_d is the discharge coefficient, assumed to be 0.4, as 0.5 is a typical value for spool valves used to actuate pneumatic system [13], and A_t is the cross-section of the feed line. The model has been implemented so that regardless of the environment connected to the considered chamber, the connection can act both as an inlet and as outlet, depending on the pressure conditions of the chamber.

4. **Losses:** the actuators are assumed to be free of any air leaks between chambers. However, to replicate the behavior of the main actuator of the CT3 shutter valve, high damping constants and static friction forces were considered. These are likely due to the high-speed movement of the components and the numerous seals that create friction between stationary and moving parts.

5.2 Implementation and parameter calibration of the model

The simulation aims at reproducing the behavior of the CT3 shutter valve actuator, as this is a case where every aspect of the geometry is known, as well as the inertial loads, initial conditions and the resulting displacement over time. Every parameter of the simulation can be at the very least estimated, except for the damping coefficient β , which will be determined as a result of this analysis. The simulation is performed with a time-stepping loop, where each iteration updates the physical state of the actuator based on the previous state. As parameters of the actuator in the current time step are computed, these are used to update other parameters.

The loop starts with updating the gas conditions in both chambers, using the isentropic flow and perfect gas equations. Assuming i the to be the current time-step and dt its duration, in the case of the top chamber of the actuator, connected to the feed line, the flow direction is evaluated by comparing the pressure in the chamber p_{i-1} with p_{in} . If $p_{in} > p_{i-1}$ then the Mach number at the throat of the feed line is computed as:

$$M = \sqrt{\frac{2}{\gamma - 1} \left[\left(\frac{p_{in}}{p_{i-1}} \right)^{\frac{\gamma-1}{\gamma}} - 1 \right]} \leq 1 \quad (5.5)$$

The mass flow is then computed as

$$\dot{m}_{in} = C_d \cdot \frac{p_{in} A_t}{\sqrt{RT_{i-1}}} \cdot \frac{\sqrt{\gamma} M}{\left[1 + \frac{\gamma-1}{2} M^2 \right]^{\frac{\gamma+1}{2(\gamma-1)}}}, \quad (5.6)$$

and thus $\dot{m}_{out} = 0$. The mass is then updated, assuming the mass flow to be constant during the time step.

$$m_i = m_{i-1} + \dot{m}_{in} dt \quad (5.7)$$

The pressure variation is evaluated as

$$\dot{p} = \frac{RT_{i-1}}{V} (\alpha_{in} \dot{m}_{in} - \alpha_{out} \dot{m}_{out}) - \alpha \frac{p_{i-1}}{V_{i-1}} \dot{V}_{i-1} \quad (5.8)$$

where \dot{V}_{i-1} is computed as the velocity of the piston v_{i-1} multiplied by the surface area of the piston for the considered chamber, in this case s_t , and the pressure in the chamber is also updated assuming constant \dot{p} during dt :

$$p_i = p_{i-1} + \dot{p} dt \quad (5.9)$$

and finally:

$$T_i = \frac{p_i V_{i-1}}{m_i R}. \quad (5.10)$$

If $p_{in} < p_{i-1}$ then the flow is considered reversed, and the equations to find the Mach number and the mass flow are accordingly changed. The same equations can be used to update the conditions of the gas in the bottom chamber, keeping in mind that it is vented to the atmosphere. At this point the force exerted by the piston can be calculated as

$$F = p_{i,t}s_t - p_{i,b}s_b - \beta v_{i-1} + mg, \quad (5.11)$$

where s_t and s_b are the surfaces of the piston in the top and bottom chambers, β is the damping coefficient and mg is the weight force due to the mass of moving components. Static or dynamic friction forces are conditionally applied depending on v_{i-1} . The acceleration, velocity and position of the piston, along with all other moving parts of the shutter is calculated as follows:

$$a_i = \frac{F}{m_v}; \quad (5.12)$$

$$v_i = v_{i-1} + a_i \cdot dt; \quad (5.13)$$

$$x_i = x_{i-1} - v_i \cdot dt - \frac{1}{2}a_i \cdot dt^2. \quad (5.14)$$

Force, acceleration and velocity are considered positive downward, while the position x is positive upward, and going from 0 at the bottom position to maximum displacement x_{max} at the top. Based on the displacement of the new position, the new volumes of the chamber can be computed as

$$V_{i,b} = V_{bc} + s_b x_i \quad (5.15)$$

$$V_{i,t} = V_{tc} + s_t(x_{max} - x_i) \quad (5.16)$$

where V_{bc} and V_{tc} are the dead volumes of the two chambers.

The results are presented below, obtained with $\beta = 1100 \text{ Ns/m}$.

As stated before, the high value of β is likely due to the many sliding rubber seals that are present throughout the system. In figure 5.6, the resulting displacement from a simulation where β was assumed to be 0 is reported : it is clear that the effect of the damping cannot be solely attributed to the built in dampener in the cylinder assembly. This is explained by the fact that it starts obstructing the venting area of the bottom chamber at $\sim 85 \text{ mm}$ of displacement, while the effect of damping is already clearly visible at 300 mm .

The actuator model gives results in line with expectations: from figure 5.4, 5.1, 5.2 and 5.3 it is possible to see that the rapid expansion of the top chamber leads to rapid pressure and temperature drops, while the mass inside the chamber grows slowly but steadily. The opposite is true for the bottom chamber.

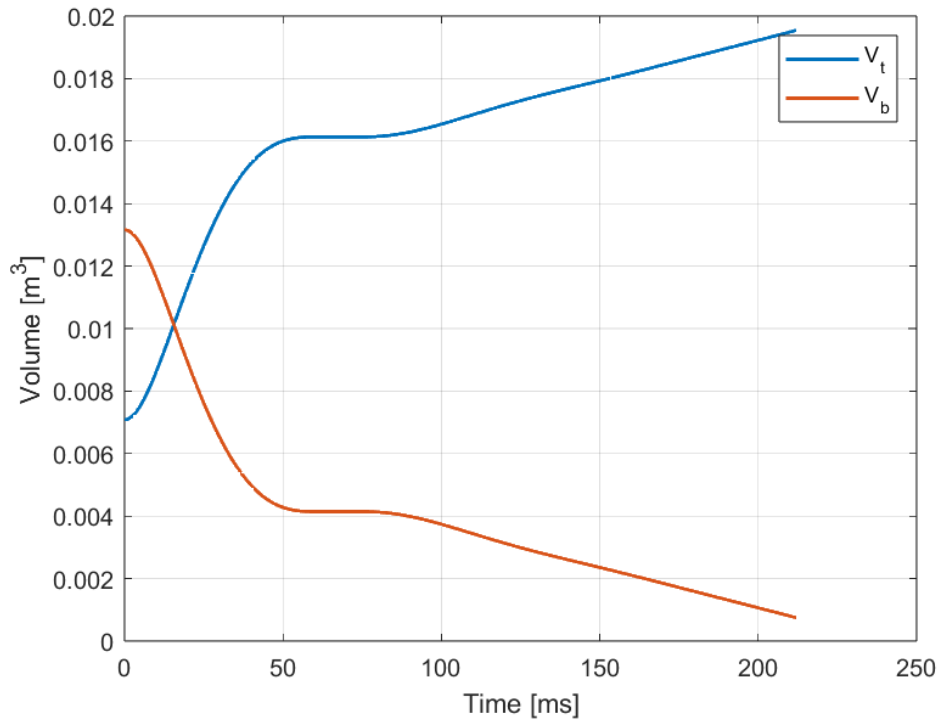


Figure 5.1: Volumes of the chambers.

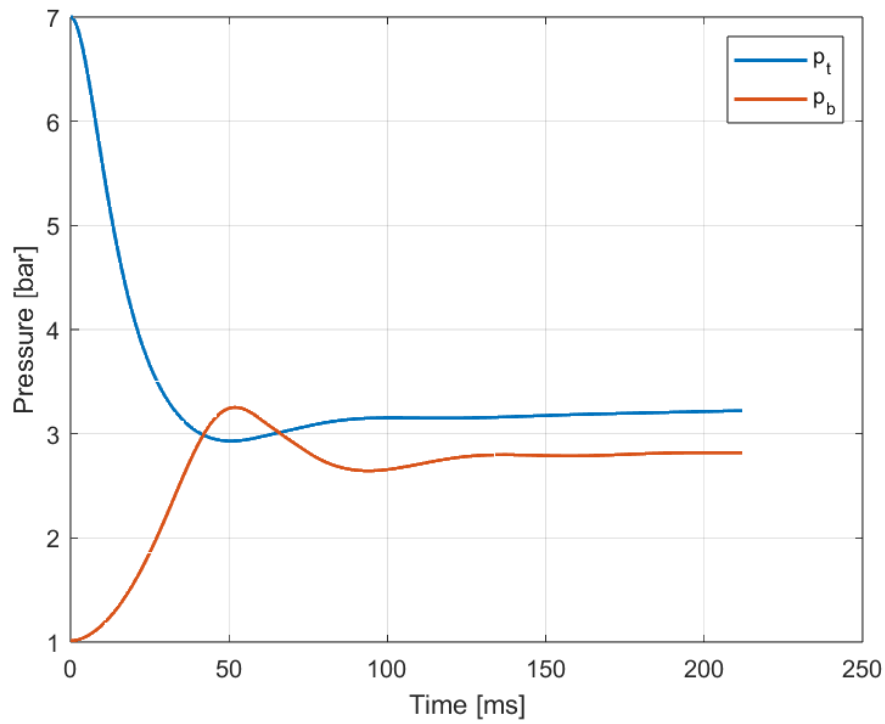


Figure 5.2: Pressures in the chambers.

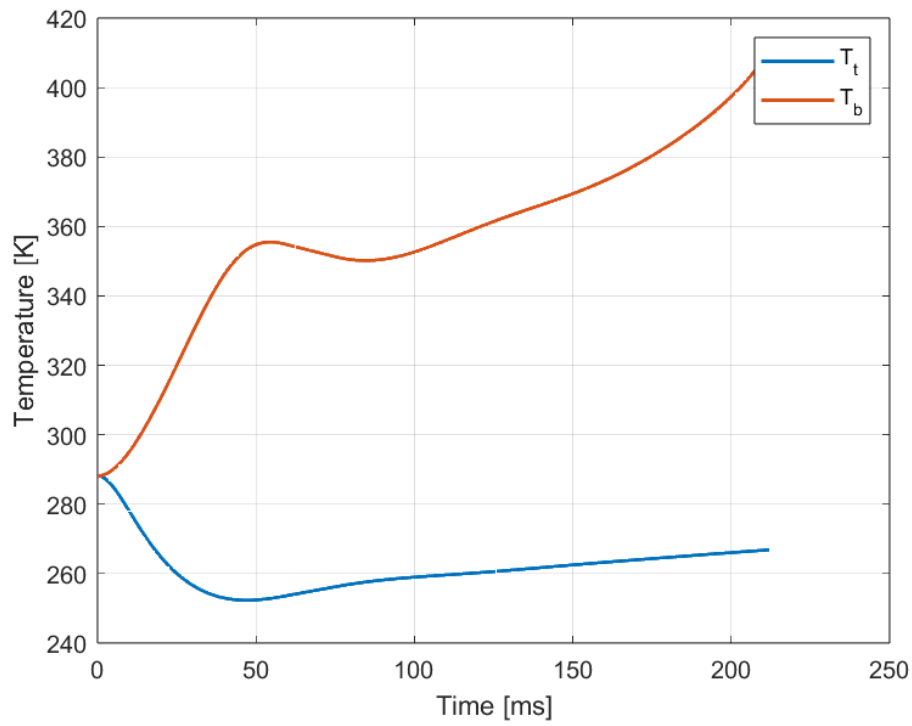


Figure 5.3: Temperatures in the chambers.

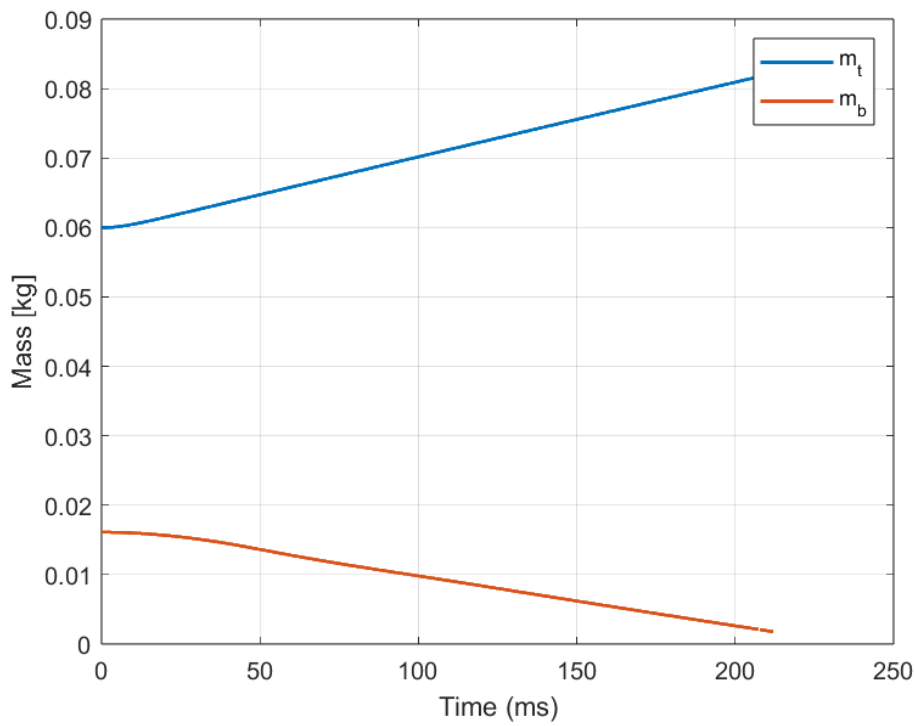


Figure 5.4: Mass of air in the chambers.

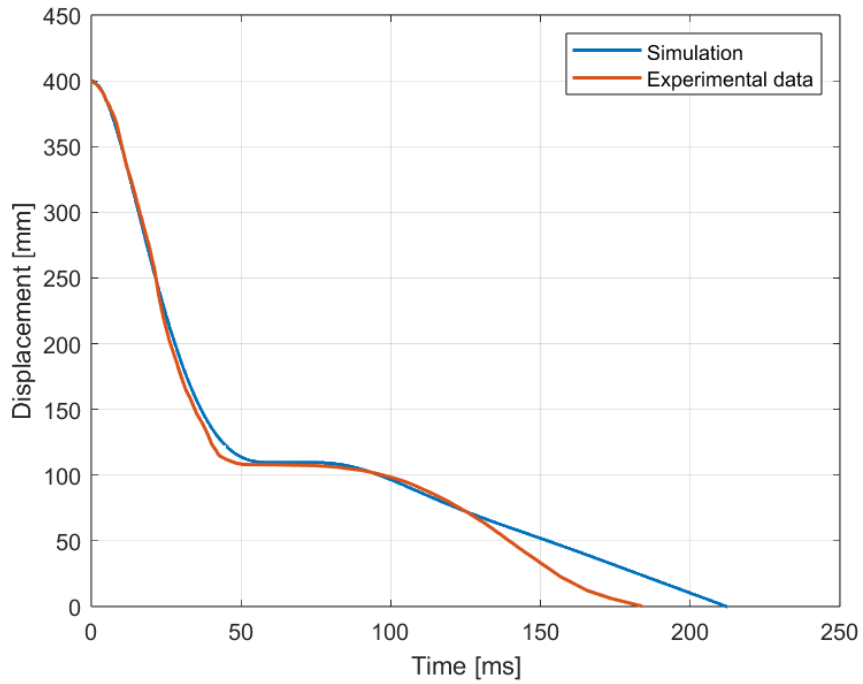


Figure 5.5: Comparison between experimental data (from figure 1.9) and simulation

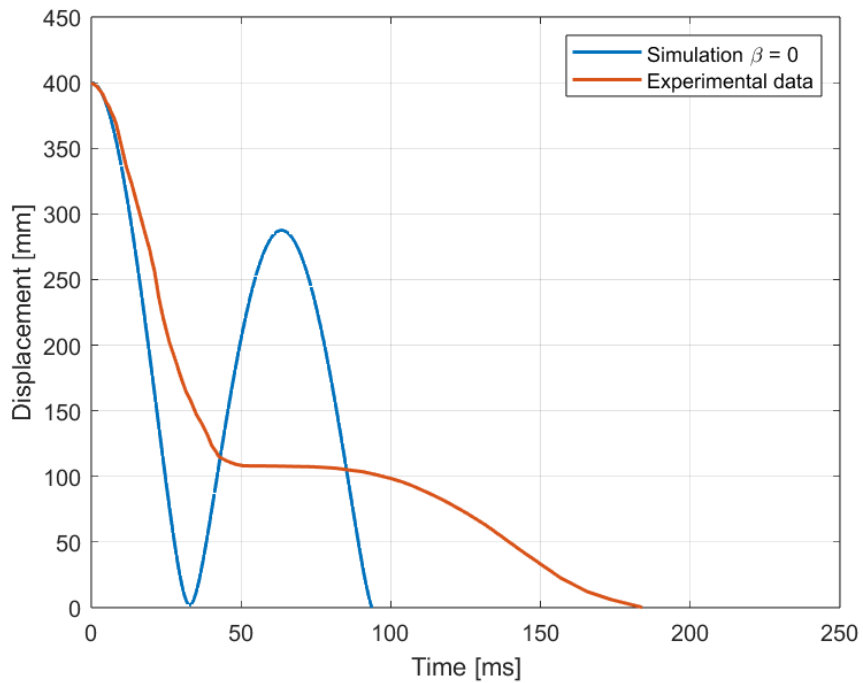


Figure 5.6: Comparison between experimental data (from figure 1.9) and simulation, $\beta = 0$

Chapter 6

Investigated solutions

All of the solutions were anticipated to be installed where the current locking mechanism sits, so this would mean at the end of the valve's rod, below the main valve actuator, and possibly mounted to it. For the sake of consistency, a color code will be adopted and used in drawings and sketches throughout the analysis of the investigated systems. The components that will be attached to the valve's rod end will be drawn in black, and their movement will be assumed to be constrained to be only translational in the vertical direction, in accordance with the motion of the valve. Green components will be those that are fixed to the bottom of the valve's main actuator, and thus they will have no motion with respect to a static observer. Red components will have the role of locking the valve in its closed position, and their movement will depend based on the solution analyzed.

6.1 Angled locking pin

6.1.1 General description

Looking at figure 6.1, the concept of this solution is to have a locking body (the pin, in red) that comes into contact with the valve's rod end at an angled surface, with angle to horizontal α . The load of the pre-pressurized valve's main actuator is supported by the pin's body at the angled surface, and transferred through contact forces to the green supporting structure. The pin will be connected to an actuator on the right, that is going to be fixed to a non-moving support structure, which is likely going to also include the green lateral guide that surrounds the valve's rod end. By sliding to the right, pulled by the actuator, the pin will allow the valve's rod end to move downward, and thus the valve will open. Having an angled surface is advantageous compared to having a horizontal surface, because it enables

instantaneous movement of the valve (downward) as soon as the pin starts moving to the right.

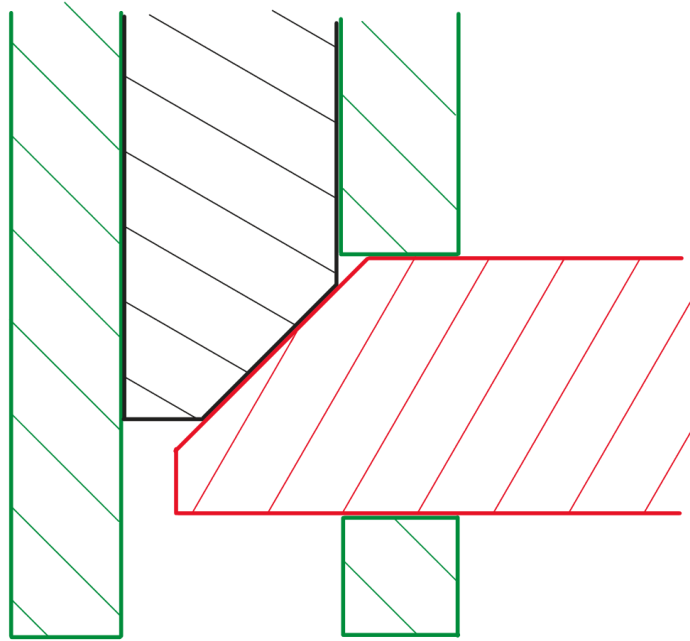


Figure 6.1: Simplified diagram of the angled locking pin (valve is closed). The sketch is not representative of proportions or any other quantitative factor, it should only be used for the general understanding of the concept.

6.1.2 Simplified modeling

The fastest opening time can be achieved if the pin does not touch the rod's end at all during the opening, so the best scenario would be to have the pin accelerate to the right faster than the valve accelerates down. The lowest reaction times can be achieved if both chambers of the actuator moving the pin are vented to atmosphere while the valve is held close, and at the opening time the smallest chamber is pressurized to provide the necessary force to move the pin. To find a suitable α value to have static equilibrium without any pushing force from the pin's actuator, it is sufficient to solve the inclined plane, and obtaining

$$\alpha = \arctan(\mu(1 - S)) \quad (6.1)$$

where μ is the static friction coefficient, ranging from 0.1 to 0.9 and $S = 0.3$ is a safety margin. S lets us select a safe α value, keeping in mind that friction coefficients are difficult to measure and are affected by many environmental factors.

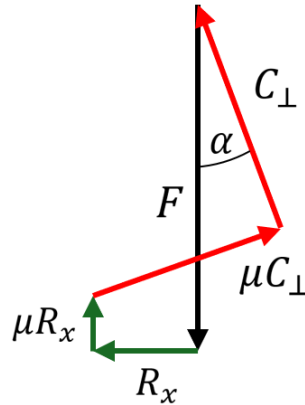


Figure 6.2: Force diagram for the static equilibrium of the valve's rod end at incipient movement (where friction forces are at their maximum values). In red the forces exerted by the pin, in green the ones exerted by the guide, and in black the one exerted by the valve's actuator.

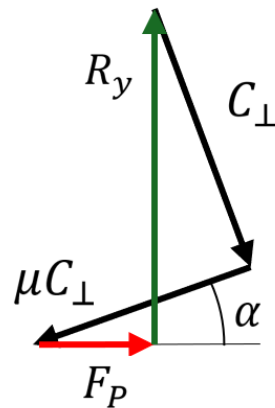


Figure 6.3: Force diagram for the static equilibrium of the pin at incipient movement (where friction forces are at their maximum values). In red the forces exerted by the pin's actuator, in green the ones exerted by the pin's guide, and in red the one exerted by the pin's actuator.

Figure 6.2 shows the equilibrium of forces for the valve's rod end. From this diagram we can write the vertical and horizontal equilibrium equations, which result in:

$$R_x = \frac{F - \mu C_{\perp} \sin \alpha - C_{\perp} \cos \alpha}{\mu} \quad (6.2)$$

and

$$C_{\perp} = \frac{F}{\mu \left(\sin \alpha (1 + \mu) + \cos \alpha \left(\frac{1}{\mu} - 1 \right) \right)}, \quad (6.3)$$

where C_{\perp} is the perpendicular force at the contact interface between the pin and the valve's rod end, and μC_{\perp} is the resulting friction force. Figure 6.3 shows that neglecting the friction forces related to the vertical support, the minimum force required to extract the pin from under the valve's rod end would be equal to

$$F_{P,min} = C_{\perp}(\mu \cos \alpha - \sin \alpha), \quad (6.4)$$

while the minimum force necessary to accelerate the pin faster than the valve in order to avoid contact or slip is:

$$F_{P,ns} = m_{pin} \frac{a_v}{\tan(\alpha)}, \quad (6.5)$$

where m_{pin} is the mass of the moving parts of the pin and a_v is the downward acceleration of the valve at the start of the opening. F_{min} and F_{ns} have been computed for the α angles obtained from equation 6.1 and then converted in actuator diameters in figure 6.4, assuming that one chamber is at 7 bar and the other at atmospheric pressure.

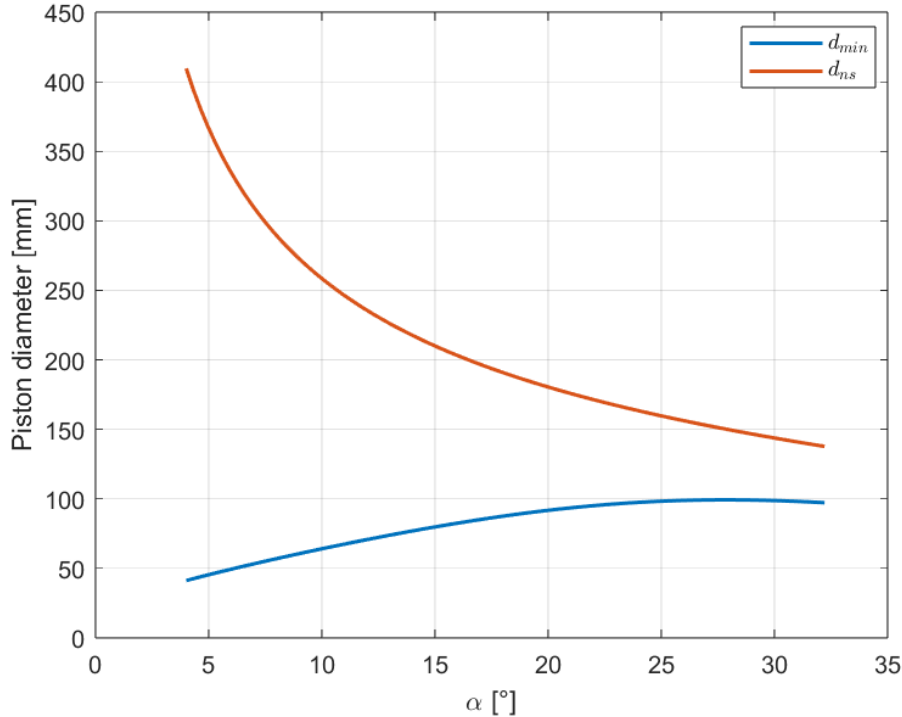


Figure 6.4: Piston diameters for starting the pin's motion (d_{min}) and to accelerate it to avoid slip (d_{ns}).

6.1.3 Negative outcome

Figure 6.4 shows that the force required to accelerate the pin is always going to be greater than the one required to start the pin's motion. The fundamental workings of pneumatic actuators, where the change in force is not instantaneous and requires time, the actuator would first reach the force level required to overcome the friction. Since the force required to achieve the "no slip" condition is higher, the pin is going to move right, pushed aside by the valve's rod, which is in turn slowed down. Different solutions where the valve itself is responsible for removing the locking device are explored in the following sections.

6.2 Brake

6.2.1 General description

This system uses a geometry similar to the one for the locking pin, as displayed in figure 6.5, but the fundamental workings are different: in the closed configuration, a pneumatic actuator pushes the red locking body, now a brake, on the inclined surface of the black valve's rod end. It, in turn, pushes against the green support, which is considered to also be a braking surface. At the interfaces where these forces are exchanged, the resulting drag forces prevent the valve from sliding open. When the valve needs to open, the brake's actuator switches the pressurization, thus decreasing the pushing force. Once it is not sufficient to generate drag forces high enough to keep the valve closed, the valve starts sliding down, pushing the brake to the right. This system can be expected to work at its best if the inclined braking surface is as close as possible to vertical, because this means that the brake is pushed to the right at a slower rate. Because of this, the re-compression in the pushing chamber due to movement will be lower, meaning lower pushing forces and thus lower obstruction of the valve's acceleration is to be expected.

6.2.2 Simplified modeling

Differently from before, α is now considered to be the angle of the contact surface relative to vertical. In the initial condition, the valve is closed and the brake's actuator pushes to the left, in order to generate enough drag to overcome the vertical downward push of the valve. Figure 6.6 shows the forces at play for each of the bodies at incipient movement, where μ is equal to μ_{st} . The braking surfaces materials are considered to be steel on ceramic brake pad material, with typical values of μ_{st}

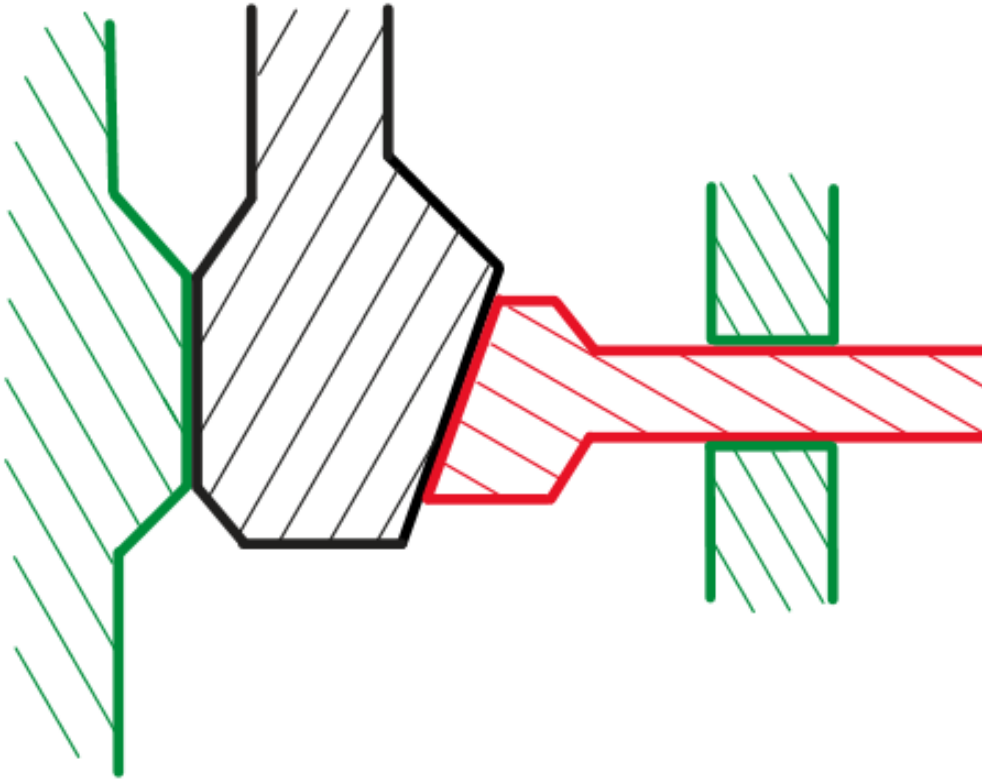


Figure 6.5: Simplified diagram of the brake (valve is closed). The sketch is not representative of proportions or any other quantitative factor, it should only be used for the general understanding of the concept.

of about 0.4. This choice was made as this combination of materials offers somewhat consistent braking performance in time, whereas a steel on steel contact could see the initially very high value of friction coefficient drop significantly as a result of a smoothing of the sliding surfaces as the system is used.

To find the size of the actuator required, the static equilibrium was solved for the bodies. The horizontal and vertical equilibrium for the valve's rod end result in

$$R_x = C_{\perp}(\cos \alpha - \mu \sin \alpha), \quad (6.6)$$

$$\mu R_x - F + C_{\perp}(\sin \alpha + \mu \cos \alpha) = 0, \quad (6.7)$$

and the horizontal equilibrium for the brake is

$$F_p = C_{\perp}(\cos \alpha - \mu \sin \alpha) = R_x, \quad (6.8)$$

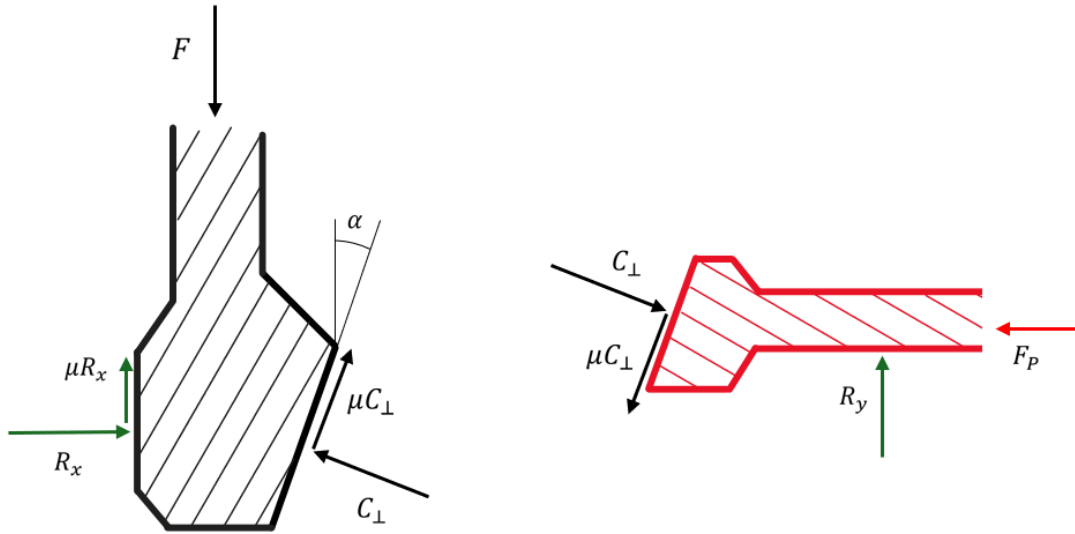


Figure 6.6: Free body diagram of the valve's rod end and of the brake at incipient movement, when the drag forces are at their maximum.

where $\mu = 0.4(1 - S)$ and $S = 0.3$ so to account for the uncertainty in the friction coefficient. Once again, Forces due to the vertical support of the brake have been neglected. F_p is the minimum force required to keep the valve closed. This force is then multiplied by a 1.5 safety factor and converted in actuator size, shown in figure 6.7. The website of FESTO [14], a pneumatic systems component supplier, was used as a reference for estimating some parameters of actuators, such as available sizes, size of connecting pneumatic lines, mass of moving parts and of whole actuators.

6.2.3 Detailed modeling

This section presents the mathematical model and its numerical implementation for a code designed to evaluate the behavior and performance of a brake locking system. The simulation starts at $t = 0$, when the pressure in the brake's actuator feed lines is instantly reversed compared to initial conditions. The bodies are considered to be rigid and the friction coefficients are considered to be $\mu_{st} = \mu_{st,nom}(1 \pm S)$ and $\mu_{din} = \mu_{din,nom}(1 \pm S)$, as well as their nominal values ($S = 0$), where $\mu_{st,nom} = 0.4$ and $\mu_{din,nom} = 0.3$. The same mathematical model and numerical implementation of the pneumatic actuator described previously has been integrated with equilibrium equations for the components to calculate the motion of components and forces, and at every time iteration, the force applied by the brake's actuator $F_{p,i}$ is known. F from the valve's actuator is considered to be constant, but the damping term β will

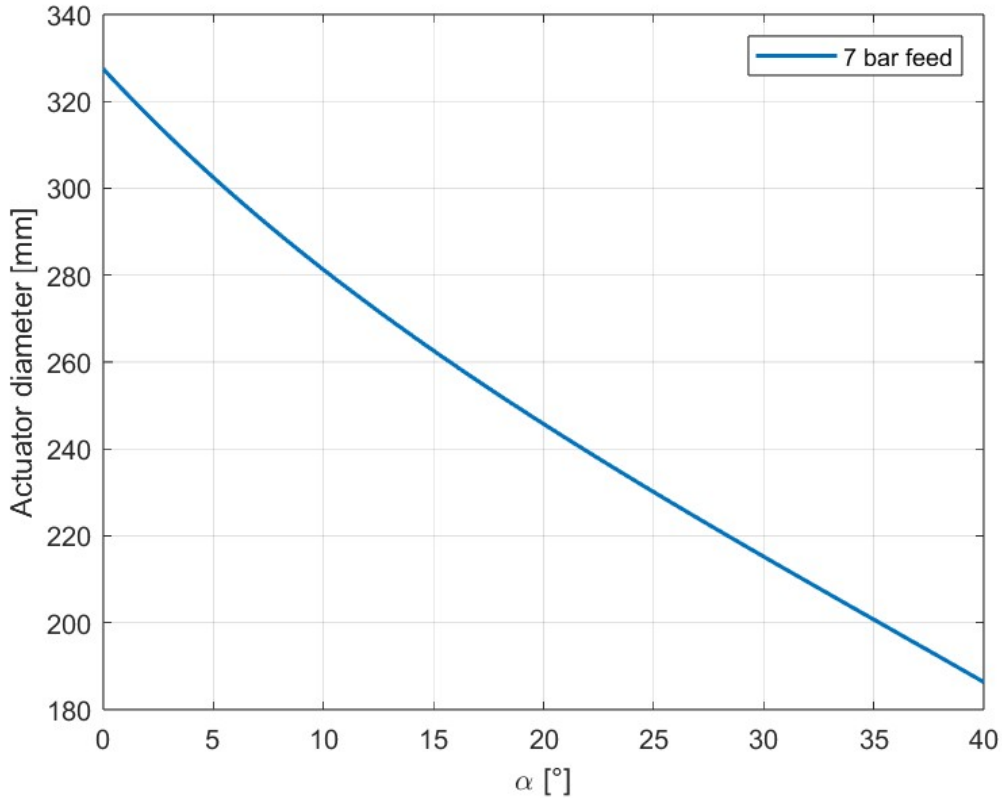


Figure 6.7: Required actuator diameter.

be considered when the valve moves downward.

Static Equilibrium

Because of the 1.5 safety factor considered in sizing the actuator, for a certain amount of time the system is stationary, with F_p lowering but high enough to hold everything still. During this phase, the friction forces can be expressed as a product of the force normal to the considered braking surface and a friction coefficient $\mu < \mu_{st}$. Looking again at figure 6.6, from equation 6.8 we derive

$$C_{\perp,i} = \frac{F_{p,i}}{\cos \alpha - \mu_i \cdot \sin \alpha}. \quad (6.9)$$

This expression for $C_{\perp,i}$, along with $R_{x,i} = F_{p,i}$, where $F_{p,i}$ is known, can be plugged into equation 6.7 to obtain a second degree equation to find μ_i and thus solve the equilibrium. Since everything is stationary, there is no need to update positions and velocities of the bodies.

This is done for every time-step as long as $\mu_i < \mu_{st}$, at which point the system

starts moving and is assumed that $\mu = \mu_{din}$.

Dynamic equilibrium

Looking at figure 6.8 we can write the equations used to evaluate accelerations and forces in the system as it starts moving.

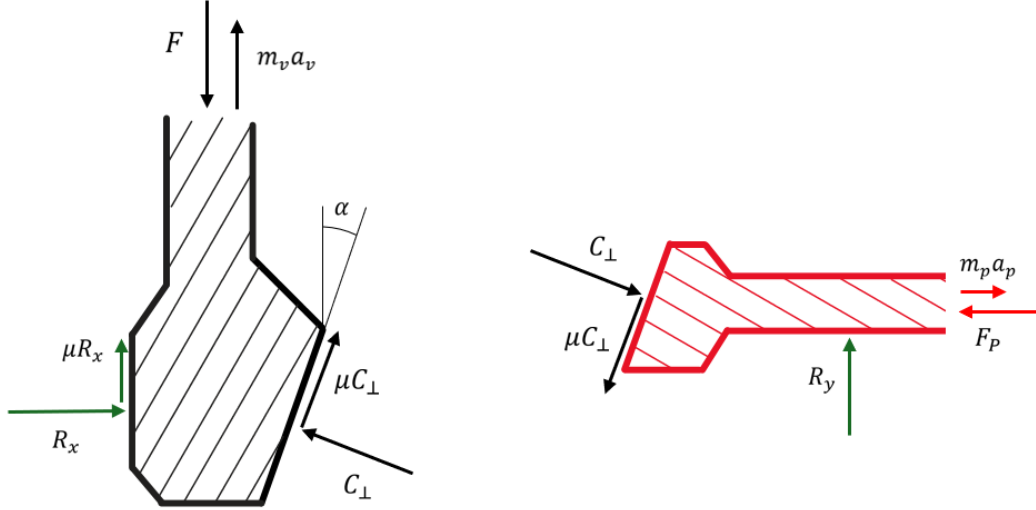


Figure 6.8: Free body diagram of the valve's rod end and of the brake during movement.

The horizontal equilibrium of the brake results in

$$a_{p,i} = \frac{C_{\perp,i-1}(\cos \alpha - \mu \sin \alpha) - F_{p,i}}{m_p}, \quad (6.10)$$

where $a_{p,i}$ is the acceleration of the piston-brake assembly to the right. The slipping between the brake and the rod's end at the inclined surface introduces kinematic relation between the valve's acceleration downward a_v and a_p :

$$a_{v,i} = \frac{a_{p,i}}{\tan \alpha}. \quad (6.11)$$

From the accelerations, the velocities and positions of the brake and the valve can be updated, as well as the volumes of the chambers of the brake's actuator for the next time-step.

From the vertical equilibrium of the rod's end we can find C_{\perp} :

$$C_{\perp,i} = \frac{F - \beta v_{v,i} - m_v a_{v,i}}{2\mu \cos \alpha - \mu^2 \sin \alpha + \sin \alpha}, \quad (6.12)$$

where β is the damping constant for the valve found in chapter 5, v_v and a_v are downward velocity and accelerations for the valve's rod end. Finally, the horizontal equilibrium equation for the brake is used to calculate residuals, to measure the accuracy of the numerical implementation.

$$\text{res}_i = \left| \frac{C_{\perp,i} - \frac{F_{p,i} + m_p a_{p,i}}{\cos \alpha - \mu \sin \alpha}}{C_{\perp,i}} \right|. \quad (6.13)$$

Results

This section presents the performance of a brake system with a 200 mm actuator, $\alpha = 35^\circ$, $m_p = 16$ kg and a dead volume at each end of the actuator, defined as the product of the piston surface on the respective side and the diameter of the port supplying the chamber. Unless explicitly labeled, the results shown are for $\mu = \mu_{nom}(1 - S)$ for both static and dynamic friction coefficients. The subscripts t and b refer the chambers of the brake's actuator, where b would be the right chamber, which starts pressurized and vents, and t would be the left chamber, which starts at atmospheric conditions and is pressurized.

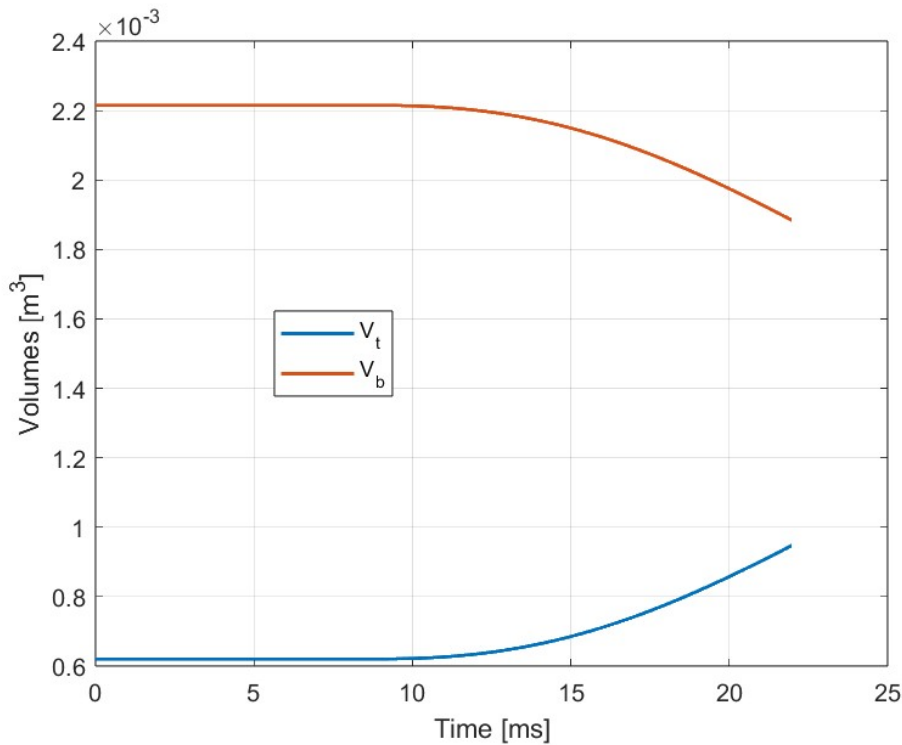


Figure 6.9: Actuator's chamber volumes in time.

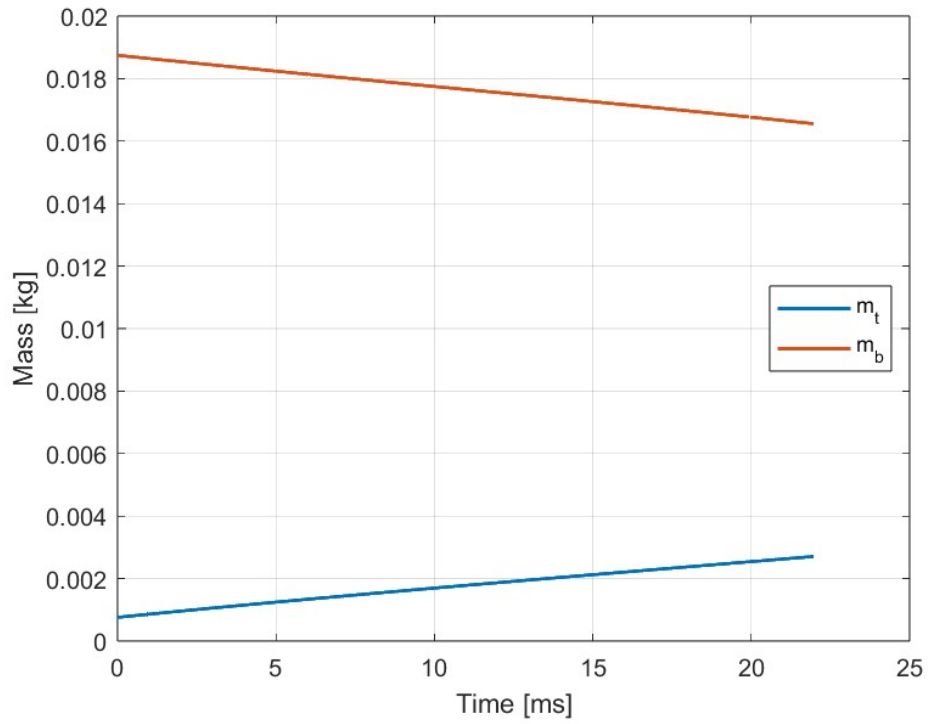


Figure 6.10: Mass of air in the actuator's chambers in time.

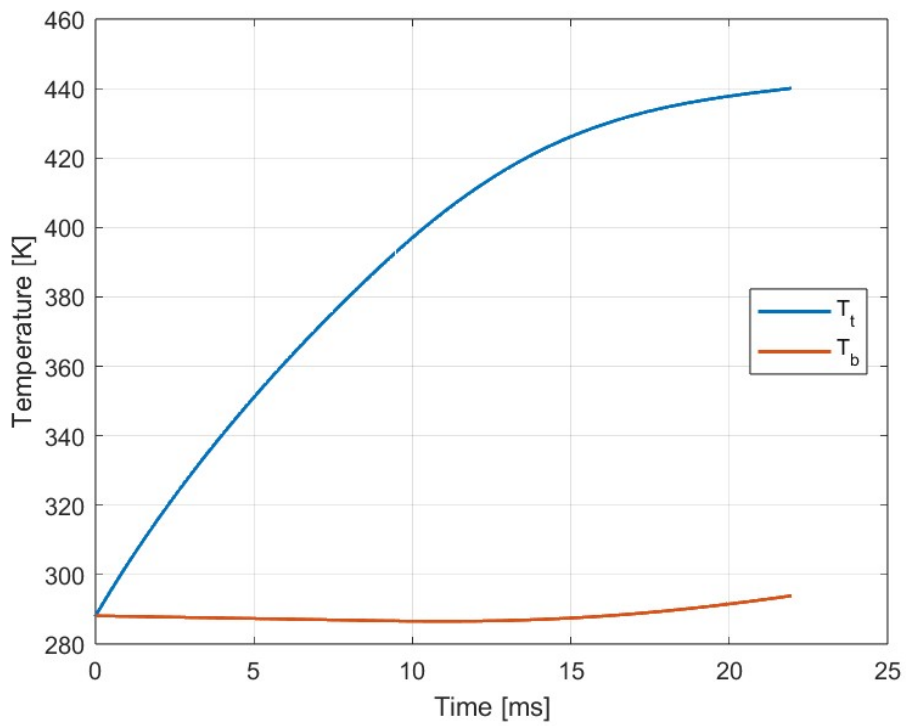


Figure 6.11: Temperature of air in the actuator's chambers in time.

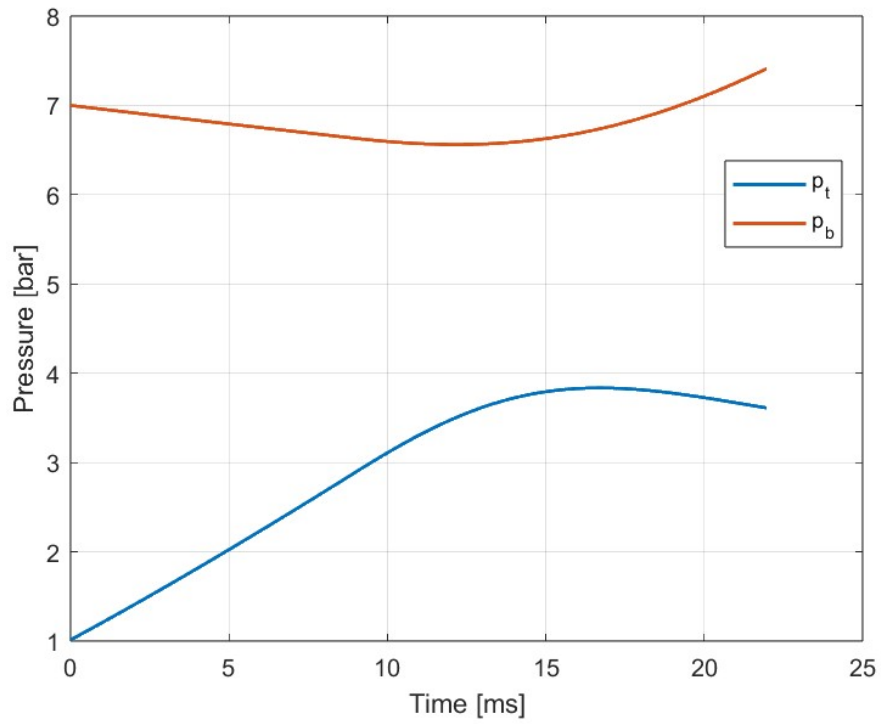


Figure 6.12: Pressure of air in the actuator's chambers in time.

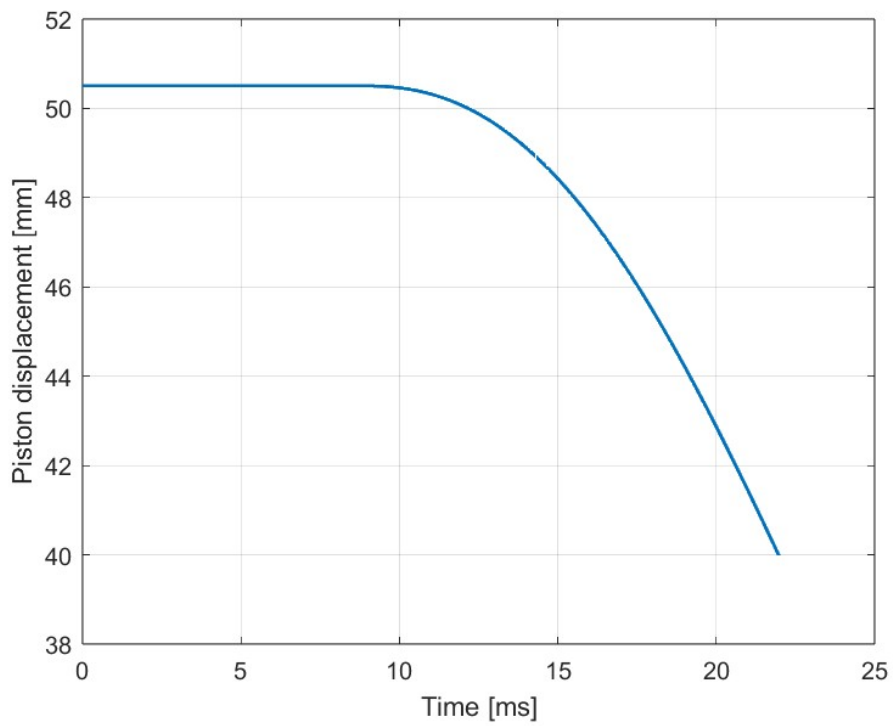


Figure 6.13: Brake's actuator displacement in time.

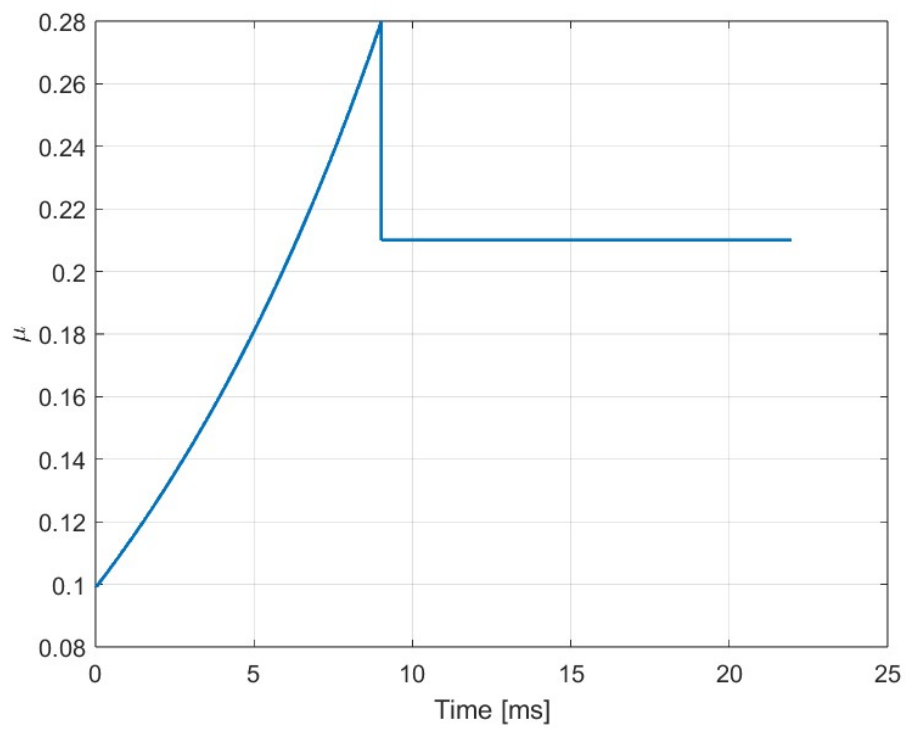


Figure 6.14: Coefficient of friction in time. It grows as the pushing force decreases, and once it reaches the maximum static level it lowers and settles at μ_{din} .

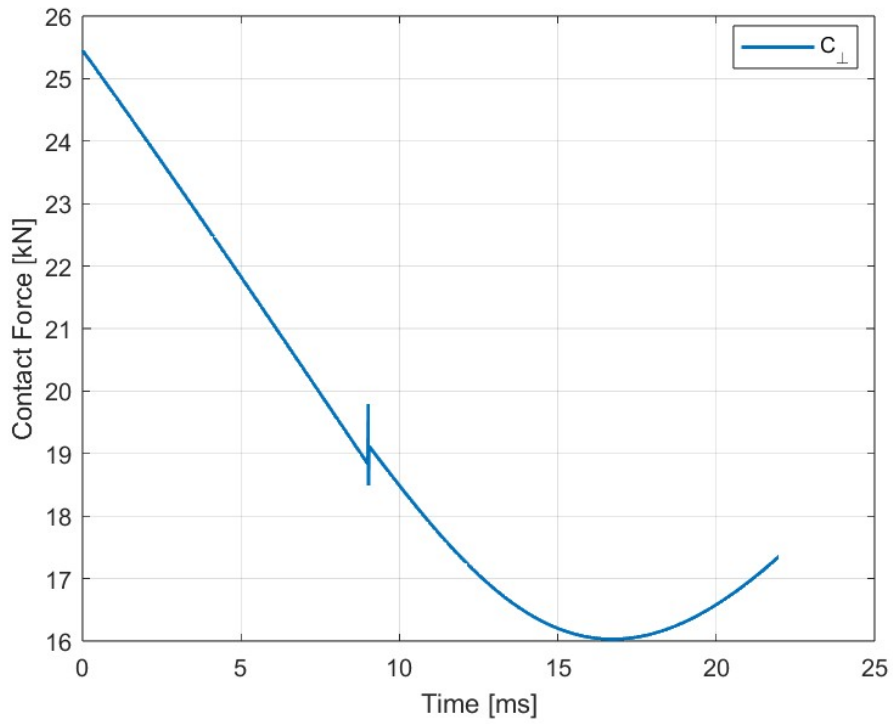


Figure 6.15: C_{\perp} in time.

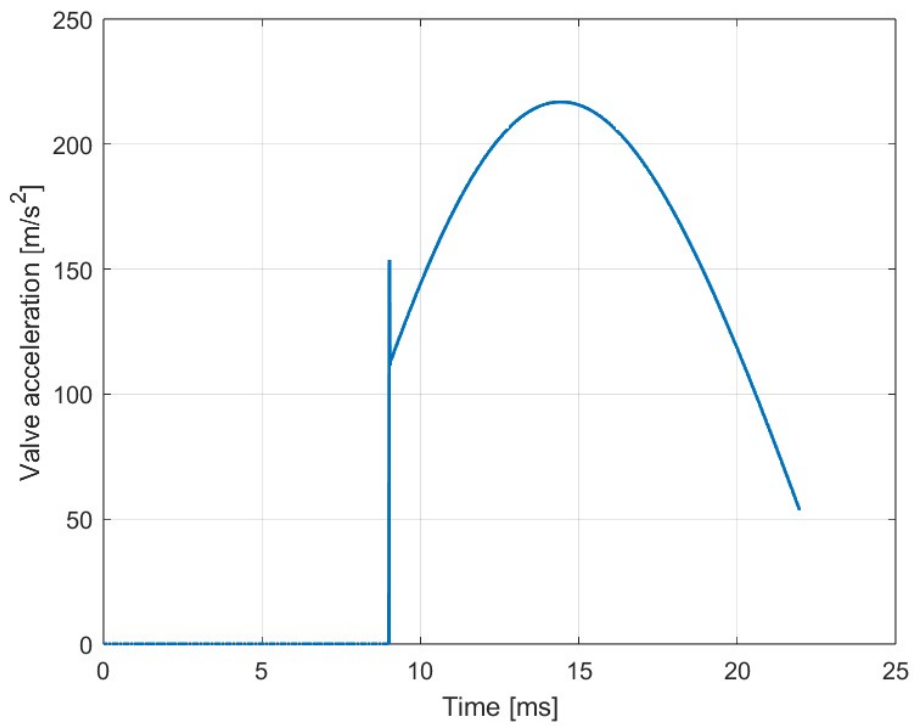


Figure 6.16: Valve's downward acceleration a_v .

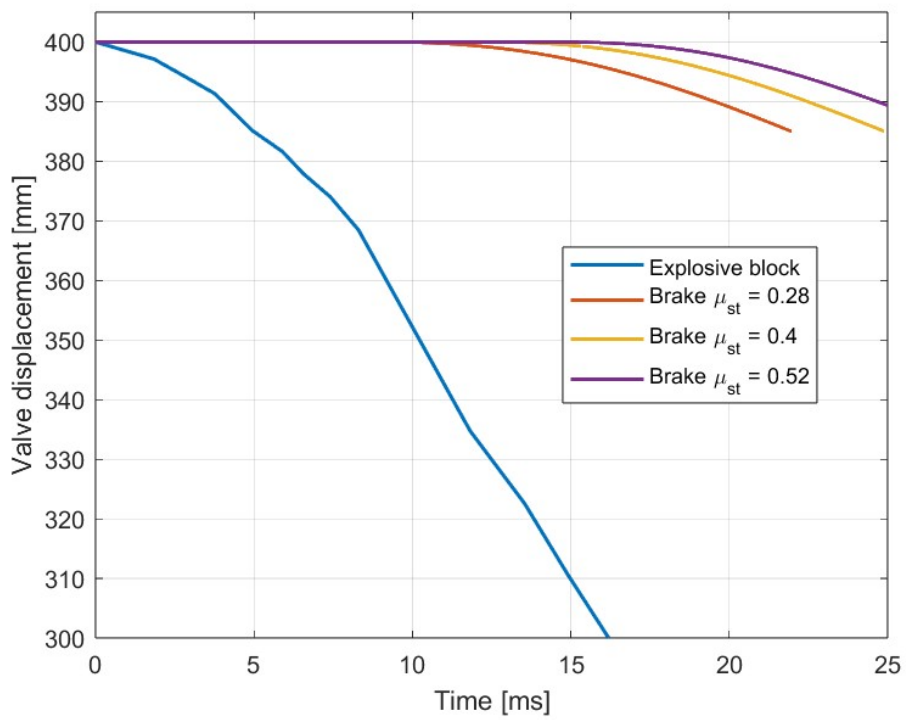


Figure 6.17: Comparison of the performance of the system in terms of valve's displacement, with the current setup.

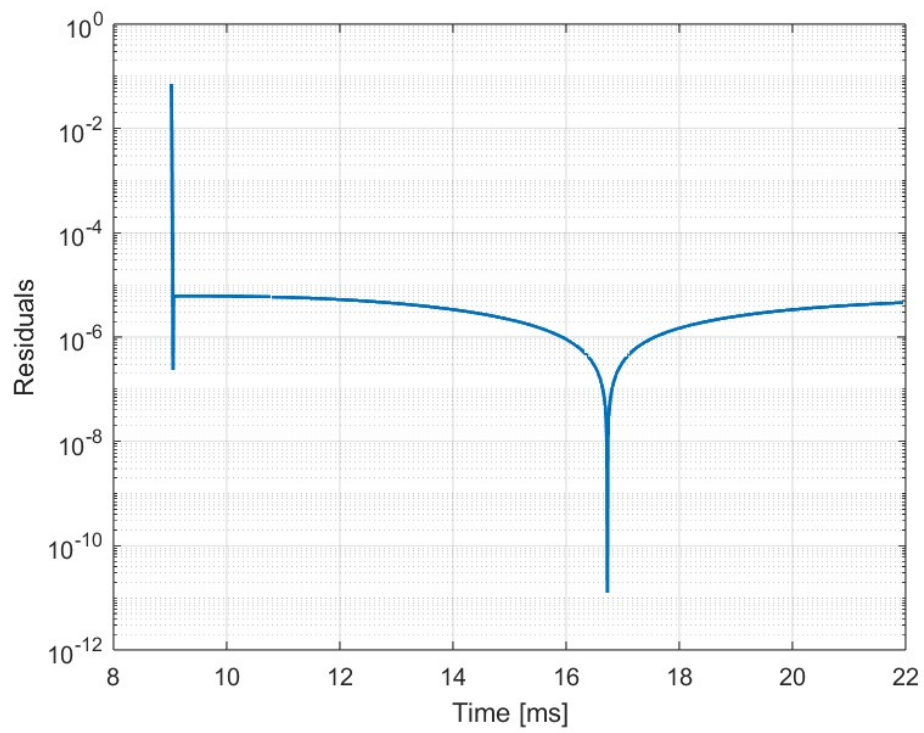


Figure 6.18: Residuals res_i in time.

From figures 6.16, 6.15 and 6.18 we can see that at the start of motion, a_v , C_{\perp} , and res_i spike and oscillate for a couple of iterations. This results from the transition between static and dynamic conditions, where $C_{\perp,i-1}$ computed under static conditions is applied to dynamic conditions. Figures from 6.9 to 6.13 illustrate the conditions inside the chambers of the actuator. Initially, while the actuator is static, the pressures in the chambers reverse, however, at $t \sim 13$ ms the trend shifts as the piston's movement compresses the venting chamber while expanding the other chamber. This means that also C_{\perp} , in figure 6.15, initially lowers, to then start growing again. This also affects the acceleration of the valve, in figure 6.16, which starts decreasing sharply as C_{\perp} stops lowering.

6.2.4 Negative outcome

The system proves to have substantial flaws, which do not seem to be solvable by selecting other actuator sizes. While a larger actuator would benefit from the lower α angle, which translates in slower brake motion that could prevent or delay the rise in C_{\perp} , it would also mean that the braking surface would get impractically large, as the ceramic braking compounds cannot support pressure values much higher than 3 MPa. Larger actuators would also suffer increased delays, as the 200, 250 and 320 mm actuators are all equipped with the same 3/4 in diameter connection to the pneumatic lines. While smaller actuators would have the advantage of reduced delays, they will certainly penalize the acceleration of the valve because of the higher α angles required to hold the system still before the opening.

6.3 Rocker Block

6.3.1 General description

Previously reviewed solutions showed that avoiding slip is a significant challenge because of the very high acceleration of the valve. This solution aims at making use of slip for helping with the removal of the locking body itself, giving the valve a progressively favorable leverage as the opening progresses. The locking body consists of a rocker, equipped with a sloped surface which supports the load of the valve. The angle of the sloped surface is such that if the rocker were not pulled by its actuator it would be moved aside by the valve's rod end. As shown in figure 6.19, in the closed configuration, a pneumatic actuator holds the rocker in its closed position, and the valve's load is transferred through the rocker to its supporting structure. At opening time the pressurization of the actuator switches and when the force it exerts

is no longer sufficient, the valve starts to move downward as it rotates the rocker counterclockwise and out of its way. The valve's rod end has a circular profile, so that the rocker can smoothly slide on it as the opening progresses. This also enables us to estimate the contact pressures and the resulting strain on the material using Hertz contact theory. The rocker's surface upon which the rod initially slides is flat, so to better spread the high contact forces. As the opening progresses and the contact force reduces, these can eventually be supported by the curved section of the contact surface.

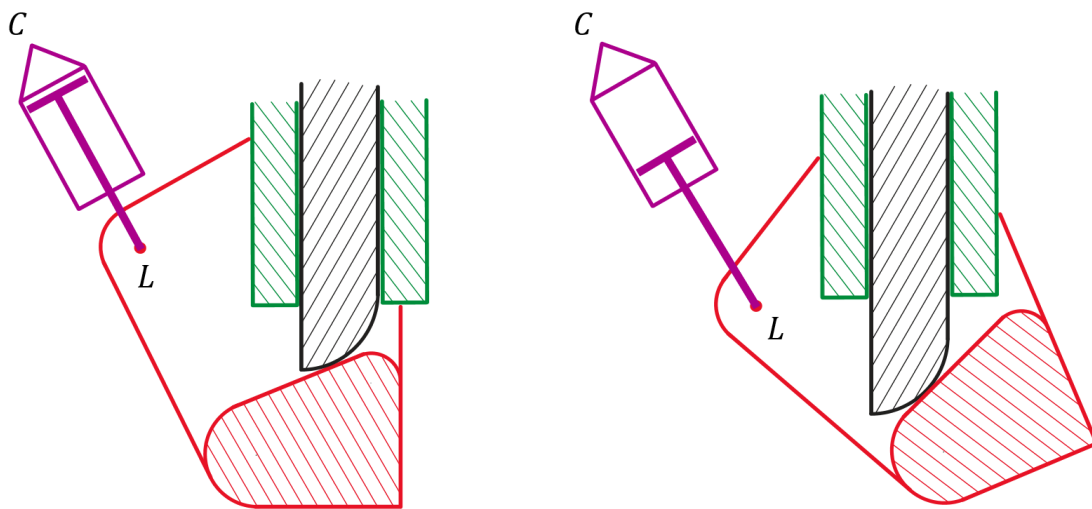


Figure 6.19: Simplified diagram of the rocker block, in closed configuration (on the left) and during opening (on the right). The sketch is not representative of proportions or any other quantitative factor, it should only be used for the general understanding of the concept.

6.3.2 Simplified modeling

The rocker rotates around its support O , is connected to its actuator in L and the contact forces due to the valve's rod end are applied in P . In the starting position, P is coincident to O' , vertically aligned with O on the sloped contact surface, so that most of the vertical load is supported by O rather than by the actuator. In this way the actuator can be smaller and thus react faster. The high forces at play require for the materials to be very strong and for this reason it is assumed the contact is steel on steel and greasy, to reduce drag forces during opening. The nominal static coefficient of friction is assumed to be 0.23 [15], but just like before, $\mu = \mu_{nom}(1 - S)$, where S this time is considered to be 0.5, because of the high variability of the friction coefficient due to smoothing of the contacting surfaces with use over time.

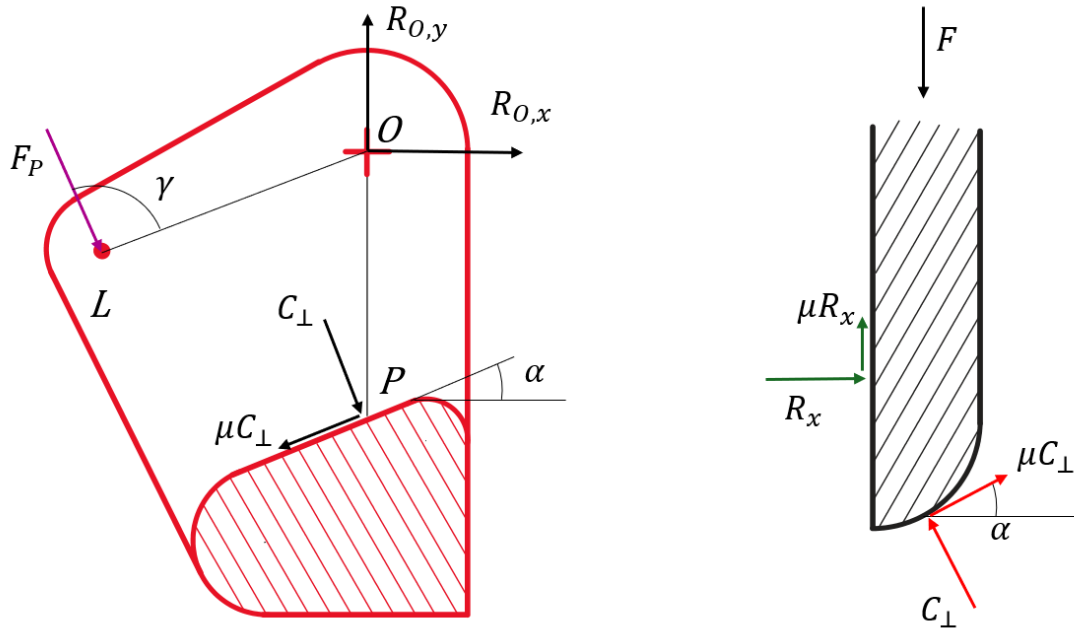


Figure 6.20: Free body diagram of the rocker and the valve's rod end in the static condition.

Looking at figure 6.20 we can write vertical and horizontal equilibrium equations for the rod and a rotation equilibrium equation around O , which result in:

$$C_{\perp} = \frac{F}{\cos \alpha (1 - \mu^2) + 2\mu \sin \alpha}; \quad (6.14)$$

$$F_p = -\frac{C_{\perp} r_{OP} (\sin \alpha - \mu \cos \alpha)}{r_{OL} \sin \gamma}. \quad (6.15)$$

The values F_p have then been transformed in actuator sizes with a safety factor of 1.5, and are reported in figure 6.21. Once again, [14] is used as a reference for available actuator sizes and geometry. Keeping in mind that with the same connecting port sizes, a larger actuator has higher compression effects due to movement of the piston and higher delay, and that a higher α increases the leverage that the rod end has to push the rocker away, the best compromise was found to be the 100 mm actuator, which is the smallest to have 1/2 in ports, which results in $\alpha = 16^\circ$.

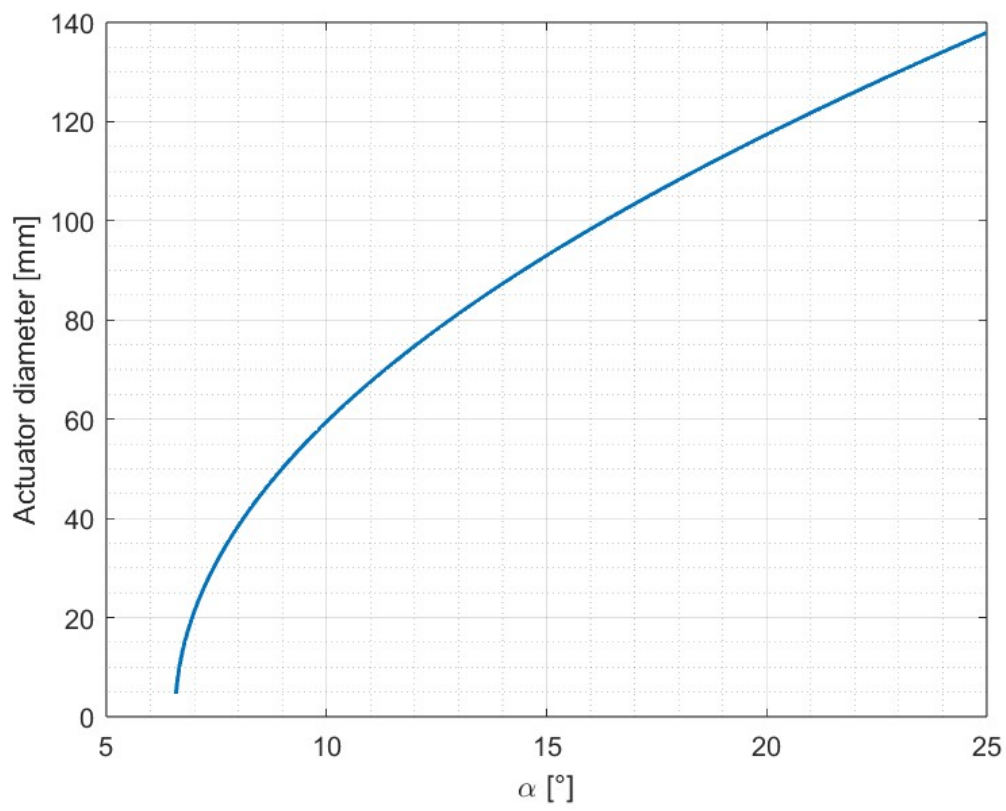


Figure 6.21: Required actuator diameter.

6.3.3 Detailed modeling

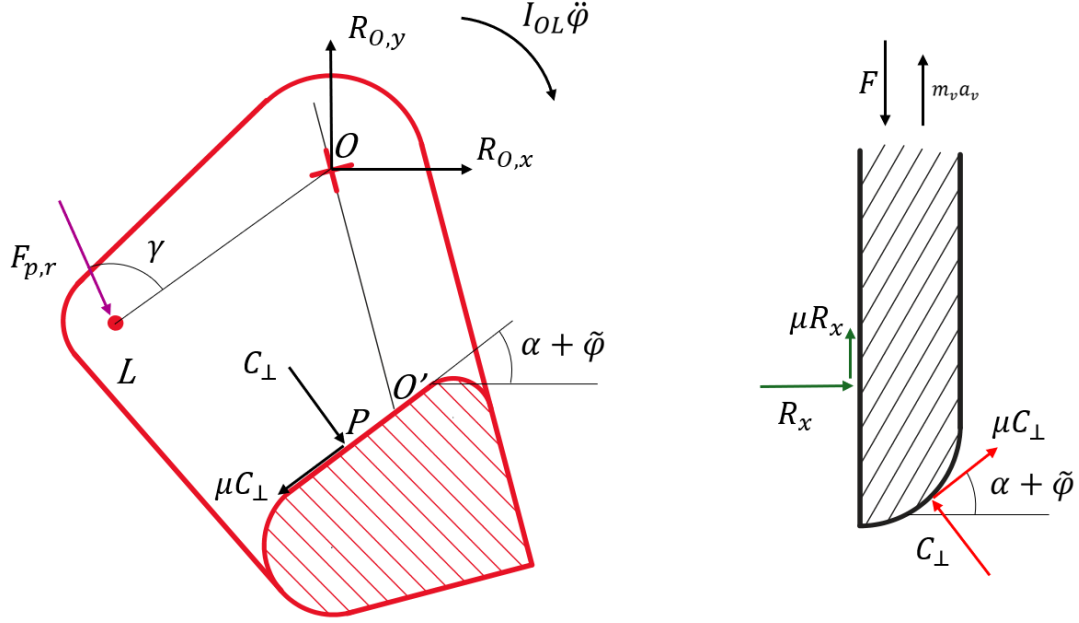


Figure 6.22: Free body diagram of the rocker and the valve's rod end in dynamic conditions.

Similarly to the brake solution, the model for a pneumatic actuator was integrated with equilibrium and kinetic equations to model the behavior and performance of the system. First we need to write an equilibrium equation for the whole system. The force from the piston is contributing to the rotation of the rocker around O , the rotation of the actuator around C and the linear movement of the moving parts of the actuator along \overline{CL} , as indicated in equation 6.16:

$$F_p = \frac{I_{OL}\ddot{\varphi} + C_{\perp}(\mu r_{OO'} \cos(\alpha + \tilde{\varphi}) - r_{OO'} \sin(\alpha + \tilde{\varphi}) - r_{O'P})}{r_{OL} \sin \gamma} + \frac{I_{CL}\ddot{\theta}}{r_{CL} \sin \gamma \cos \gamma} + m_p r_{\ddot{C}L}. \quad (6.16)$$

The first term of the sum in equation 6.16 is the contribution due to the angular acceleration $\ddot{\varphi}$ around O of the rocker, with moment of inertia I_{OL} , and to the contact forces that act on it. The second term is due to the actuator's angular acceleration $\ddot{\theta}$ around C , with inertia I_{CL} . The third term is due to the acceleration $r_{\ddot{C}L}$ of the moving parts of the actuator (piston and rod) with mass m_p . $\tilde{\varphi}$ is the rotation of the rocker relative to the starting position. Drag forces at the linkages C and L

have been neglected. I_{CL} has been assumed to be equal to the inertia of a beam weighting as much as the actuator about its end, and its value is updated at every timestep as r_{CL} increases. I_{OL} has been evaluated iteratively as the design of the rocker progressed.

Kinematic relations have been found to link velocities and accelerations together. Analyzing the velocity of L about C and O yields:

$$\dot{\varphi} = \frac{r_{\dot{C}L}}{r_{OL} \sin \gamma}, \quad (6.17)$$

$$\dot{\theta} = \frac{r_{\dot{C}L}}{r_{CL} \tan \gamma}. \quad (6.18)$$

Furthermore, evaluating the acceleration of L about C and O yields:

$$r_{\ddot{C}L} - r_{CL}\dot{\theta}^2 = -r_{OL}\dot{\varphi}^2 \cos \gamma + r_{OL}\ddot{\varphi} \sin \gamma, \quad (6.19)$$

$$r_{CL}\ddot{\theta} + 2r_{\dot{C}L}\dot{\theta} = r_{OL}\dot{\varphi}^2 \sin \gamma + r_{OL}\ddot{\varphi} \cos \gamma. \quad (6.20)$$

To find $r_{O'P}$, which appears in equation 6.16 we need to study the motion of P relative to the valve's rod end and to the rocker. Starting with the first one, looking at figure 6.23, let's consider a static reference frame Oxy centered above V , the center of the circular section of the rod end, with radius f . As the rocker rotates by an angle $\tilde{\varphi}$, with angular velocity and acceleration $\dot{\varphi}$ and $\ddot{\varphi}$, the sloped flat surface rotates by an equal amount and at the same rates. Being P the contact point between the two, it will always find itself on the circumference described by f around V and on the sloped surface of the rocker, and thus at the tangent point between the two. V is constrained to move up and down, with velocity and acceleration v_V and a_V , considered positive in the direction $-y$. For improving readability, we will now consider $\delta = \alpha + \tilde{\varphi}$.

The velocity of P along x and y can be written as:

$$v_{Px} = f\dot{\varphi} \cos \delta, \quad (6.21)$$

$$v_{Py} = -v_V + f\dot{\varphi} \sin \delta, \quad (6.22)$$

and the accelerations:

$$a_{Px} = \ddot{\varphi}f \cos \delta - \dot{\varphi}^2 \sin \delta, \quad (6.23)$$

$$a_{Py} = -a_V + \ddot{\varphi}f \sin \delta + \dot{\varphi}^2 f \cos \delta. \quad (6.24)$$

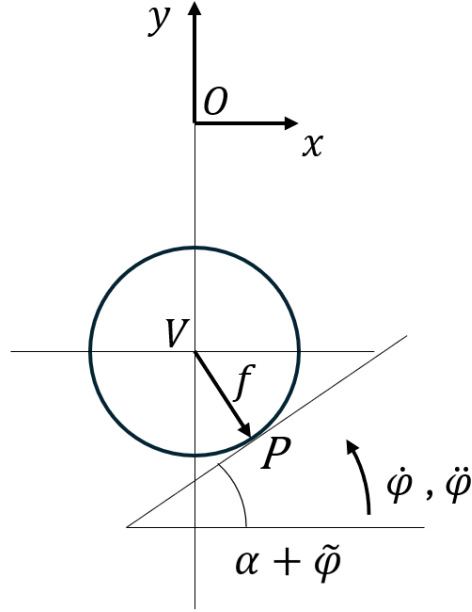


Figure 6.23: Sketch for evaluating the position of P in the reference frame of the valve's rod end.

For the rocker, looking at figure 6.24, let's consider a static reference frame Oxy centered in the center of rotation of the rocker. Using relative motion, we can write the following equations:

$$v_{Px} = r_{OO'}\dot{\varphi} \cos \tilde{\varphi} - r_{O'P}\dot{\varphi} \sin \delta + \dot{r}_{O'P} \cos \delta \quad (6.25)$$

$$v_{Py} = r_{OO'}\dot{\varphi} \sin \tilde{\varphi} + r_{O'P}\dot{\varphi} \cos \delta + \dot{r}_{O'P} \sin \delta \quad (6.26)$$

$$a_{Px} = a_{O'x} - \ddot{\varphi}r_{O'P} \sin \delta - \dot{\varphi}^2 r_{O'P} \cos \delta - 2\dot{\varphi}\dot{r}_{O'P} \sin \delta + r_{O'P}\ddot{\delta} \cos \delta \quad (6.27)$$

$$a_{Py} = a_{O'y} + \ddot{\varphi}r_{O'P} \cos \delta - \dot{\varphi}^2 r_{O'P} \sin \delta + 2\dot{\varphi}\dot{r}_{O'P} \cos \delta + r_{O'P}\ddot{\delta} \sin \delta \quad (6.28)$$

where

$$a_{O'x} = r_{OO'}\ddot{\varphi} \cos \tilde{\varphi} - r_{OO'}\dot{\varphi}^2 \sin \tilde{\varphi} \quad (6.29)$$

$$a_{O'y} = r_{OO'}\ddot{\varphi} \sin \tilde{\varphi} + r_{OO'}\dot{\varphi}^2 \cos \tilde{\varphi}. \quad (6.30)$$

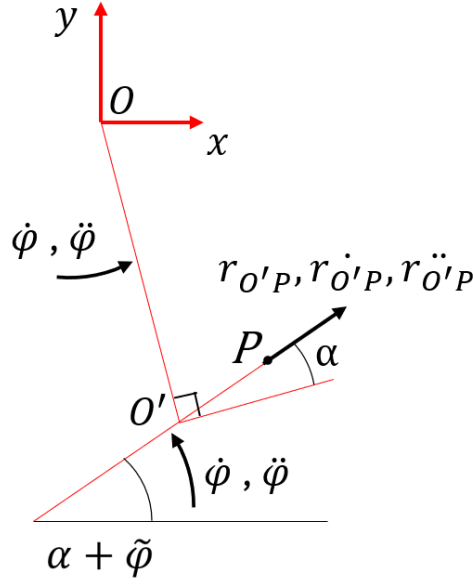


Figure 6.24: Sketch for evaluating the position of P in the reference frame of the rocker.

$r_{O'P}$, $r_{O'P}$ and $r_{O'P}$ are the distance, velocity and acceleration of P along the rotating sloped surface relative to O' , positive as shown in the figure. Because the velocities and accelerations are found in reference systems that are both static and with the same orientation, even though not coincident, accelerations and velocities in one reference are equal in the other.

6.3.4 Implementation

As before, for every time-step, the F_p exerted by the actuator is known. Rearranging 6.16 and using 6.19 and 6.20 to find $\ddot{\theta}$ and $\ddot{\varphi}$, we can use information from the previous time-step to compute the acceleration of the extension of the actuator with

$$\begin{aligned}
 r_{\ddot{C}L} = & \frac{F_p - \frac{C_{\perp}(\mu r_{OO'} \cos(\alpha + \tilde{\varphi}) - r_{OO'} \sin(\alpha + \tilde{\varphi}) + r_{O'P})}{r_{OO'} \sin \gamma}}{m_p + \frac{I_{LC}}{(r \sin \gamma)^2} + \frac{I_{OL}}{(r_{OO'} \sin \gamma)^2}} \\
 & - \frac{\frac{I_{LC}}{r \sin \gamma \cos \gamma} \left(\frac{r_{OO'} \dot{\varphi}^2 \sin \gamma}{r} + \frac{r_{OO'}}{r} (-r \dot{\theta}^2 + r_{OO'} \dot{\varphi}^2 \cos \gamma) \right) \frac{\cos \gamma}{r_{OO'} \sin \gamma} - 2 \frac{r_{\dot{C}L} \dot{\theta}}{r}}{m_p + \frac{I_{LC}}{(r \sin \gamma)^2} + \frac{I_{OL}}{(r_{OO'} \sin \gamma)^2}} \\
 & - \frac{\frac{I_{OL}}{(r_{OO'} \sin \gamma)^2} (-r \dot{\theta}^2 + r_{OO'} \dot{\varphi}^2 \cos \gamma)}{m_p + \frac{I_{LC}}{(r \sin \gamma)^2} + \frac{I_{OL}}{(r_{OO'} \sin \gamma)^2}}, \tag{6.31}
 \end{aligned}$$

\dot{r}_{CL} and r_{CL} can be obtained integrating it in the duration of the time-step. The new value for γ can be computed:

$$\gamma = \arccos\left(\frac{r_{CL}^2 + r_{OL}^2 - r_{OC}^2}{2r_{CL}r_{OL}}\right) \quad (6.32)$$

and from 6.19 and 6.20 we can compute

$$\ddot{\varphi} = \frac{\ddot{r}_{CL}}{r_{OL} \sin(\gamma)} - \frac{\dot{r}_{CL}^2}{r_{CL}r_{OL} \tan^2(\gamma) \sin(\gamma)} + \frac{\dot{r}_{CL}^2}{r_{OL}^2 \tan(\gamma) \sin^2(\gamma)}, \quad (6.33)$$

$$\ddot{\theta} = \frac{r_{OL}\dot{\varphi}^2 \sin(\gamma) + r_{OL}\ddot{\varphi} \cos(\gamma) - 2\dot{r}_{CL}\dot{\theta}}{r_{CL}}, \quad (6.34)$$

and with 6.17 and 6.18 can be used to update to find angular velocities. Finally θ and φ can be integrated from the respective angular velocities and accelerations.

Since θ and φ are computed with respect to a common direction, we can also express

$$\gamma_c = \theta - \varphi \quad (6.35)$$

and compute residuals to measure the accuracy of the computation:

$$\text{res}_\gamma = \left| \frac{\gamma - \gamma_c}{\gamma} \right|. \quad (6.36)$$

Using 6.29 and 6.29, we can equate equations 6.21 and 6.25, 6.22 and 6.26, 6.23 and 6.27, 6.24 and 6.28 to find:

$$\dot{r}_{O'P} = \frac{f\dot{\varphi} \cos(\delta) + r_{O'P}\dot{\varphi} \sin(\delta) - r_{O'O'}\dot{\varphi} \cos(\tilde{\varphi})}{\cos(\delta)}, \quad (6.37)$$

$$v_v = f\dot{\varphi} \sin(\delta) - r_{O'O'}\dot{\varphi} \sin(\tilde{\varphi}) - r_{O'P}\dot{\varphi} \cos(\delta) - \dot{r}_{O'P} \sin(\delta), \quad (6.38)$$

$$\ddot{r}_{O'P} = \frac{\ddot{\varphi}f \cos(\delta) - \dot{\varphi}f \sin(\delta) - a_{O'x} + \ddot{\varphi}r_{O'P} \sin(\delta) + \dot{\varphi}^2 r_{O'P} \cos(\delta) + 2\dot{\varphi}\dot{r}_{O'P} \sin(\delta)}{\cos(\delta)}, \quad (6.39)$$

$$a_v = \ddot{\varphi}f \sin(\delta) + \dot{\varphi}^2 f \cos(\delta) - a_{O'y} - \ddot{\varphi}r_{O'P} \cos(\delta) + \dot{\varphi}^2 r_{O'P} \sin(\delta) - 2\dot{\varphi}\dot{r}_{O'P} \cos(\delta) - \ddot{r}_{O'P} \sin(\delta). \quad (6.40)$$

At this point $r_{O'P}$ and the position of the valve can be integrated, and using the vertical and horizontal equilibrium equation for the rod we finally find:

$$C_{\perp} = \frac{F - \beta v_v - m_v a_v}{\cos(\alpha + \tilde{\varphi})(1 - \mu^2) + 2\mu \sin(\alpha + \tilde{\varphi})}, \quad (6.41)$$

$$R_x = C_{\perp}(\sin(\alpha + \tilde{\varphi}) - \mu \cos(\alpha + \tilde{\varphi})). \quad (6.42)$$

Additional residuals are computed for the position of the contact point P and for the vertical equilibrium of the rod. The simulation ends once P reaches the end of the flat surface of the rocker.

6.3.5 Dimensions of the valve's rod end

As anticipated before, Hertz's contact theory has been used to determine the value of f . A cylindrical contact was excluded from possible solutions, as the load from the rod would cause deformation of the rocker's flat contact surface in the center, and thus most of the load would be supported at the extremities of the cylinder, further amplifying edge effects. The alternative consists in "crowning" the contact surface: this means introducing a curvature to the valve's rod end out of the plane of the cross-section of figure 6.19. The effect of tangential forces due to friction was neglected. The analysis led to a crowning radius of 3000 mm and f of 35 mm, which, with a load of 18580 N from the valve's actuator, results in a maximum equivalent tension of 647 MPa under the center of the contact surfaces. The contact patch results to be an ellipse with semi-axes of 12.1 mm and 0.66 mm. Choosing a steel alloy with high yield of at least 900 MPa, such as quenched and tempered 42CrMo4, gives sufficient safety margin to the design, as these kind of parts are expected to perform adequately even after suffering small plastic deformation.

The parts are also expected to perform a relatively low number of cycles, 36500 as per the requirements. A first order fatigue analysis can be conducted using the classical fatigue model, where the load cycle can be considered to start with the rocker at rest, then being loaded by the valve's load and then the load being removed, returning to initial conditions. In this case, the minimum value of equivalent tension is $\sigma_{min} = 0$ MPa when the rocker is at rest, while the maximum value is $\sigma_{max} = 647$ MPa. The load cycle is characterized by $R = \frac{\sigma_{min}}{\sigma_{max}} = 0$ and using the properties from [16] for 42CrMo4, we obtain the results reported in 6.26 and 6.25. Our load case, with alternating stress of 323 MPa sits below the fatigue limit for the chosen steel alloy.

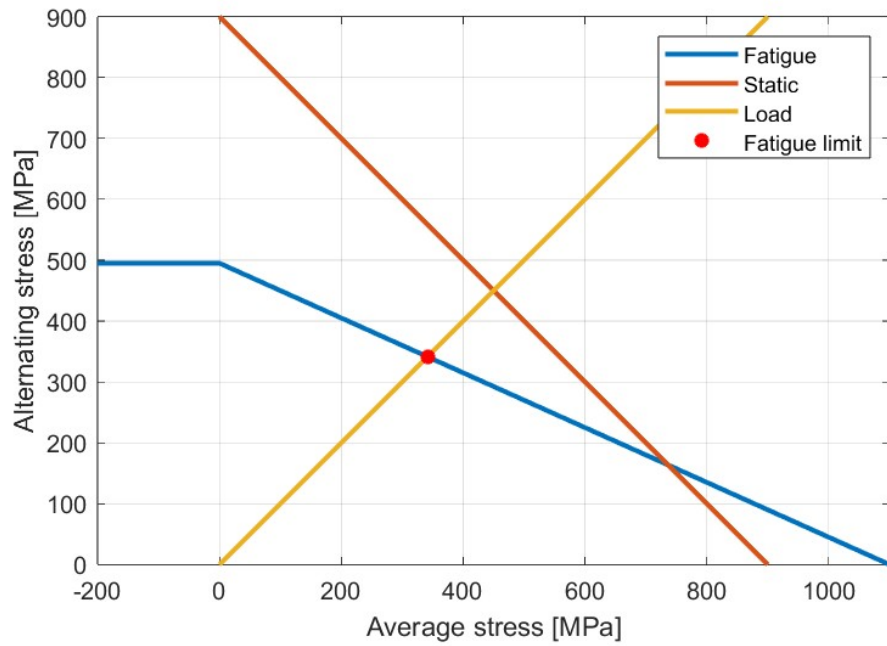


Figure 6.25: Haigh diagram for 42CrMo4 steel.

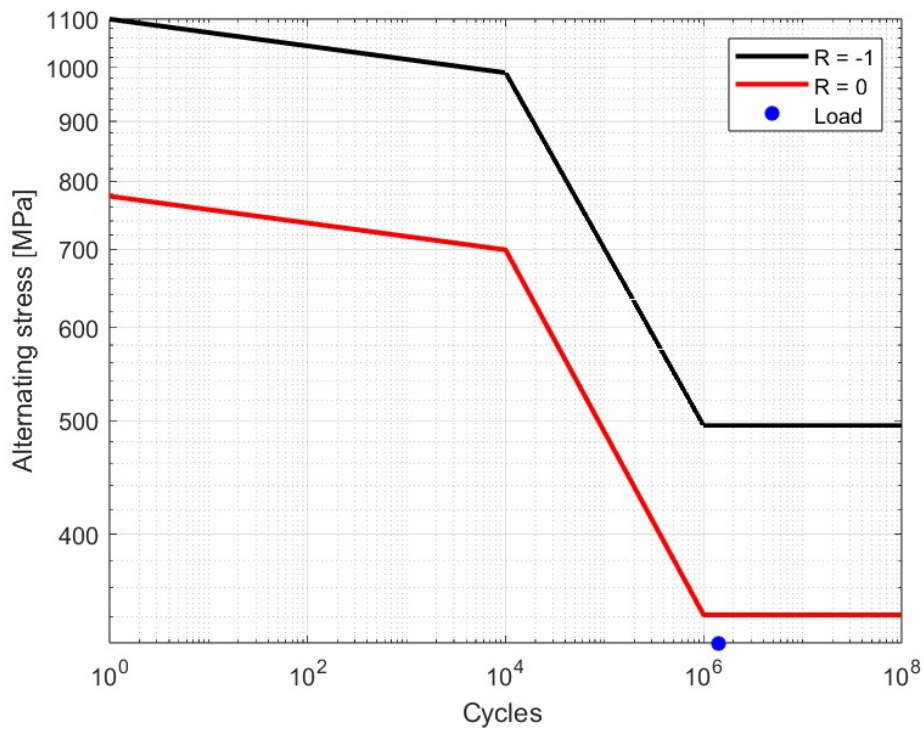


Figure 6.26: Wöhler curve for 42CrMo4 steel.

6.3.6 Results for CT3 scale model

For the rocker at this scale, the values chosen for some of the parameters that have yet to be discussed are reported in table 6.1.

Parameter	Value	Comment
r_{OL}	70 mm	The lower, the lighter the rocker, but the size of the main valve's actuator (positioned above the rocker, as close as possible to it) requires a value close to 100 mm for ensuring fitment of the system.
r_{CL}	150 mm	Conservative estimate for fitting the actuator.
$r_{OO'}$	70 mm	A value lower than r_{OL} increases the leverage of the actuator, but requires it to move faster to achieve the same $\ddot{\varphi}$ value, which is what ultimately enables a fast opening. A higher value than r_{OL} decreases the leverage of the actuator, increasing the size required and thus its reaction time.
μ_{st}	0.12-0.28	[15] reports 0.23 as the static coefficient of friction for hard steel on hard steel with light mineral oil as lubricant, and advises to use values in a range of $\pm 20\%$. The range here considered is from -50% to $+20\%$.
μ_{din}	0.08-0.2	[17] reports the range for multiple material combinations
SF	1.5	Safety factor for masses, giving margin for additional parts currently unaccounted for (e.g. bearings, link in L).
I_{OL}	$0.00875 * SF$ kg m ²	Found after developing the geometry.
m_{act}	$4.3 * SF$ kg	Mass of the actuator, from [14].
m_p	$1.3 * SF$ kg	Mass of moving parts of the actuator, from [14].

Table 6.1: Table with unaddressed parameters for the CT3 scale rocker.

Here the results for the performance of the rocker locking system are reported. Unless explicitly labeled, the results shown are for the lower values of static and dynamic friction coefficients within the considered ranges. This is the scenario where the actuator is contrasting the rotation of the rocker the most, because friction forces are breached earlier. As a result, C_{\perp} and R_x are the highest and the valve moves with the lowest delay. The simulation is stopped when the contact point between the valve's rod end and the rocker reaches the end of the flat surface of the rocker,

which is considered to be $r_{O'P,end} = -21$ mm.

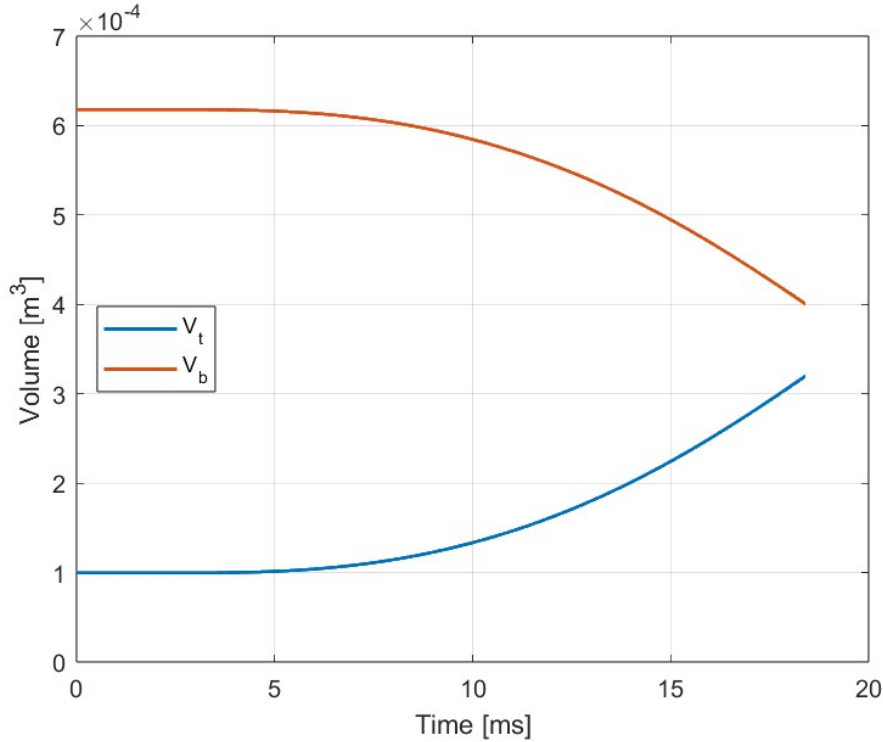


Figure 6.27: Actuator's chamber volumes in time.

Looking at figure 6.38 the performance of the rocker in terms of delay and worsening of the opening time does not seem significantly better than the one of the brake. Looking further in the results though, it seems like a valid solution. One of the reasons for this is the low difference between the opening times for the low and high friction scenarios. In the real world this translates in high repeatability of the opening, especially after an initial break-in period, where contact surfaces are smoothed down by repeated usage. Other promising results are the steady increase of the valve's acceleration (figure 6.37), and the decrease in C_{\perp} (figure 6.35) during the run. This last fact allows to further explore the design of the rocker's contacting geometry. In particular, a curved surface, as depicted in 6.19, could be placed after the flat surface, further enhancing the valve's acceleration trend shown in the results. This is true because as the rocker rotates, a curved surface will provide an increased slope for the contact point to find itself on, compared to a straight plane. The contact point along the curved surface will also be further from O , increasing the leverage of the rod end to move the rocker away. These two effects lower C_{\perp} overall, but also lower its vertical component, affecting the acceleration of the valve. To find an appropriate f_r radius of this surface we can extract the highest load that

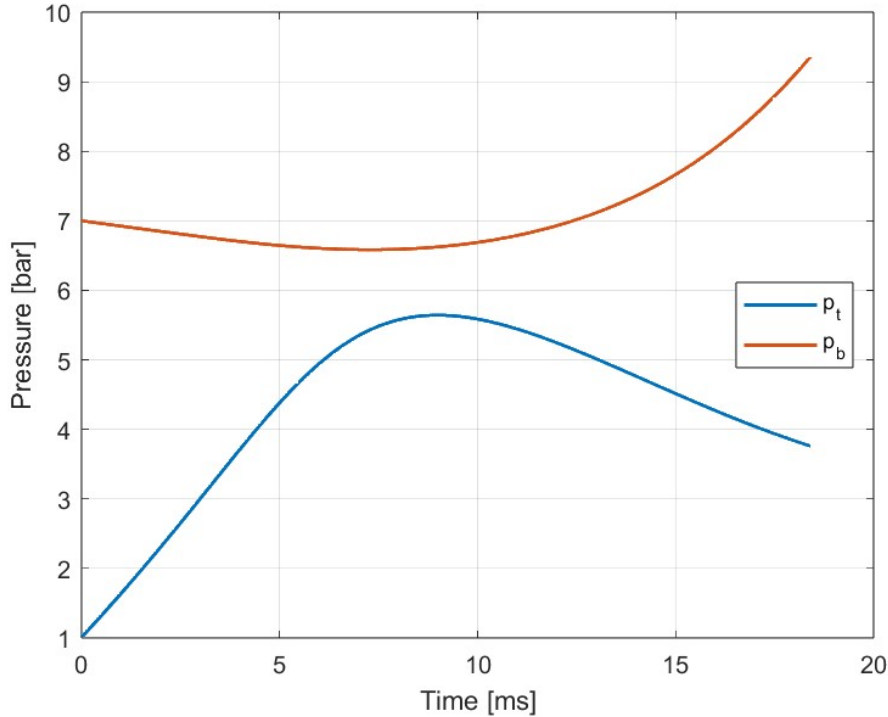


Figure 6.28: Actuator's chamber pressures in time.

it is going to support from figure 6.35: at the end of the simulation (when the contact point moves on the curved surface) C_{\perp} is 9000 N. With the same assumptions that were made for finding f , we can determine that if $f_r = 35$ mm, the contact will generate a 695 MPa maximum stress below the center of the contact patch, an ellipse with semi-axes of 10 mm and 0.37 mm. The stress is compatible with the material choice and the tolerance of small plastic deformation of the structure. The main dimensions of the system thus far determined are displayed in figure 6.39.

Figures 6.27, 6.28, 6.29, 6.30 and 6.31 show the behavior of the actuator: initially the actuator does not move, the top chamber pressurizes and heats up while the bottom one vents and cools slightly. At about ~ 3 ms the assembly starts moving, and as the speed of the piston increases, the variation in volume of the chamber reverts the trends of the pressure curves.

Figures 6.32, 6.33 and 6.34 show how the assembly changes: because γ starts at 90° , the initial increase in r_{CL} only causes φ to change, while θ changes at lower rates and later in the opening. Figure 6.36 shows the accuracy of the calculation: at the end of the simulation, the position of P has a discrepancy of 0.01 mm between the rod end and the rocker, while γ has a discrepancy of 0.0034° .

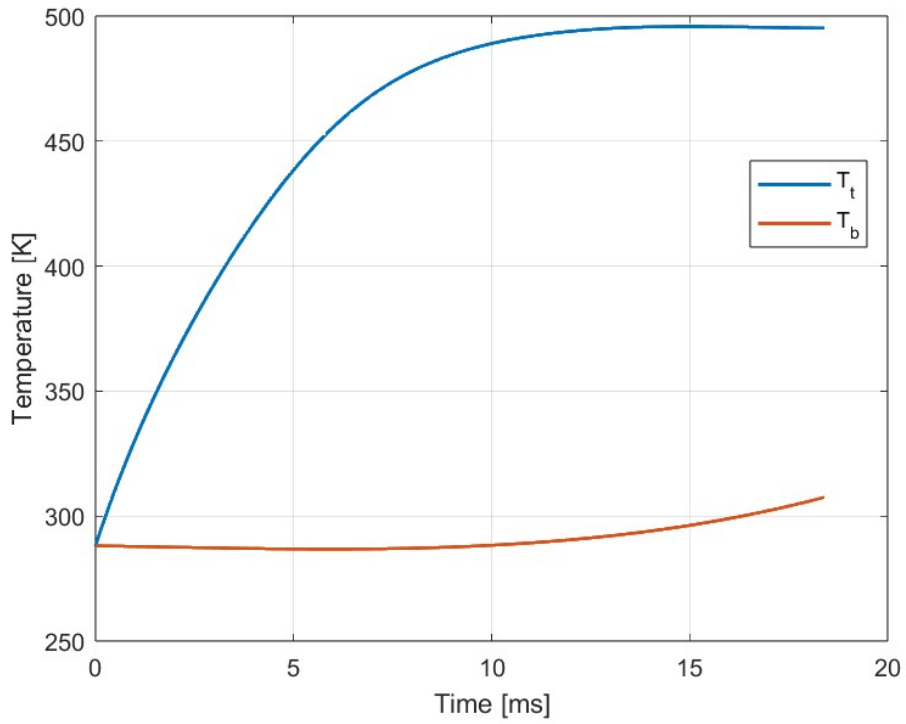


Figure 6.29: Actuator's chamber temperatures in time.

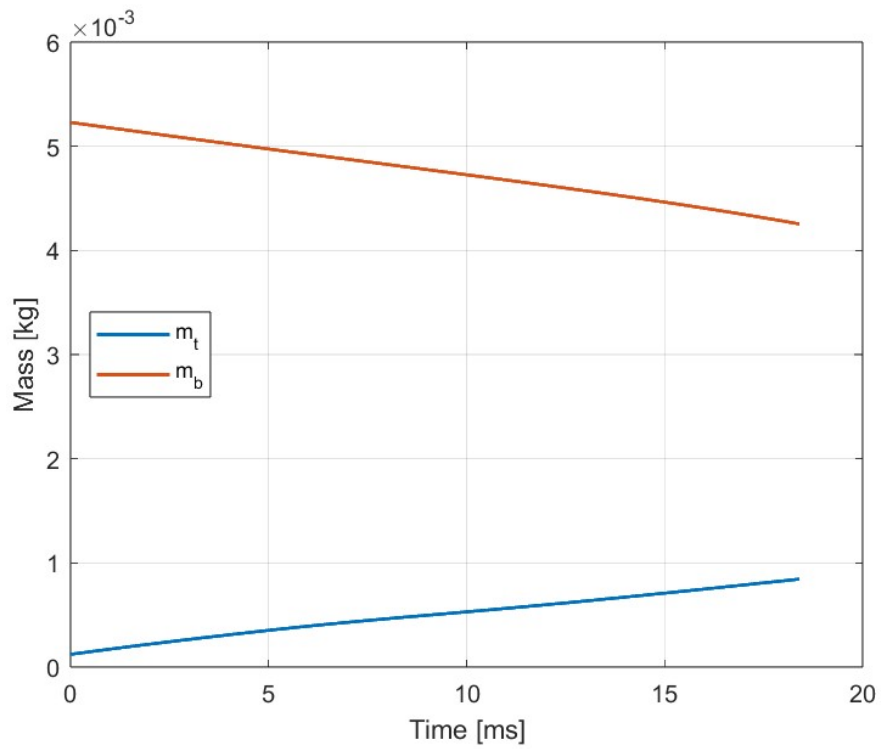


Figure 6.30: Mass of air in the actuator's chambers.

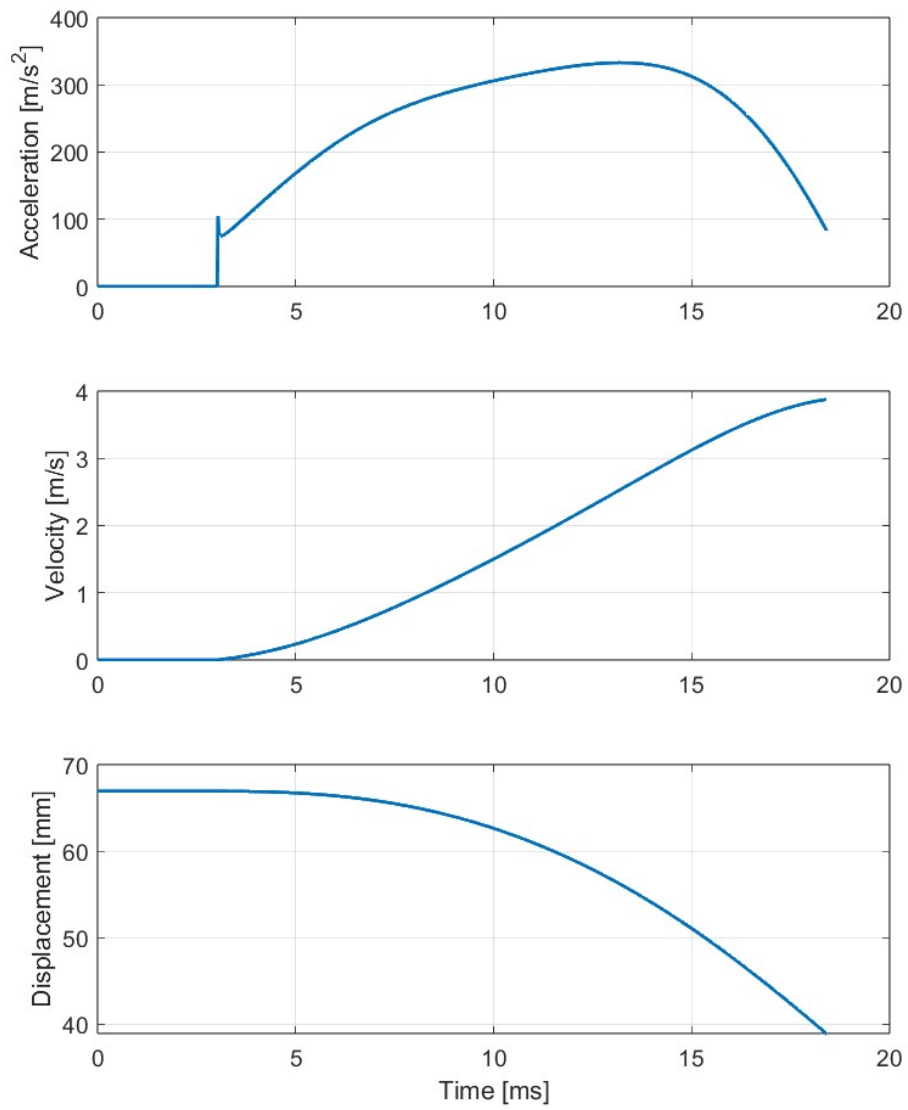


Figure 6.31: Acceleration, velocity and position of the rocker's actuator.

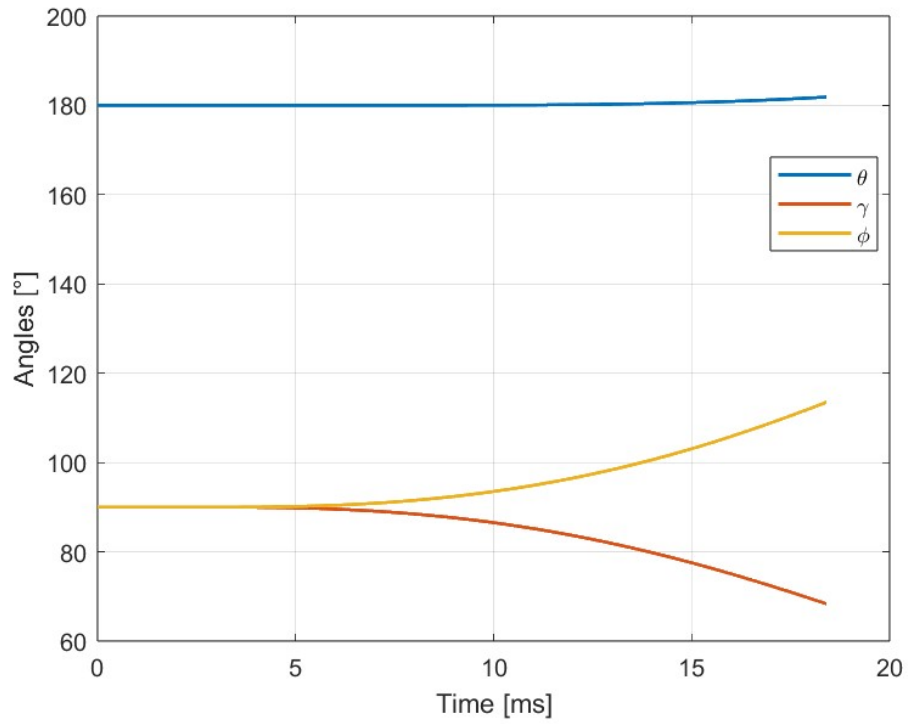


Figure 6.32: Angles' evolution in time.

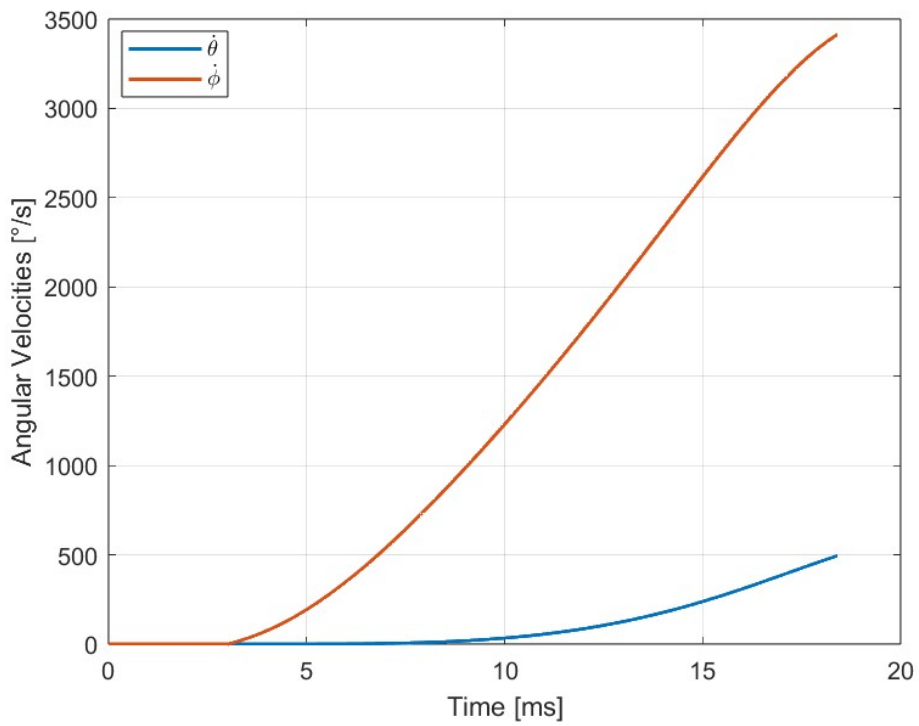


Figure 6.33: Angular velocities.

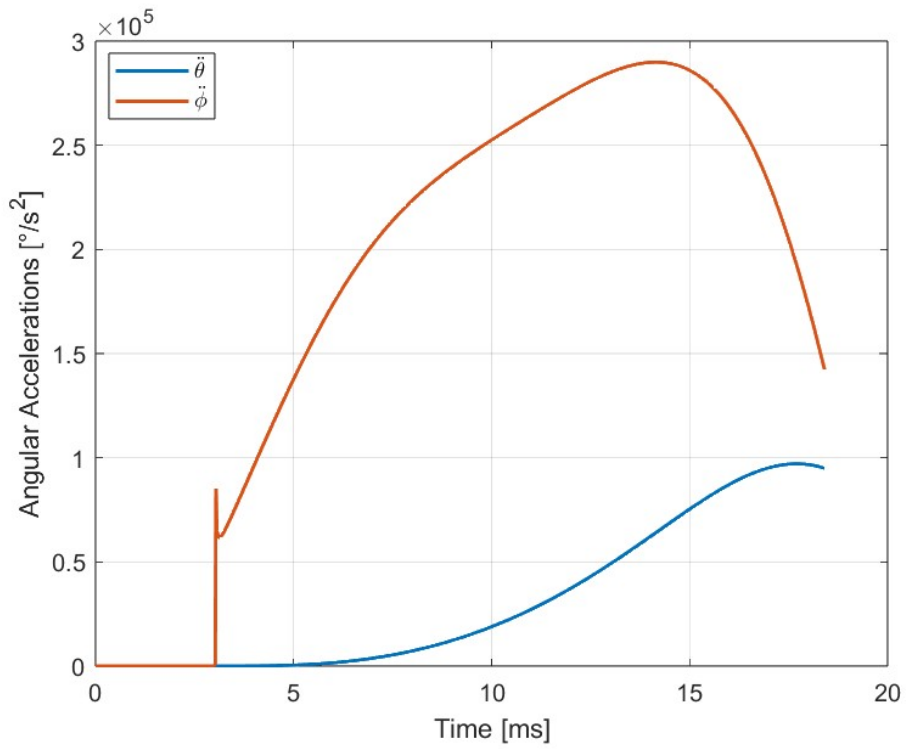


Figure 6.34: Angular accelerations.

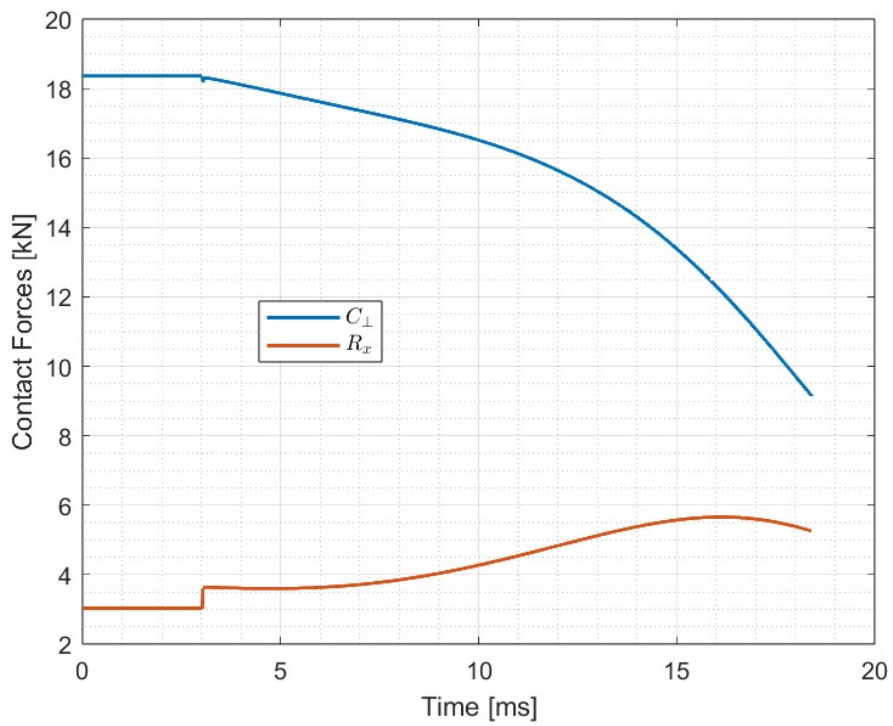


Figure 6.35: Contact forces.

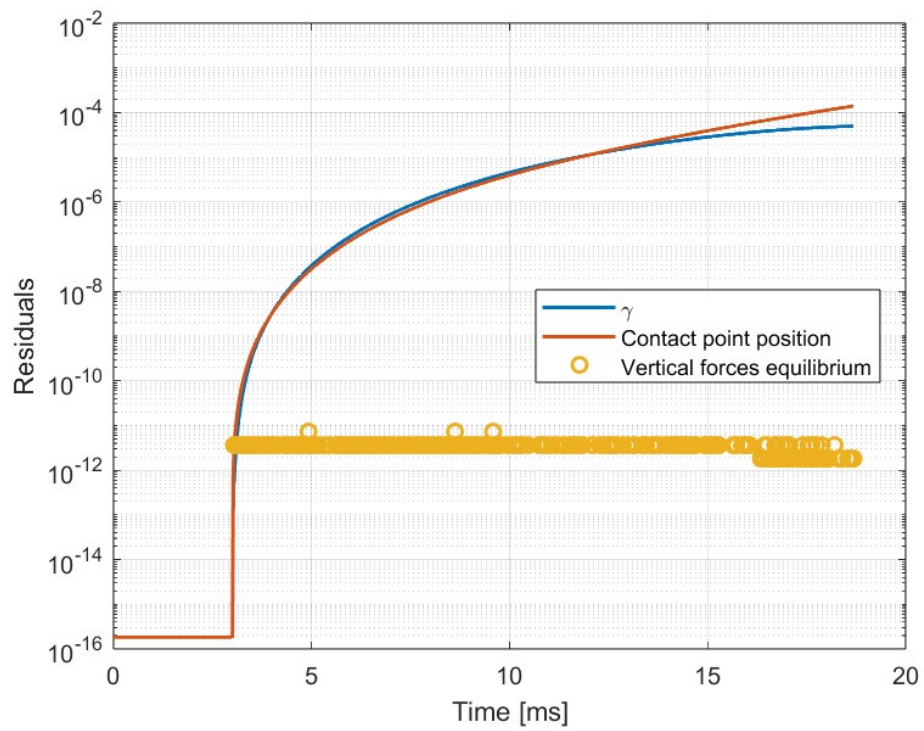


Figure 6.36: Residuals for γ , the position of P and for the vertical equilibrium of the valve.

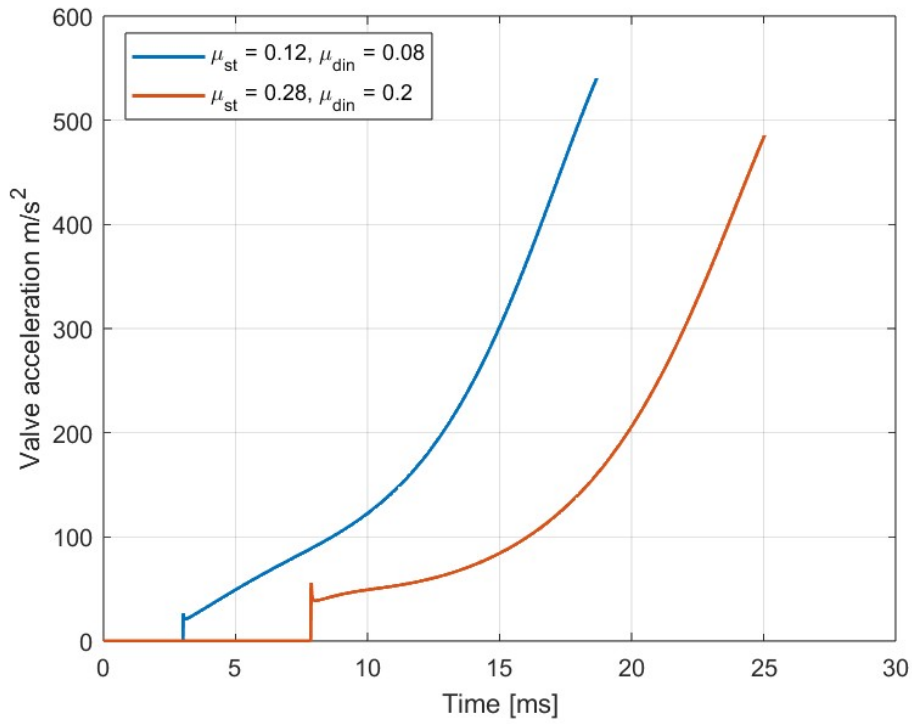


Figure 6.37: Valve acceleration.

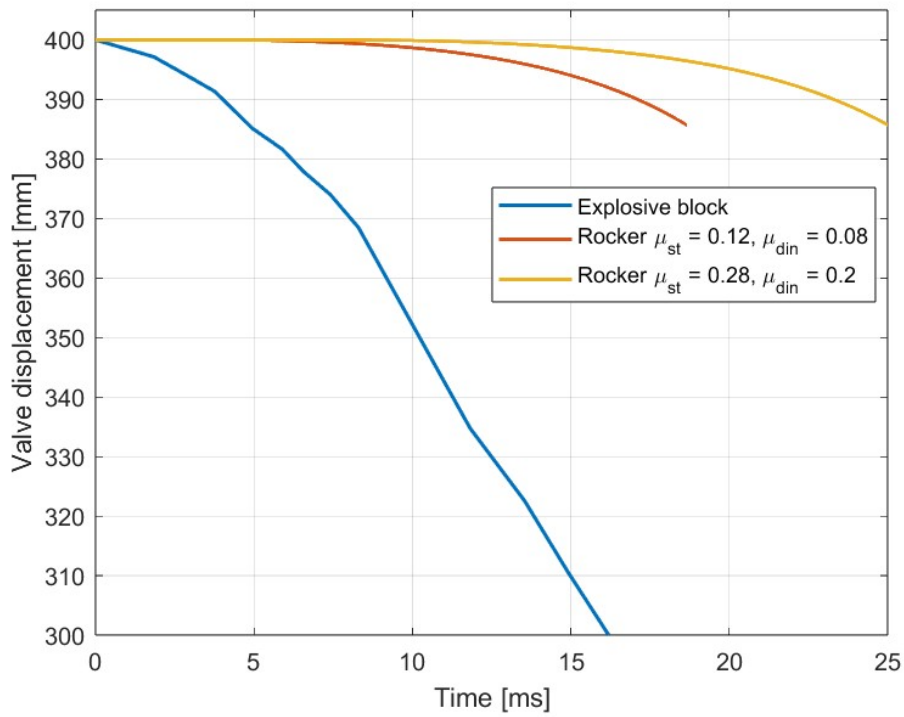


Figure 6.38: Valve displacement comparison.

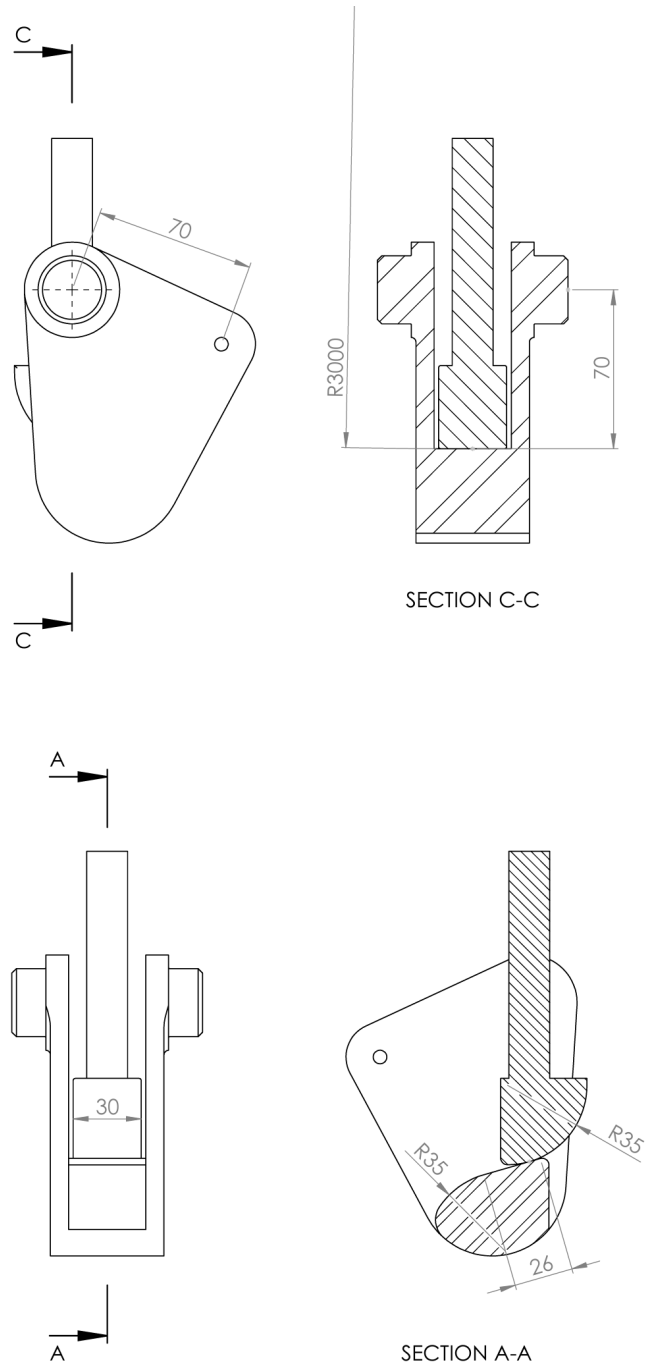


Figure 6.39: Lateral and frontal views of the rocker and rod end assembled in the closed configuration.

6.3.7 Scaling for Prototype

The purpose of producing a scaled-down prototype of the system is to verify the basic working principle of the mechanism and to highlight any unforeseen shortcomings of the solution. In this case in particular, it will also work to validate the numerical results and to provide further insight on the most critical aspects of the project. Such is the case for friction coefficients and the possible plastic deformation of the contact surface. To do this, the materials and the maximum equivalent tension should be preserved, and for this, the trend of the forces on the contact surfaces should also be preserved. All this has to be done at a smaller scale, so to lower the costs of the prototype. The chosen scale for the prototype is 1:4, so an actuator with diameter of 50 mm and 100 mm stroke will act as the valve, with the addition of some ballast weight to achieve the same maximum acceleration of the actual valve. From the analysis of the static equilibrium of the rocker, a linear dependence emerged between F and F_p , so we can assume that applying the same scale factor to the size of the rocker's actuator will allow us to preserve $\alpha = 16^\circ$, and thus the actuator for the rocker will be 25 mm in diameter. Because the rocker would now be rather small, about 2 cm x 2 cm, a decision was made to sacrifice some accuracy in the replication of C_\perp in exchange for a slightly larger part, which makes it easier to handle. For this reason, f , f_r , $r_{OO'}$, r_{OL} , r_{CL} , were up-scaled by a factor of 1.5 after the initial 1:4 scaling. For this reason and for preserving contact pressures, the crowning radius of the valve's rod end had to be significantly reduced to 370 mm to achieve maximum equivalent tensions within 2% of the ones obtained for the full scale system.

The results for the prototype are here reported: for figures 6.40 to 6.51, the same considerations that were made for the simulation of the CT3 scale system are valid. Of great interest is figure 6.52: it shows how C_\perp , normalized with the maximum force that the valve's actuator (full scale and scaled) can exert, evolves as the rocker rotates of $\tilde{\varphi}$. The simulation for the prototype is terminated at $r_{O'P,end} = -7$ mm instead of $r_{O'P,end} = -7.88$ mm, because results were showing spurious oscillations, likely due to the low order of the numerical method implemented. However, the trend indicates that $\frac{C_\perp}{F}$, of about 0.51 are to be expected for the scaled down model. C_\perp evolves in a very similar way to the full scale system, so this configuration is appropriate to verify the concept. In table 6.2 the parameters for the scaled prototype are reported .

Parameter	Value	Comment
r_{OL}	26.3 mm	Scaled from CT3 sized system.
r_{CL}	56.2 mm	Scaled from CT3 sized system.
$r_{OO'}$	26.3 mm	Scaled from CT3 sized system.
f	13.1 mm	Scaled from CT3 sized system.
f_r	13.1 mm	Scaled from CT3 sized system.
μ_{st}	0.12-0.28	See table 6.1.
μ_{din}	0.08-0.2	See table 6.1.
SF	1.5	Safety factor for masses, giving margin for additional parts currently unaccounted for (e.g. bearings, link in L).
I_{OL}	$6.49e-5 * SF$ kg m ²	Found after developing the geometry.
m_{act}	$0.27 * SF$ kg	Mass of the actuator, from [14].
m_p	$0.054 * SF$ kg	Mass of moving parts of the actuator, from [14].

Table 6.2: Table with parameters for the scaled prototype rocker.

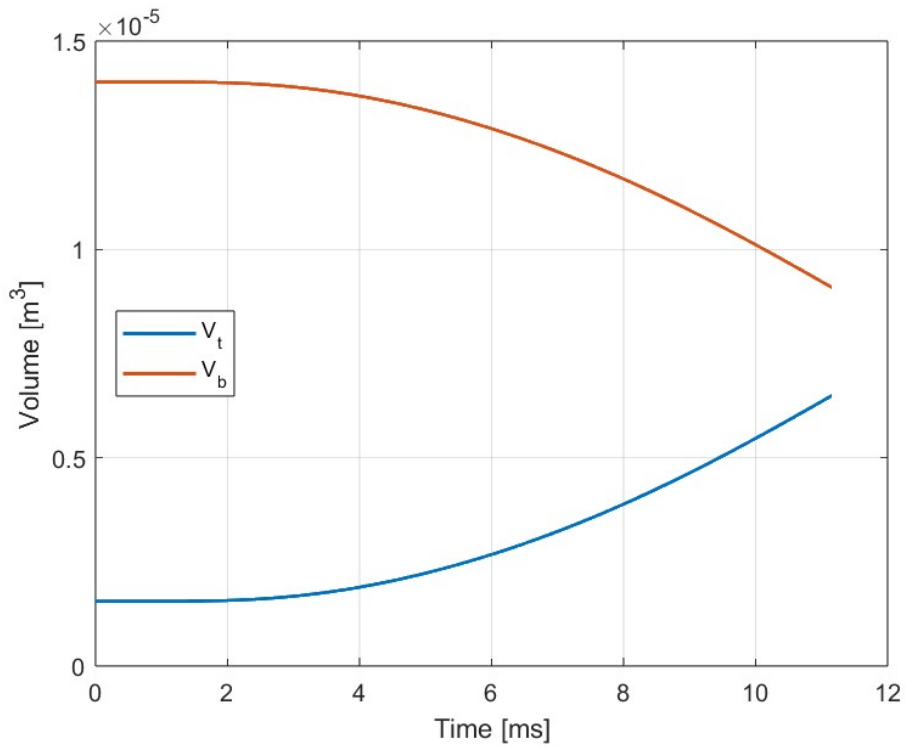


Figure 6.40: Actuator's chamber volumes in time.

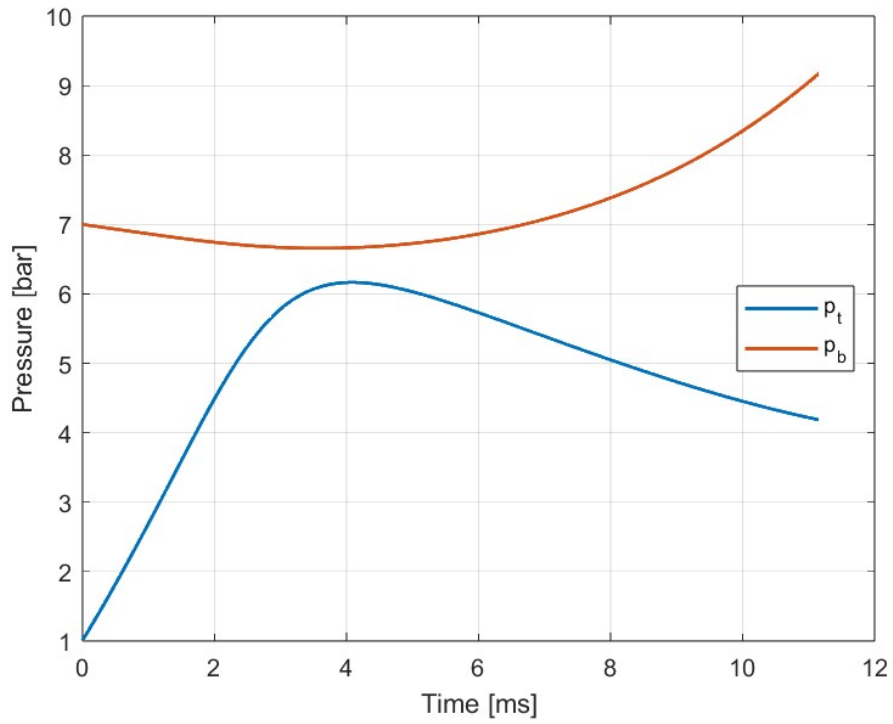


Figure 6.41: Actuator's chamber pressures in time.

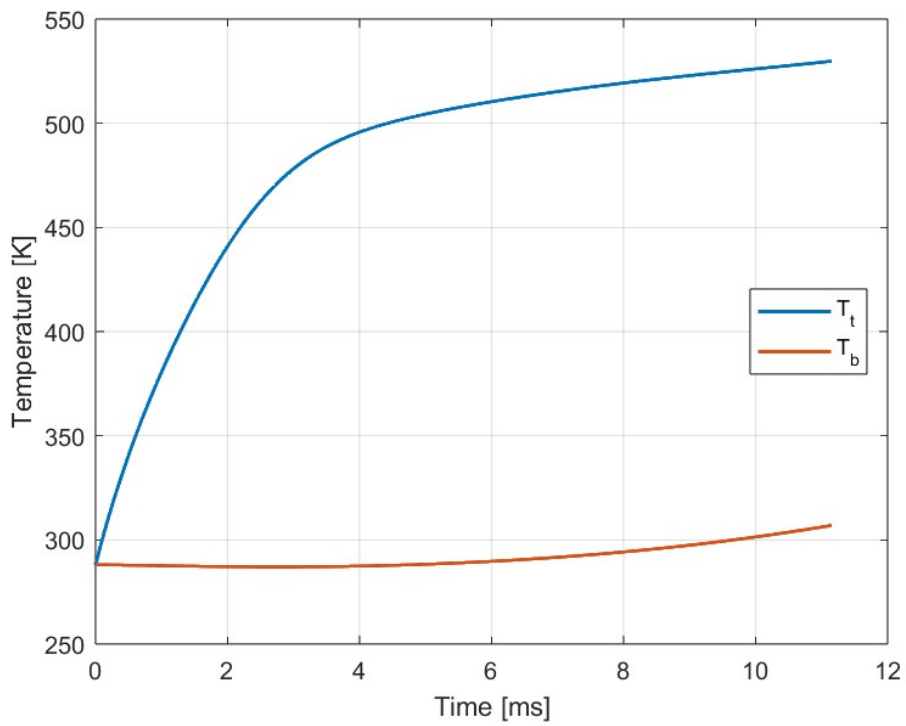


Figure 6.42: Actuator's chamber temperatures in time.

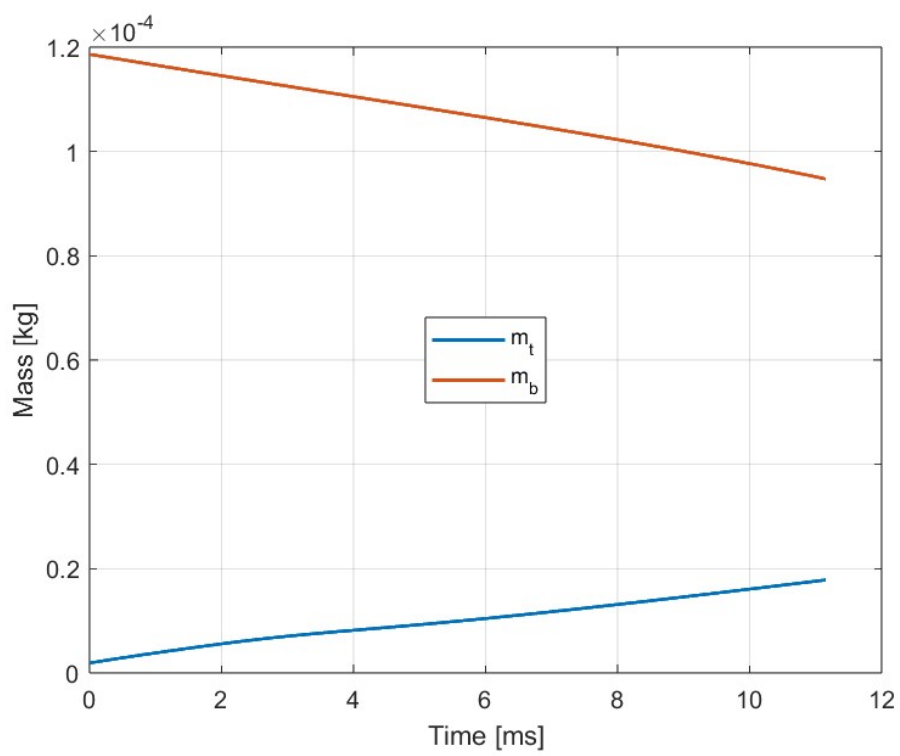


Figure 6.43: Mass of air in actuator's chambers.

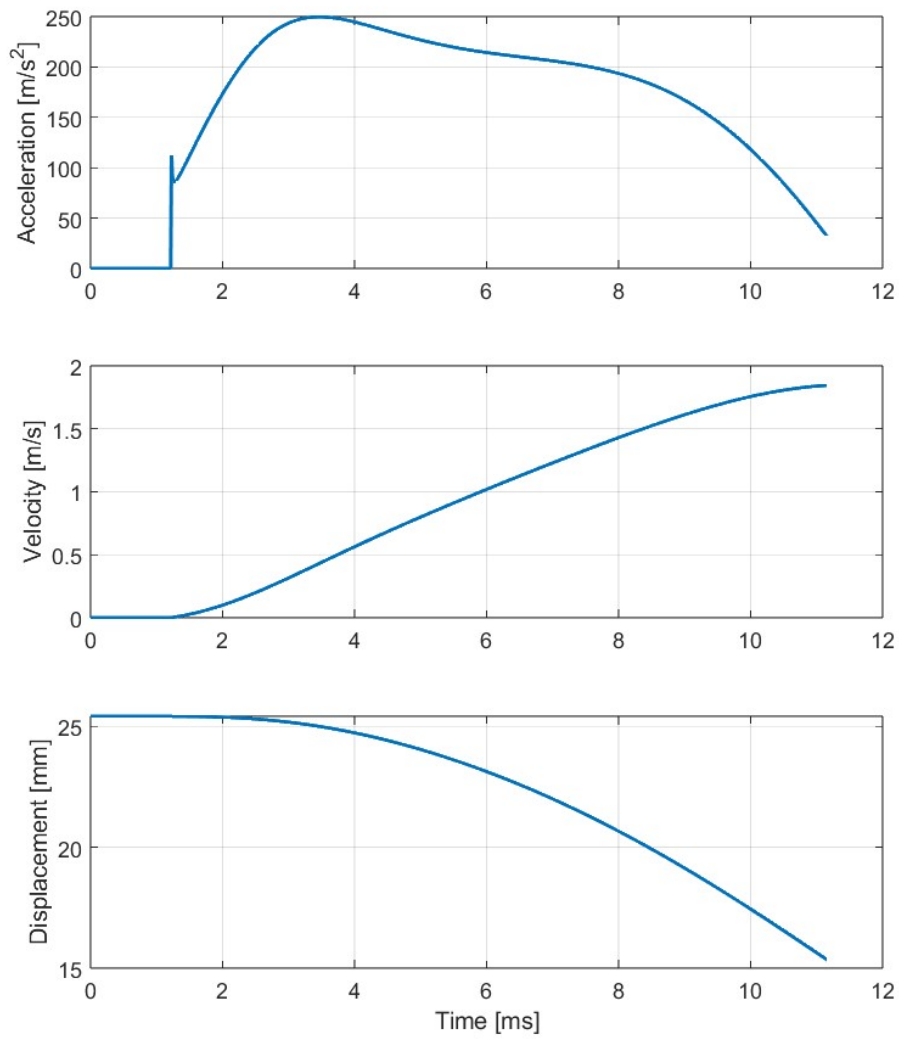


Figure 6.44: Acceleration, velocity and displacement of the rocker's actuator.

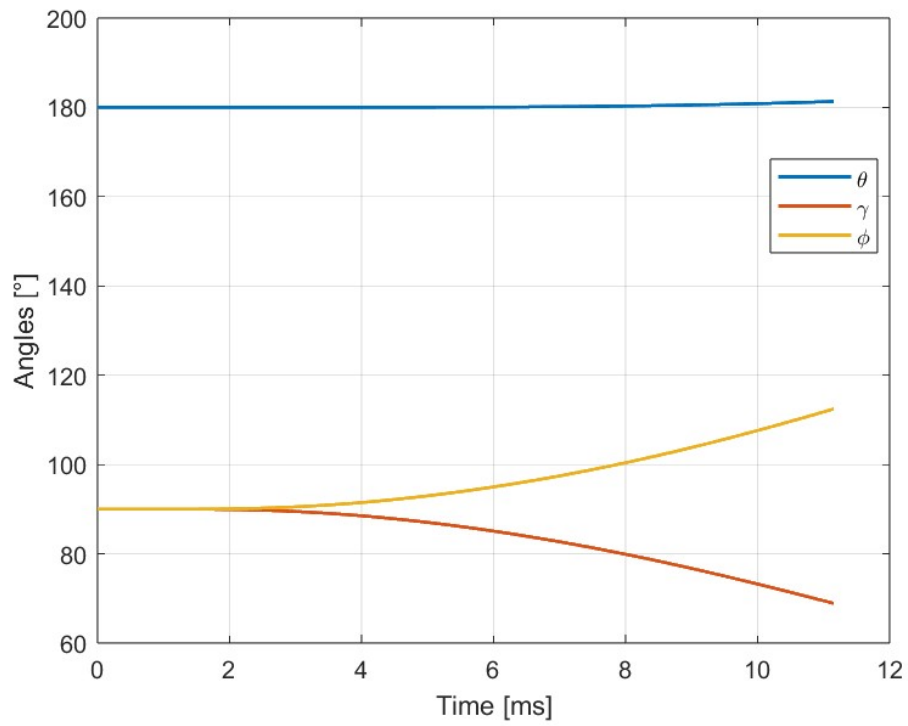


Figure 6.45: Angles' evolution in time.

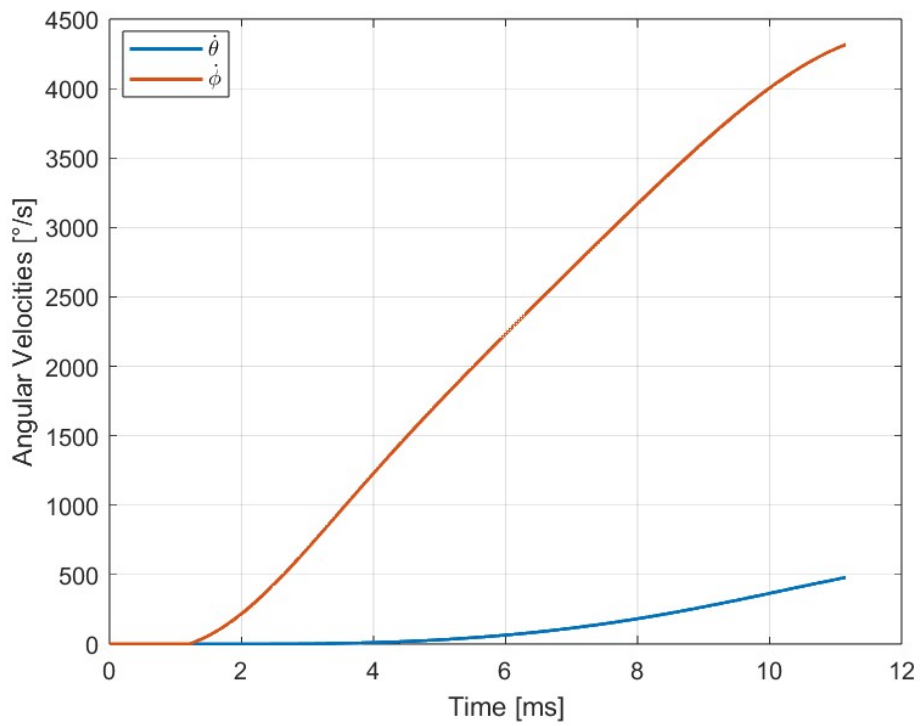


Figure 6.46: Angular velocities.

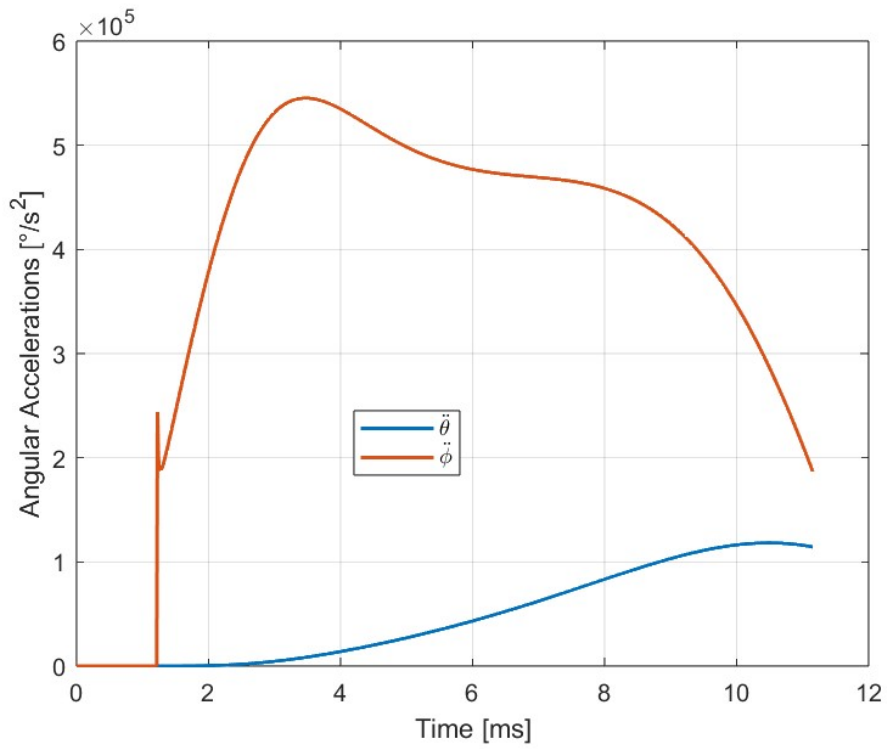


Figure 6.47: Angular accelerations.

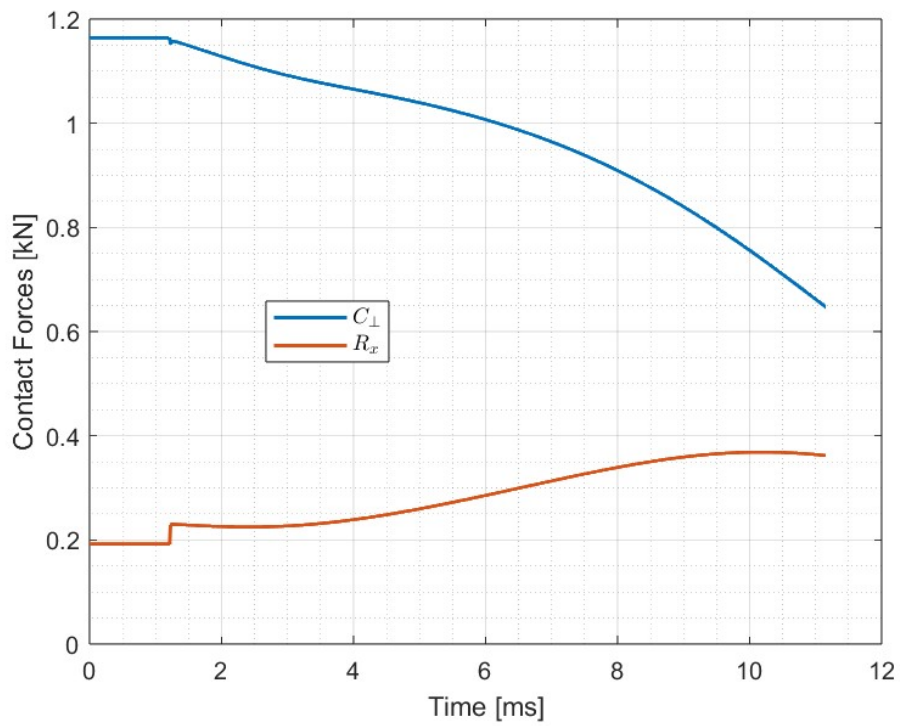


Figure 6.48: C_{\perp} and R_x .

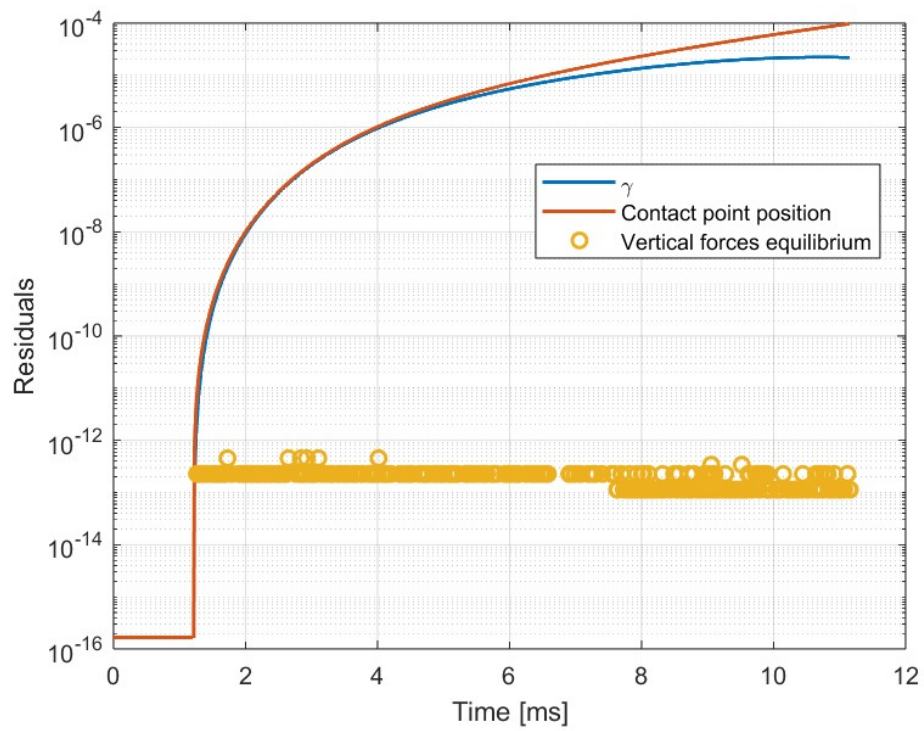


Figure 6.49: Residuals for γ , the position of P and for the vertical equilibrium of the valve's placeholder.

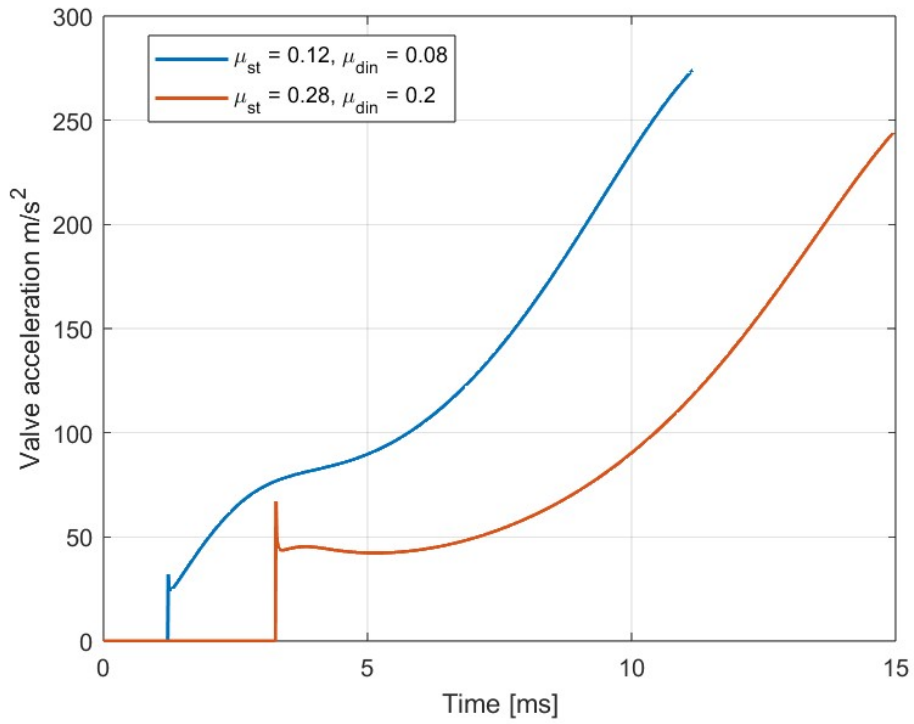


Figure 6.50: Valve acceleration.

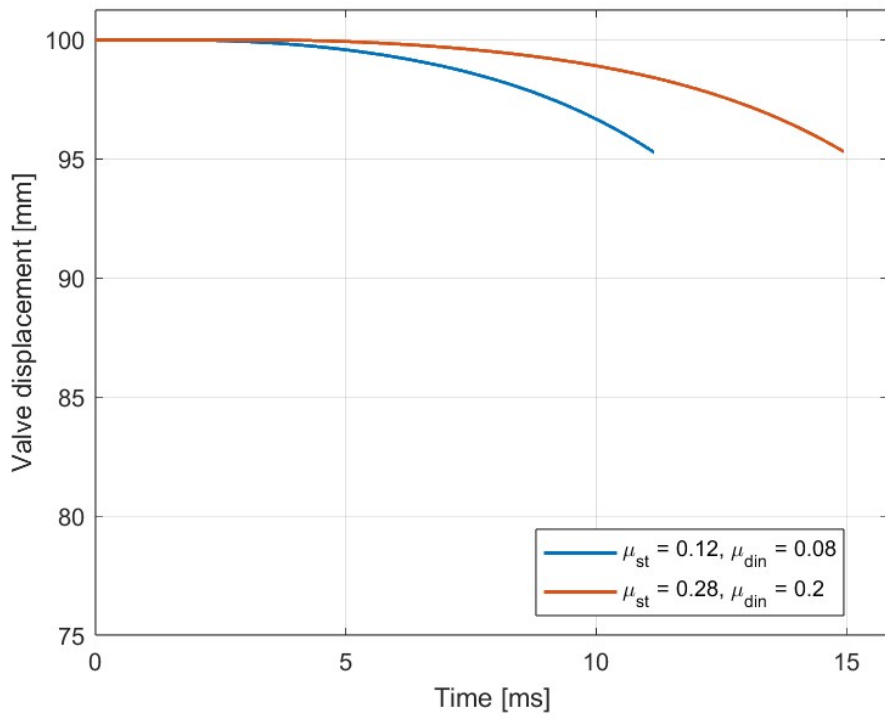


Figure 6.51: Valve displacement.

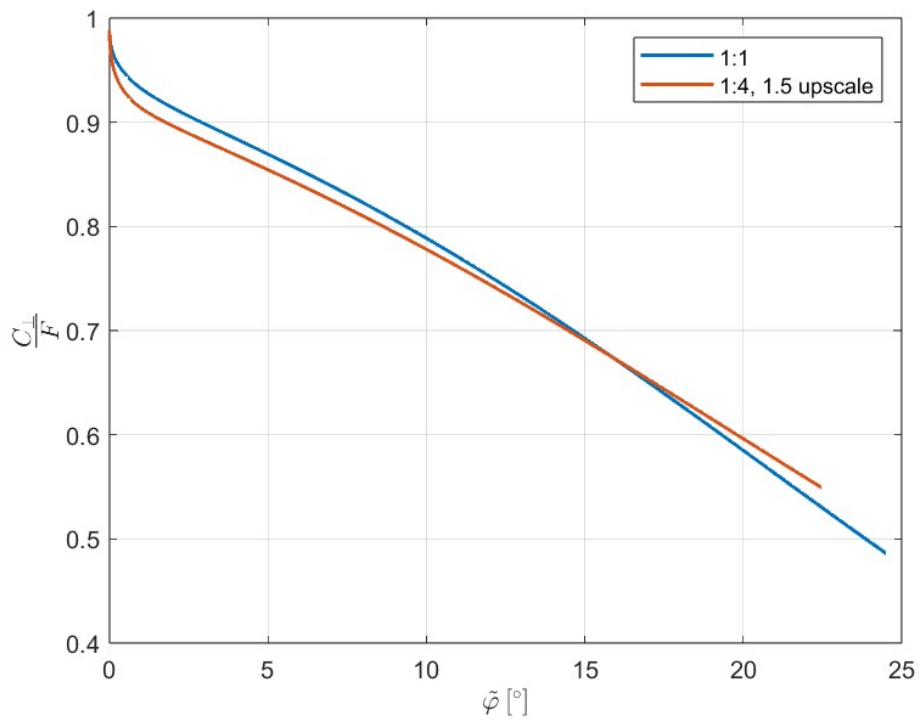


Figure 6.52: $\frac{C_{\perp}}{F}$ evolution as the rocker rotates by $\tilde{\varphi}$.

Chapter 7

Conclusions and future work

This work consisted in studying mechanical solutions for updating the release mechanism for the pneumatically actuated shutter valves of CT2 and CT3 wind tunnels. These solutions were envisioned to be powered by pneumatic actuators, for ease of access to pneumatic lines, costs, and the ability to fully automate them. Furthermore, safety can be enhanced and decoupled from the reliability of power systems and pneumatic lines, by accurately selecting the correct configuration of solenoid valves (normally closed and normally open), as well as equipping the system with safety features such as manual position locks for actuators or for the whole system.

Totally avoiding slip during opening phases was proven to not be a feasible possibility, because of the extremely high accelerations that this would require. A brake solution was also evaluated, but the results of the simulation showed a decrease in acceleration of the valve shortly after the start of the motion. Mitigating this with a steeper braking surface would mean significantly increasing the delay in the release, as the larger actuator required retains the same connecting port size. The rocker block is the solution that shows to be the most promising, in terms of compliance with the strict low delay requirements and trends of relevant quantities. The system also appears to promise high consistency, which can be further enhanced by enclosing the system, limiting exposure to contaminants that may alter friction coefficients. The geometry of the slipping surface can be further optimized by shortening the flat surface section of the rocker and designing the subsequent curved section with segments of progressively decreasing radii. As explained previously, this will shorten the required rocker rotation to clear the rod end, thus shortening the acceleration, velocity and travel of the rocker's actuator. This will in turn reduce the force opposing the rocker's rotation and the contact force between the rocker and the rod end, ultimately resulting in higher valve acceleration. The effect of altering the initial

position of the contact point should also be investigated: with respect to figure 6.20, moving P to the right of O reduces the leverage of C_{\perp} , which can result either in a smaller actuator to keep the system locked or in increased slope of the flat surface α .

An explicit method was used to evaluate the performance of the system. While this choice allowed easy implementation and integration between the pneumatic model and the kinematics and dynamics equations to resolve the motion of the systems, its low accuracy affected the quality of results for the scaled down prototype of the rocker block. For further development and full simulations of the unlocking motion, it would be ideal to develop the mathematical model in higher precision methods. The mathematical model for determining valve acceleration and tracking of the contact point past the flat surface of the rocker should also be developed and implemented to evaluate the performance of the full release motion.

Throughout the analysis of these solutions, it has been assumed that the solenoid valves controlling airflow to the actuator's chambers are acting instantaneously. In reality, these valves are very fast, but not as much as it would take for this hypothesis to be true in the time scale of interest for this project. [13] lists many 1/2 in solenoid valves that may be of interest for this application to have response times lower than 30 ms. Choosing one that is fed by DC current could improve the consistency of the response time of the valve, as this is affected by the phase angle of the power supply at the moment when a change in position is triggered. This can help in calibrating a logic controller that can trigger the change in position for the valve controlling the rocker's actuator at pressure levels in the compression tube lower than the desired value for the test. This anticipated opening signal is given so to account for delays in the locking mechanism, and exploits the near linear growth of pressure in the compression tube to achieve accurate conditions in the tests.

Other next steps for the project revolve around a detailed design of the test rig for the prototype, and developing an experimental campaign aimed at evaluating the performance of the system and retrieving data to validate the simulations.

Bibliography

- [1] V Andreoli, G Paniagua, and S Lavagnoli. “HIGH-FIDELITY MODEL OF A TRANSIENT TURBINE FACILITY FOR OFF-DESIGN AEROTHERMAL TESTING”. en. In: ().
- [2] *The von Karman Institute for Fluid Dynamics*. URL: <https://www.vki.ac.be/>.
- [3] VKI. *Technical drawings for CT3 facility*.
- [4] C. H. Sieverding and T. Arts. *The VKI Compression Tube Annular Cascade Facility CT3*.
- [5] S. Janardhanraj, S.K. Karthick, and A. Farooq. “A review of diaphragmless shock tubes for interdisciplinary applications”. en. In: *Progress in Energy and Combustion Science* 93 (Nov. 2022). Publisher: Elsevier BV, p. 101042. ISSN: 0360-1285. DOI: [10.1016/j.pecs.2022.101042](https://doi.org/10.1016/j.pecs.2022.101042). URL: <https://linkinghub.elsevier.com/retrieve/pii/S0360128522000491>.
- [6] T. V. Jones, P. Street, and M. Westby. “Recent Enhancement to the DRA Shock Tunnel”. In: *The European Forum on Wind Tunnels*. 14–17 September 1992. Southampton, 1992.
- [7] Alan H Epstein and Gerald R Guenette. “THE DESIGN OF THE MIT BLOW-DOWN TURBINE FACILITY”. en. In: ().
- [8] T. Abe et al. “Rupture-disk-less shock-tube with compression tube driven by free piston”. In: *Shock Waves* 7.4 (Aug. 1997), pp. 205–209. ISSN: 0938-1287, 1432-2153. DOI: [10.1007/s001930050076](https://doi.org/10.1007/s001930050076). URL: <http://link.springer.com/10.1007/s001930050076>.
- [9] Matthew McGilvray et al. “The Oxford High Density Tunnel”. en. In: *20th AIAA International Space Planes and Hypersonic Systems and Technologies Conference*. Glasgow, Scotland: American Institute of Aeronautics and Astronautics, 2015. ISBN: 978-1-62410-320-9. DOI: [10.2514/6.2015-3548](https://doi.org/10.2514/6.2015-3548). URL: <http://arc.aiaa.org/doi/10.2514/6.2015-3548>.

-
- [10] G. Paniagua et al. “Design of the Purdue Experimental Turbine Aerothermal Laboratory for Optical and Surface Aerothermal Measurements”. en. In: *Journal of Engineering for Gas Turbines and Power* 141.1 (Jan. 2019), p. 012601. ISSN: 0742-4795, 1528-8919. DOI: [10.1115/1.4040683](https://doi.org/10.1115/1.4040683).
- [11] Kinetrol. *Home - Kinetrol*. July 2024. URL: <https://www.kinetrol.com/>.
- [12] Edmond Richer and Yildirim Hurmuzlu. “A High Performance Pneumatic Force Actuator System: Part I—Nonlinear Mathematical Model”. en. In: *Journal of Dynamic Systems, Measurement, and Control* 122.3 (Sept. 2000), pp. 416–425. ISSN: 0022-0434, 1528-9028. DOI: [10.1115/1.1286336](https://doi.org/10.1115/1.1286336). URL: <https://asmedigitalcollection.asme.org/dynamicsystems/article/122/3/416/464478/A-High-Performance-Pneumatic-Force-Actuator-System> (visited on 11/20/2024).
- [13] Tameson.com. *Tameson - We simplify industrial supply | Tameson.com*. URL: <https://tameson.com/>.
- [14] Festo. *Pneumatic electric automation technology | Festo USA*. URL: <https://www.festo.com/>.
- [15] Richard T. Barrett. *Fastener Design Manual*. NASA Reference Publication (RP) NASA-RP-1228. Cleveland, OH, United States: NASA Lewis Research Center, 1990. URL: <https://ntrs.nasa.gov/citations/19900009424>.
- [16] Roland Rennert, Eckehard Kullig, and Michael Vormwald, eds. *Analytical strength assessment of components Made of Steel, Cast Iron and Aluminium Materials in Mechanical Engineering: FKM Guideline*. eng. 6th revised Edition, 2012. 2013. ISBN: 978-3-8163-0649-8.
- [17] *SKF*. URL: <https://www.skf.com/>.
- [18] NATO, ed. *High temperature problems in gas turbine engines: Papers*. eng. AGARD Conference Proceedings 229. Neuilly-sur-Seine: AGARD, 1978. ISBN: 978-92-835-0209-8.
- [19] G. Paniagua, C. H. Sieverding, and T. Arts. “Review of the von Karman Institute Compression Tube Facility for Turbine Research”. en. In: *Volume 3C: Heat Transfer*. San Antonio, Texas, USA: American Society of Mechanical Engineers, June 2013, V03CT14A031. ISBN: 978-0-7918-5516-4. DOI: [10.1115/GT2013-95984](https://doi.org/10.1115/GT2013-95984). URL: <https://asmedigitalcollection.asme.org/GT/proceedings/GT2013/55164/San%20Antonio,%20Texas,%20USA/249538>.

- [20] Janardhanraj Subburaj, Touqeer Anwar Kashif, and Aamir Farooq. “Methane and n-hexane ignition in a newly developed diaphragmless shock tube”. en. In: *Combustion and Flame* 253 (July 2023). Publisher: Elsevier BV, p. 112818. ISSN: 0010-2180. DOI: [10.1016/j.combustflame.2023.112818](https://doi.org/10.1016/j.combustflame.2023.112818). URL: <https://linkinghub.elsevier.com/retrieve/pii/S0010218023001992>.
- [21] T. Wolf, M. Estorf, and R. Radespiel. “Investigation of the starting process in a Ludwig tube”. en. In: *Theoretical and Computational Fluid Dynamics* 21.2 (Mar. 2007), pp. 81–98. ISSN: 0935-4964, 1432-2250. DOI: [10.1007/s00162-006-0040-z](https://doi.org/10.1007/s00162-006-0040-z). URL: <http://link.springer.com/10.1007/s00162-006-0040-z>.
- [22] M. Estorf, T. Wolf, and R. Radespiel. “Experimental and Numerical Investigations on the Operation of the Hypersonic Ludwig Tube Braunschweig”. In: 563 (Feb. 2005). Conference Name: Fifth European Symposium on Aerothermodynamics for Space Vehicles ADS Bibcode: 2005ESASP.563..579E, p. 579. URL: <https://ui.adsabs.harvard.edu/abs/2005ESASP.563..579E>.
- [23] Nicholas R. Atkins, Robert J. Miller, and Roger W. Ainsworth. “The Development of Aerodynamic Performance Measurements in a Transient Test Facility”. en. In: *Volume 5: Turbo Expo 2004, Parts A and B*. Vienna, Austria: ASMEDC, Jan. 2004, pp. 1325–1338. ISBN: 978-0-7918-4170-9. DOI: [10.1115/GT2004-53813](https://doi.org/10.1115/GT2004-53813). URL: <https://asmedigitalcollection.asme.org/GT/proceedings/GT2004/41707/1325/307207>.
- [24] Dong Chen and Guofeng Zou. “Research on Contact Pressure Distribution of Pad”. en. In: *MATEC Web of Conferences* 198 (2018). Ed. by Huafeng Ding and Hongliang Yuan, p. 01002. ISSN: 2261-236X. DOI: [10.1051/mateconf/201819801002](https://doi.org/10.1051/mateconf/201819801002). URL: <https://www.matec-conferences.org/10.1051/mateconf/201819801002> (visited on 03/25/2025).

Torino, 19 Marzo 2025